Improved Modelling of Offshore Wind Generation Using Machine Learning

On a Reliable Supply of Electricity in Future Power Systems

by

Thuy-hai Nguyen

A thesis presented for the degree of
Philosophiae Doctor in Engineering Sciences & Technology

pursued in the Electrical Power Engineering Unit of the
University of Mons

Members of the Jury

Prof. Laurent Bricteux, University of Mons	Chairman
Prof. Philippe Chatelain, University of Louvain	
Prof. Paul Cuffe, University College Dublin	
Dr Jean-François Toubeau, University of Mons	
Prof. Lieven Vandevelde, Ghent University	
Prof. Jacques Lobry, University of Mons	Secretary
Prof. François Vallée, University of Mons	Supervisor
Prof. Emmanuel De Jaeger, University of Louvain	Co-supervisor

4 February 2025

Sustainability in all things should be our species' philosophy

---

Sir David Attenborough
(British biologist, natural historian, and writer, 1926 -)

We are persuaded to spend money we don't have,
on things we don't need,
to make impressions that won't last,
on people we don't care about

From "An Economic Reality Check"
Tim Jackson
(British ecological economist, 1957 -)

Acknowledgements

A l'origine, faire une thèse n'était pas dans mes plans d'avenir. A la fin de mes études, tout ce à quoi j'aspirais était de travailler dans l'aéronautique et de concevoir des avions. J'avais même déménagé à Toulouse, siège du plus grand constructeur mondial d'avions, et obtenu un stage de fin d'études chez Airbus. Cependant, je n'avais pas anticipé la pandémie mondiale qui a cloué tous les avions au tarmac, fracassant l'industrie aéronautique et mes aspirations professionnelles par la même occasion. Ce que je n'avais pas anticipé non plus, c'est un email d'un ancien professeur, dans un timing parfait, qui me proposait de venir faire une thèse dans le service de génie électrique et sur un thème, selon ses propres termes, "plus ou moins en relation avec l'aéronautique". Il s'avère que le sujet portait plutôt sur l'éolien offshore et son impact sur la sécurité d'approvisionnement électrique. Après une brève discussion plutôt convaincante avec ce professeur (sans suspense, il s'agissait de François Vallée), je décide d'accepter la proposition et de revenir en Belgique faire une thèse. Une décision que je ne regrette absolument pas et qui m'a emmenée dans cette aventure incroyable qu'est une thèse de doctorat.

Je ne pourrai pas débuter mes remerciements sans citer mes promoteurs François Vallée et Emmanuel De Jaeger, sans qui cette thèse n'aurait pas été possible. Merci Emmanuel pour tes conseils bienveillants et pour ton accueil chaleureux lors de mon séjour à l'UCLouvain. François, merci énormément pour ta bonne humeur et ton enthousiasme contagieux, tes discours motivationnels, tes conseils précieux et la confiance que tu m'as accordée durant toute la durée de mon doctorat. Quel défi d'effectuer une thèse dont le sujet est la continuité de celle de son promoteur, mais tu m'as guidée avec patience et tu m'as transmis ta passion pour l'adéquation des systèmes électriques.

Je dois également remercier de tout cœur le Dr Jean-François Toubeau, qui m'a tellement apporté durant ce doctorat, d'un point de vue scientifique mais aussi humain. Ta rigueur scientifique et ta recherche de l'excellence m'ont poussée à me dépasser et à me plonger avec ferveur dans ma thèse. En

outre, nos discussions passionnantes sur la transition écologique et l'économie m'ont réellement inspirée et ont profondément changé ma façon d'aborder ma recherche.

Je remercie également les membres de mon jury de thèse pour leur retour scientifique hautement qualitatif, leurs questions judicieuses qui m'ont permis de prendre du recul sur mon travail, et leur bienveillance.

Je suis heureuse d'avoir pu effectuer ma thèse dans le cadre du projet PhairywinD, financé par le Fonds de Transition Energétique organisé par le SPF Economie. En effet, j'ai pu contribuer à un projet de recherche important pour le futur énergétique de la Belgique. Je remercie tous mes collègues PhairywinDers et en particulier Marijke, pour avoir créé une véritable communauté, pour l'organisation d'évènements fantastiques et pour son soutien continu.

Durant ma thèse, j'ai eu la chance d'effectuer un séjour scientifique de recherche de 2 mois et demi à la DTU, une excellente université au Danemark. Au sein de la division "Systems Engineering and Optimization", j'ai pu côtoyer des chercheurs de tous les horizons et passionnés par l'énergie éolienne: ils m'ont inspiré tant d'un point de vue personnel que scientifique. Je tiens à remercier particulièrement le Dr Pierre-Elouan Réthoré pour m'avoir chaleureusement accueillie au sein de son équipe ainsi que pour ses précieux conseils et son accompagnement, et le Dr Julian Quick pour son aide inestimable et son enthousiasme pour le travail sur lequel nous avons étroitement collaboré.

Un bon environnement de travail est pour moi une condition indispensable pour la réussite et le bon déroulement d'une thèse. Pour ma part, j'ai eu la chance d'évoluer au sein d'un service incroyable, le GELE, et je remercie tous les collègues que j'ai pu côtoyer durant mes 4 années de thèse pour leurs conseils, leur soutien et leur bienveillance. Aux bébés du GELE: Apolline, Arnaud, Aurélia, Chloé, Clélia, Julien, Louise, Martin, merci pour les parties de ping-pong intenses, les pauses thé, et les moments de partage et de rire. J'ai une pensée toute particulière pour mes collègues de bureau: Aurélia, mon binôme adequacy qui m'a appris à prendre certains choses de la vie avec nonchalance, Clélia, mon binôme bavardage et ma référence non officielle de Machine Learning, et Julien, toujours curieux d'en savoir plus sur ma recherche et constamment prompt à m'aider à trouver des solutions à mes problèmes.

J'ai également eu la chance d'être entourée d'amis fantastiques qui m'ont soutenue et se sont intéressés à ma recherche avec curiosité. Merci à mes amis d'enfance Paul et Isaline, pour avoir supporté mes soliloques interminables sur la transition énergétique, mais surtout pour votre bonne humeur constante, votre écoute et votre amitié indéfectible. Merci également à Eloïse pour m'avoir

maintenue dans une forme physique décente durant ces quatre dernières années et pour m'avoir permis de me vider l'esprit lors de nos parties de squash effrénées.

Enfin, je termine ces remerciements en rendant hommage à ma famille. Je remercie ma sœur, Dr Céleste, qui m'a ouvert la voie du doctorat et qui par ses conseils m'a permis d'éviter de nombreux écueils sur le chemin de la thèse. En outre, une des mes plus grandes fiertés est de dorénavant t'entendre t'extasier à chaque fois que tu aperçois une éolienne. Et enfin, un énorme merci à mes parents pour leur soutien inconditionnel, que ce soit pour cette thèse mais aussi tout au long du parcours qui y a mené. Merci à ma maman d'être toujours à l'écoute quand je traverse des mauvaises passes, mais également de me botter les fesses quand je me morfonds inutilement, de m'aider à prendre les décisions importantes dans ma vie, et de me pousser à toujours donner le meilleur de moi-même tout en faisant des choses qui me plaisent. Merci à mon papa pour les discussions sur la politique et l'économie qui me permettent de situer ma recherche sur les É-O-liennes dans un contexte plus global, de m'avoir gentiment convoyée au labo malgré mes horaires bizarres, et pour éveillé mon esprit d'ingénieur.

MERCI à tous.

Summary

Energy is the bedrock of modern economies and societies, yet its production and consumption are also responsible for 75% of greenhouse gas emissions, making it the primary driver of climate change. But global warming is not the only negative impact that human activity has on our planet. The energy transition must aim not only at counteracting climate change, but also at returning us below the 9 planetary boundaries that describe limits beyond which the environment may not be able to self-regulate anymore. Equally important is that the energy transition must be fair, allowing everyone to thrive in an environment respectful of the Earth. In other words, we need to find the safe space between the 9 planetary boundaries and a social foundation of well-being that no one should fall below. Encompassed within the basics needs of life is notably *access to energy*.

Renewable energy sources are expected to play a significant role in the energy transition, because of their low emissions of greenhouse gases over their lifetime. However, they affect other planetary boundaries as they require a lot of raw materials and a considerable surface area, potentially jeopardizing biodiversity and impacting land use. Therefore, the operation of those energy sources must be optimized to produce electricity in the most efficient way and avoid spillage of electricity. Moreover, renewable energy sources are inherently intermittent, fluctuating, and highly unpredictable, thus posing many challenges to ensure a reliably supply of electricity. A detailed planning and usage throughout the year will be necessary to guarantee access to electricity for everyone, at all times, and at an affordable price.

This thesis does not have the ambition to tackle all the challenges of the energy transition, but aims at discussing the impact of the massive installation of renewable energy sources, targeting one type in particular: *offshore wind energy*. This work is focused on developing enhanced models of offshore wind generation, with the purpose of improving the integration of future offshore wind farms in power systems by assessing their impact on the reliability of supply

and their ability to provide balancing services. Machine Learning techniques are leveraged to build a fast, accurate and topology-aware surrogate for offshore wind farms, able to capture complex aerodynamic phenomena and to generalize to any layout configuration while keeping a reasonable computation time. This model is then directly integrated within adequacy studies aimed at evaluating the reliability of electricity supply in future power systems with a high share of offshore wind generation. It allows to assess the impact of an improved modelling of offshore wind power on reliability indices. The generalization capabilities enable the consideration of the uncertainty related to the topology of future wind farms, as their layout (turbine position, power density, turbine technology) is still unknown. Thanks to the topology-aware abilities of the wind farm surrogate, the same model can be used to consider many possible farm configurations without hindering the tractability of the computation process. Outcomes show that disregarding power losses due to aerodynamic phenomena arising in offshore wind farms leads to an underestimation of reliability indices, thereby concealing adequacy issues and preventing the right investments to ensure a sufficient reliability of the system. Finally, we focused on the foreseen participation of offshore wind farms to reserve markets, aimed at restoring balance within the system in case of sudden perturbations. We explored how the layout of future wind farms can be optimized to account for their participation to ancillary frequency services. The developed surrogate is especially appropriate for a wind farm layout optimization problem, where a different layout is seen at each iteration, justifying the need for a topology-aware model, applicable to any wind farm configuration.

Contents

Acronyms

AD	Actuator Disk
AEP	Annual Energy Production
aFRR	Automatic Frequency Restoration Reserve
ARMA	Auto-Regressive Moving Average
BSP	Balancing Service Provider
CFD	Computational Fluid Dynamics
DA	Day-Ahead
DAEM	Day-Ahead Energy Market
DNS	Direct Numerical Simulation
GBRT	Gradient Boosting Regression Tree
JERM	Joint day-ahead Energy and Reserve Market
LCOE	Levelized Cost of Energy
LES	Large Eddy Simulations
LOE	Loss Of Energy
LOEE	Loss Of Energy Expectation
LOL	Loss Of Load
LOLE	Loss Of Load Expectation
MAE	Mean Absolute Error
ML	Machine Learning
MLP	Multi-layer Perceptron
MPPT	Maximum Power Point Tracking
NN	Neural Network

O&M	Operation and Maintenance
RANS	Reynolds-Averaged Navier Stokes
ReLU	Rectified Linear Unit
RMSE	Root Mean Squared Error
SCADA	Supervisory Control And Data Acquisition
SGD	Stochastic Gradient Descent
TSO	Transport System Operator
VARMA	Vector Auto-Regressive Moving Average
VRES	Variable Renewable Energy Sources
WFLO	Wind Farm Layout Optimization

CHAPTER 1.

Introduction

How to ensure a fair energy transition for all ? How to guarantee an energy transition that respects our life-giving planet in every aspect ? What is the role of renewable energy sources ? Are they the easy solution for this problem ? These complex questions are at the heart of today's challenges regarding the energy transition. They cannot be all and fully answered in one single work, but they will be the guiding thread for the remaining of this thesis.

The first chapter provides a brief introduction to current challenges regarding energy, which allows setting the context for the objectives and contributions of the proposed research work. In particular, section 1.1 discusses the impact of human activities related to energy on the Earth system, the complexity of making an energy transition fair for all, and the role of offshore wind energy. Then, section 1.2 explores the motivations, research questions and scope of the proposed research work. Thereafter, section 1.3 presents the corresponding research objectives and scientific contributions. Finally, section 1.4 provides an outline of the remainder of this dissertation.

1.1. Context

Climate change caused by human activities is a fact. There is now a consensus in the scientific community that our fast-paced use of fossil fuels, our never ending exploitation of raw materials, our unreasonable land use, and our careless greenhouse gases emissions have put a severe strain on Earth's climate system. There is no need for an umpteenth introduction on global warming. A few key figures can sum up current issues: according to the last IPCC (Intergovernmental Panel on Climate Change) report [1], the increase of global surface temperature has now reached 1.1°C above levels in 1850–1900, atmospheric CO_2 concentrations are higher than at any time in at least 2 million years, the

global mean sea level has increased by 0.20 m since 1901, and approximately 3.6 billion people live in contexts that are highly vulnerable to climate change (heatwaves, heavy precipitation, droughts, tropical cyclones, ...).

However, global warming is not the only negative consequence of human activities. Environmental scientists have identified 9 planetary boundaries that describe limits to the impacts of human activities on the Earth system [2]. Beyond these limits, the environment may not be able to self-regulate anymore, which means that the Earth system would leave the period of stability of the Holocene, in which human society developed. Every boundary is characterized by one or several control variables and the corresponding limit values:

1. Climate change: atmospheric CO_2 concentration
2. Biodiversity loss: rate of species extinction
3. Biogeochemical composition: levels of phosphate and nitrogen, applied to land as fertilizers
4. Ocean acidification: global mean saturation state of calcium carbonate in surface seawater
5. Land use: part of forests remaining intact
6. Freshwater change: human induced disturbance of green water (available to plants) and blue water (rivers, lakes, groundwater, glaciers, polar ice)
7. Ozone layer depletion: stratospheric ozone concentration
8. Atmospheric aerosols: interhemispheric difference in aerosol optical depth
9. Novel entities: percentage of synthetic chemicals released to the environment without adequate safety testing

As it can be seen on Fig. 1.1, 6 out of 9 boundaries have already been crossed as of 2023, with only ocean acidification, atmospheric aerosol loading and stratospheric ozone depletion remaining in the safe operating space. It is well past-time for an ecological transition to reduce pressure on the planet and safeguard the stability of our home. Otherwise, damage will be irreversible and we will put in jeopardy the living conditions in which humanity has thrived for thousands of years. A technological solution backed up by many scientists is a massive development of renewable energy [3].

Variable Renewable Energy Sources (VRES) such as onshore and offshore wind turbines, and photovoltaic panels, have emerged as an important building block for the energy transition. They do not emit greenhouse gases during

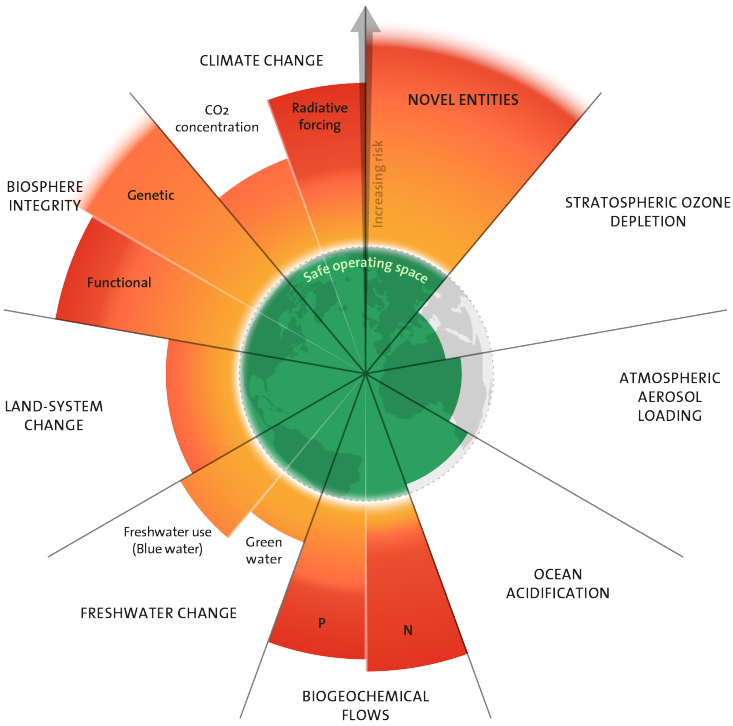

Figure 1.1.: Planetary boundaries in 2023 [2].

the production of electricity, they diversify energy supply and they reduce dependence on imported fuels. However, although VRES seem to enable us to counteract climate change and reach carbon neutrality, they might impede on other planetary boundaries. Indeed, solar panels require a large amount of silicon, while building a wind turbine relies upon a lot of raw materials: copper for wiring and electricity generators, rare earths for synchronous machines, steel for the tower and hub, carbon fibres for the blades, and concrete for the turbine foundations. Mining and exploiting all those resources has a significant negative impact on land use and biodiversity. Moreover, because of their lower capacity factors, VRES involve using a lot of surface area, which might lead to deforestation and modifications of land use. Therefore, the decision to build wind turbines and solar panels should be taken carefully, as to avoid installing more VRES than necessary. Moreover, the operation of those energy sources must be optimized to produce electricity in the most efficient way and avoid spillage of electricity.

Coming back to the planetary boundaries, the overshoot of 6 of them already has drastic consequences on human well-being. The increase of weather and

climate extreme events have exposed millions of people to acute food insecurity and reduced access to water. Roughly half of the world's population currently experience severe water scarcity for at least part of the year [4]. Human mortality from floods, droughts and storms has severely escalated in highly vulnerable regions [5]. In some oceanic regions, ocean warming and acidification have been detrimental to food production from fisheries and shellfish aquaculture [6]. Occurrences of climate-related food-borne and water-borne diseases are exacerbated [7]. Mental health challenges arise because of trauma from extreme events, and loss of livelihoods and culture [8]. Individual livelihoods have been impacted through, e.g., destruction of homes and infrastructure, loss of property and income, health deterioration, and food insecurity, all of which having negative effects on gender and social equity.

Therefore, we should ensure an ecological transition that aims not only at decreasing pressure on Earth's resources but also at making sure that humanity can thrive in that environment. And that is the essence of the Doughnut, a concept introduced by the English economist Kate Raworth in 2017: a social foundation of well-being that no one should fall below, and an ecological ceiling of planetary pressure that we should not go beyond. Between the two lies a safe and just space for all [9], the sweet spot to target, as depicted in Fig. 1.2. The ecological ceiling consists in the 9 planetary boundaries cited above, while the social foundation encompass the 12 basic needs of life: sufficient food and cooking facilities, clean water and decent sanitation, access to education and healthcare, a minimum income and decent work, peace and justice, political voice, social equity, gender equality, decent housing, access to networks of information and social support, and finally, *access to energy*.

The energy transition, besides striving to counteract climate change without crossing other planetary boundaries, must not jeopardize the access of energy for all. VRES are inherently intermittent, fluctuating, and highly unpredictable and a massive installation of those energy sources in modern power systems results in many challenges to ensure a reliably supply of electricity. For example, a *dunkelflaute* is an extended period of time with minimal or no wind nor sun, usually occurring during winter [11], as depicted in Fig. 1.3. Highly-renewable electricity systems will thus require a detailed planning and usage throughout the year to guarantee electricity supply even in those conditions. Moreover, because many parts of the Doughnut are interconnected, hindering access to energy adversely impacts other social needs. Indeed, hospitals, schools, and essential governmental institutions must be provided with sufficient energy to guarantee the quality of healthcare, education and social stability. Furthermore, scarcity often yields inequality [12], as it was demonstrated during the 2022 energy crisis, where electricity prices reached values so high that they became

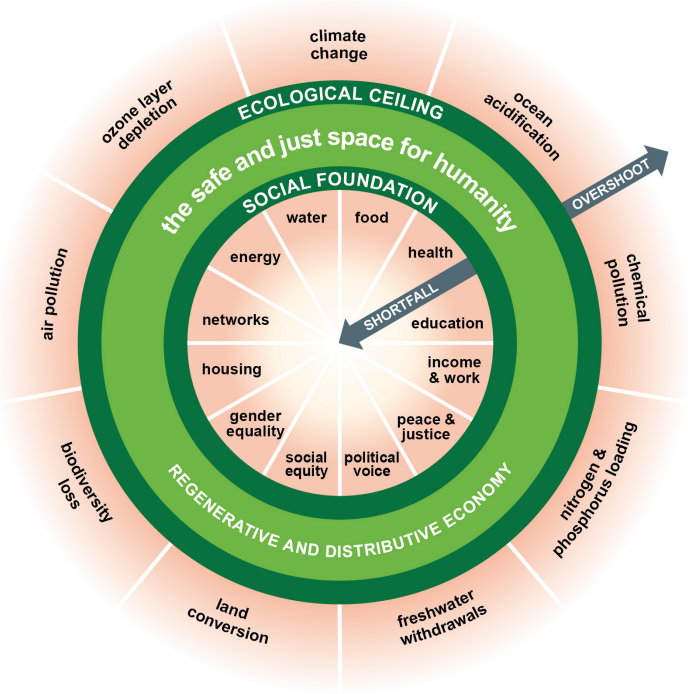

Figure 1.2.: The Doughnut: a depiction of the safe space between planetary boundaries and human well-being [9].

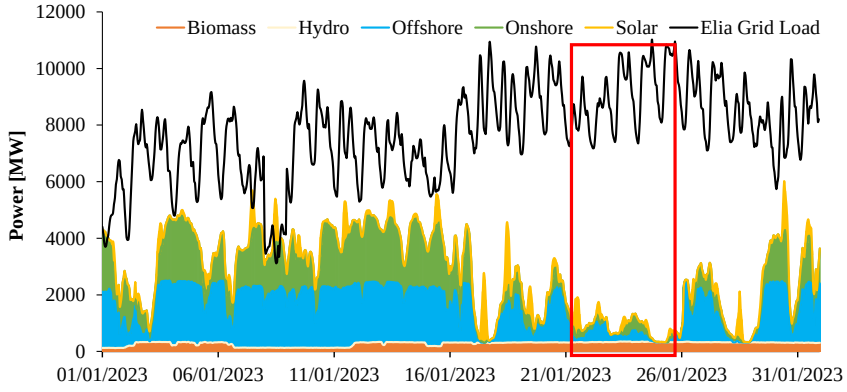

Figure 1.3.: Dunkelflaute event in Belgium during January 2023 (data from [10]).

unaffordable for many households, even in developed countries. 760 million people still lack access to electricity today [13], notably in sub-Saharian Africa where 80% of the population lives without regular supply. The energy transition must allow to decrease those numbers, and ensure a reliable and stable supply of electricity that can meet demand at all times and at an affordable price.

This work does not have the ambition to tackle all aspects of the Doughnut, but aims at discussing the impact of the massive installation of VRES, notably on the access to energy with a focus on the security of supply. Moreover, it will not explore all VRES but will target one type in particular: **offshore wind energy**.

1.2. Scope, Motivation, and Research Questions

Offshore wind energy has the potential to deliver large amounts of low-carbon, renewable energy to fulfil a large part of future electrical needs. Offshore wind power has gradually progressed in many countries and further development is foreseen for the future. In 2023, 11 GW of new offshore wind power was added to the grid, bringing the total worldwide offshore wind capacity to 75.2 GW [14]. The rate of new offshore installations is expected to dramatically increase in the future, reaching 66 GW in 10 years, as shown in Fig. 1.4. Indeed, it has been estimated that to meet a 1.5°C-trajectory, the worldwide offshore wind capacity should reach at least 380 GW by 2030 and 2000 GW by 2050 [15]. Regarding Europe, the European Union has recently set targets for an installed capacity of at least 60 GW of offshore wind energy by 2030, and 300 GW by 2050 [16]. This is part of the European Union's plan to reach a climate-neutral economy with zero-net greenhouse gas emissions by 2050 [17]. It is important to keep in mind that all those targets assume an energy use that maintains the current high living standards in developed countries. However, a recent study showed that, with a combination of the most efficient technologies available and radical demand-side transformations that reduce excess consumption to sufficiency-levels, the final energy requirements for providing decent living standards to the global population in 2050 could be over 60% lower than consumption today [18].

Regarding Belgium, there are currently 9 offshore wind farms installed in the North Sea (399 wind turbines), as shown in Fig. 1.5, amounting to 2.2 GW of installed offshore capacity. The oldest turbines date from 2009 while the latest wind farms have been operating since 2020. They can generate in average 8 TWh of green electricity per year, i.e., 10% of the total electrical load or nearly 50% of the electricity needs of all Belgian households. Over its expected

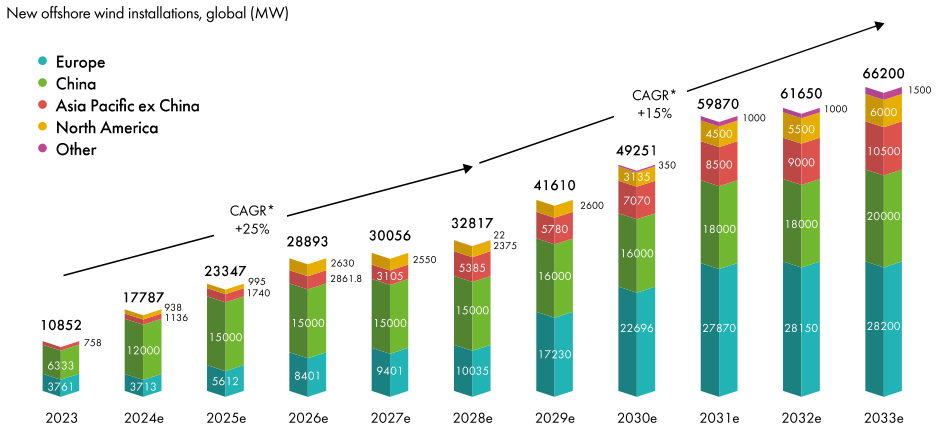

Figure 1.4.: Worldwide new offshore installations for the next 10 years [14] (*CAGR = Compound Annual Growth Rate).

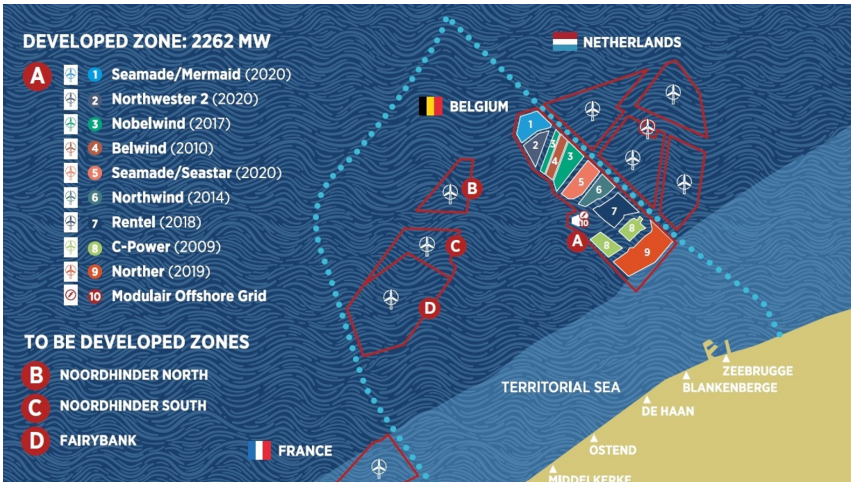

Figure 1.5.: Offshore wind farms location in the Belgian part of the North Sea, current cluster and the future Princess Elizabeth zone [19].

operational lifespan of 20 years, a wind farm emits 115 times less CO_2 than the current Belgian electricity mix and 175 times less than the most modern gas power stations [19]. Recent environmental studies have also shown that wind farms at sea do not have a significant negative impact on fish or other maritime fauna and flora [20]. Therefore, Belgium has set high targets of large-scale offshore wind for the future carbon-neutral electricity system. Indeed, despite having the smallest exclusive economic zone in the North Sea, Belgium has ambitious plans to further increase its offshore wind capacity in the coming decade. By 2030, the offshore production capacity is set to reach 6 or 8 GW

with the new Princess Elizabeth Zone (PEZ), which would allow to cover approximately 30% of the electrical consumption thanks to wind energy in the Belgian North Sea [21]. This new zone is represented by parcels B, C and D on Fig. 1.5.

However, even if offshore wind is stronger and more constant than in onshore conditions [22], it remains inherently intermittent and uncertain. The wind may not be blowing when the electricity from a wind farm is required, while it can be very windy and electricity is being produced even if energy is not needed (the turbines might have to be curtailed in that case). Adding to that the trend for nuclear dismantling, the decentralization of production and other challenges related to the energy sector, growing concerns are expressed regarding the reliability of future power systems. In the scientific literature, power system reliability is associated with two distinct concepts: **adequacy** and **security** [23]. On the one hand, adequacy represents the ability of the electrical system to satisfy load consumption in steady-state conditions [24]. In every considered state, it is supposed that the system conditions do not evolve, thus adequacy does not encompass dynamic behaviours. On the other hand, security assesses the ability of a power system to cope with severe and sudden perturbations, such as non-anticipated loss of system components or electrical short-circuits, while maintaining its integrity, i.e., without major service interruptions. Therefore, adequacy and security are two distinct concepts that mainly differ from each other with regard to the timescale: adequacy focuses on the long-term behaviour of a system (e.g., a 10 years horizon) while security relates to the response and integrity right after an unanticipated disturbance. A lack of adequacy leads to load shedding, i.e., *scheduled* power outages designed to prevent the failure of the entire system when the demand strains the generation capacity, while insufficient security can lead to power blackouts. Adequacy studies are traditionally carried out by the Transport System Operator (TSO) and policy-makers in order to evaluate the risk of generation shortage, thus assessing the need for investment in additional production units. In Belgium, Elia, the national TSO, biennially publishes its "Adequacy & Flexibility study" for an horizon of 10 years in the future [25].

By definition, a system is adequate if there is sufficient capacity to meet the relevant needs via different means including generation, imports, storage and demand side management. However, several challenges jeopardize the adequacy of the future Belgian power system. Firstly, a massive electrification is foreseen in the coming years, which will largely increase the electrical demand (from 83 TWh in 2023 to almost 130 TWh in 2034) [25]. Secondly, given its topography, limited area and dense population, Belgium's full VRES potential will not meet all of the country's future needs. Thirdly, Belgium relies heavily on

importations, which was not an issue in the past. However, given the fast pace at which foreign policy is evolving and the speed at which change in the European energy system is occurring, Belgium's security of supply becomes vulnerable to events happening abroad and to the availability of surplus generation across Europe at times of need in Belgium. All those challenges must be considered when Belgian policy-makers decide on investments to be made in the generation fleet and interconnections with other countries. The latest adequacy study carried out by Elia for Belgium has highlighted the need for new domestic capacity in the future [25]. However, the exact amount depends on scenarios and sensitivities regarding electrical consumption, VRES installation, nuclear phase-out, demand side response, storage, closure of thermal capacity and surplus in other countries. Because adequacy studies are usually carried out on an hourly basis, accurate generation profiles for VRES are crucial, and it is not sufficient to use the average production based on yearly capacity factors. Given the increased role of offshore wind generation in the future Belgian electricity mix, improving its modelling is essential, especially the hour-by-hour variations. Free-flow wind speed, wind direction and aerodynamic phenomena drive the production of turbines within a wind farm. Not accurately capturing power variations and losses due to those aerodynamic effects might lead to an overestimation of adequacy, thus hiding potential stressed conditions within the power system. Thinking back about the Doughnut, adequacy aspects ensure that a massive integration of offshore wind energy, even though beneficial against climate change, will not jeopardize access to energy.

A higher penetration of VRES generation also puts strain on security, as storms and rapidly changing weather conditions are expected to cause important system balancing challenges if not adequately managed [25]. Moreover, given the ambitions regarding a massive installation of VRES, more and more periods will occur during which the production of renewable electricity exceeds demand, which could lead to difficulties when trying to manage positive system imbalances (generation exceeds consumption). During the spring and summer months, when high levels of solar generation occur simultaneously in Belgium and its neighbouring countries, these difficulties will be particularly critical, making it difficult to export excess energy. Therefore, it is crucial to explore how to make sure that the generation of VRES is used in the most efficient way possible. Historically, balancing services were provided by thermal generation, typically gas-fired power plants in Belgium. However, considering the progressive phase-out of fossil fuel generators and the increasing penetration of weather-dependant electricity generation, the need for more security will intensify. Because offshore wind generation capacity is expected to grow steadily in the future, wind farm operators will have an important role in system balancing. Allowing offshore wind farms to participate in the reserve market will be of mu-

tual interest to TSOs and wind producers. Offshore wind farms were originally designed, optimized, and operated to produce maximal power, regardless of the current situation of the grid. However, it has been proven that variable speed wind turbines in modern wind power plants have intrinsic fast down (virtually at no cost) and ramping up (subject to the availability of wind power) capabilities, which can be effectively used to provide ancillary services [26], [27]. For example, during periods of overproduction, instead of producing at full capacity, wind farms should offer balancing services, e.g., derating turbines and keeping a power output margin available in case of sudden perturbations in the system, therefore not aggravating generation surplus. This aspect should be considered when designing the future offshore wind farms in the second Belgian offshore cluster. Moreover, coming back to the Doughnut, a more efficient operation of wind farms, avoiding spillage of renewable energy, could lead to a recalculation of security needs. This could then result in a reduction of requirements to build more generation means, thereby alleviating land use, mining demand and all associated negative effects on the environment.

Making accurate hourly power assessments with a very low computation time is crucial for assessing the impact of offshore wind farms on the supply of electricity. For computational reasons, offshore wind generation is often modelled in a simplified way in power system computations assessing the reliability of electricity supply. In problems involving iterative calculations, simplified offshore wind farm models often disregard complex aerodynamic effects. However, these effects have a significant impact on the produced electricity. Therefore, this thesis aims at developing novel formulations to answer the following research questions:

- *How can we improve the integration of future offshore wind farms in power systems by assessing their impact on the reliability of supply and their ability to provide balancing services ?*

Throughout this work, this main research question has been divided into three sub-questions. Each of the following research questions is addressed in the chapters of this dissertation:

- *How to model offshore wind farms in a fast and accurate way to capture complex aerodynamic phenomena while keeping a reasonable computation time ? (chapter 3)*
- *What is the impact of an improved modelling of offshore wind generation in adequacy studies aimed at assessing the reliability of electricity supply in future power systems ? (chapter 4)*
- *How can the layout of future wind farms be optimized to account for the participation to ancillary frequency services ? (chapter 5)*

Overall, the improved modelling of offshore wind generation could be applied to other power system computations. The objective is to enable a better integration of offshore wind production. The case studies are based on real-word Belgian offshore wind farms, as well as wind and market data from the Belgian power system, which allows performing quantitative observations. The presented research contributions and findings may be relevant to all wind farm operators, policy makers and system operators.

1.3. Research Objectives and Scientific Contributions

The goal of this thesis is to develop novel models for offshore electricity production in order to ensure a better integration of wind farms in future power systems. More specifically, this work establishes the three following research objectives.

- **Developing a fast and reliable topology-aware surrogate of offshore wind farms**
  The objective is to build a Machine Learning (ML) model for making accurate hourly power assessments with a very low computation time, but also able to generalize to unseen wind farm configurations (i.e. applicable to any offshore wind farm in the world, with the training process carried out only once).

- **Assessing the impact of a more accurate offshore wind generation modelling on power systems adequacy**
  This objective aims at integrating the ML surrogate model within adequacy studies, in order to study the impact of considering aerodynamic effects on reliability indices.

- **Designing future wind farm layouts considering the provision of frequency services**
  For this objective, a new formulation for Wind Farm Layout Optimization (WFLO) is developed to account for the participation of future wind farms to both day-ahead energy and reserve markets.

The accomplishment of these three complementary objectives provides a tool to model offshore wind farms for power system adequacy and security assessments. From a practical perspective, this research project would enable TSOs to have an accurate and tractable modelling of offshore wind generation when they carry out adequacy studies to assess the reliability of electricity supply in the future. Moreover, the surrogate model could be used by wind

farm operators willing to design future offshore projects in an optimal way and to estimate the yearly production of various layouts. By extension, this would benefit the integration of offshore wind farms in future power systems by ensuring a reliable supply of electricity for systems with a high share of offshore generation and by enabling wind farms to be designed and operated as to optimize the utility of the produced electricity. Considering these research objectives, we list the three main contributions with regard to the literature:

- **On a topology-aware wind farm surrogate**. A generic, topology-aware ML model is trained to accurately capture complex aerodynamic effects arising within offshore wind farms, encompassing various atmospheric conditions, heterogeneous turbine types and turbine failures. The model relies on an augmented set of features, including atmospheric, geometric, physics-informed, and turbine-specific characteristics, which makes it able to generalize to any farm configuration (even future farms that are not yet built). By externalizing the complexity from the model architecture to the input features set, the proposed model has a very low computation time in both training and inference stages, such that the ML model is applicable in problems involving iterative computations. The development of the model has resulted in the following contributions:
  - **T-H. Nguyen**, J-F. Toubeau, E. De Jaeger, and F. Vallée, "Topology-aware Surrogate for Future Offshore Wind Farms Using Machine Learning", submitted to *Applied Energy*
  - **T-H. Nguyen**, J-F. Toubeau, E. De Jaeger and F. Vallée, "Fast and Reliable Modeling of Offshore Wind Generation for Adequacy Studies," *IEEE Transactions on Industry Applications*, vol. 59, no. 6, pp. 7116-7125, 2023
  - **T-H. Nguyen**, N. Thils, J-F. Toubeau, E. De Jaeger, and F. Vallée, "Offshore Wind Farm Power Prediction for Security of Supply Assessment Using a Unique Machine Learning Proxy", *2022 EAWE PhD seminar*, Bruges, Belgium, 2022
- **On adequacy studies with improved offshore wind farm models**. The developed ML surrogate is embedded within adequacy studies using sequential Monte-Carlo simulations in order to assess the impact of an improved offshore wind generation modelling on reliability results. The generalization capabilities of the model are leveraged to account for uncertainties in the layout and turbine choice of future offshore wind farms. This is illustrated by an integration of the model into a long-term adequacy study aimed at assessing the reliability indices of a power system with a high share of offshore wind generation. For this part, those contributions have been proposed:

  - **T-H. Nguyen**, J-F. Toubeau, E. De Jaeger and F. Vallée, "Fast and Reliable Modeling of Offshore Wind Generation for Adequacy Studies," *IEEE Transactions on Industry Applications*, vol. 59, no. 6, pp. 7116-7125, 2023
  - **T-H. Nguyen**, G. Paternostre, J-F. Toubeau, E. De Jaeger, and F. Vallée, "Adequacy Computations for Power Systems with a High Share of Offshore Wind Generation: Application to Belgium", *2023 EAWE PhD seminar*, Hannover, Germany, 2023
  - **T-H. Nguyen**, J-F. Toubeau, E. De Jaeger and F. Vallée, "Adequacy Assessment Using Data-driven Models to Account for Aerodynamic Losses in Offshore Wind Generation", *Electric Power Systems Research*, vol. 211, 2022
  - **T-H. Nguyen**, J-F. Toubeau, E. De Jaeger and F. Vallée, "Machine Learning Proxies Integrating Wake Effects in Offshore Wind Generation for Adequacy Studies," *2021 IEEE International Conference on Environment and Electrical Engineering and 2021 IEEE Industrial and Commercial Power Systems Europe (EEEIC / I&CPS Europe)*, Bari, Italy, 2021

- **On wind farm layout optimization accounting for reserve markets**. A new formulation for computing the optimal offering, reserve allocation strategy, and subsequent expected profits of a wind farm participating in both day-ahead energy and reserve markets is developed. It considers the uncertainty in forecasts of wind power, electricity prices and activated reserve volumes. The estimated penalties and balancing costs for failing to provide energy and reserve are also taken into account. This formulation is used as the objective function of a wind farm layout optimization maximizing yearly profits, and applied on a real wind farm using historical data for wind and electricity prices. This part led to the following contribution:
  - **T-H. Nguyen**, J. Quick, P-E. Réthoré, J-F. Toubeau, E. De Jaeger and F. Vallée, "Offshore Wind Farm Layout Optimization Accounting for Participation to Secondary Reserve Markets", submitted to *Wind Energy Science*

The complete list of publications can be found at the end of this manuscript in Appendix A.

1.4. Thesis Outline

The organisation of this thesis manuscript is the following:

- **Chapter 2** firstly introduces the basics regarding offshore wind farms design and operation, as well as their integration within power systems.
- **Chapter 3** presents the topology-aware wind farm surrogate, built upon aerodynamic simulations of wind farms using supervised Machine Learning techniques. The developed models are assessed and compared with high-fidelity simulations and data of real offshore wind farms.
- **Chapter 4** is focused on improving the modelling of offshore wind generation within adequacy studies and studying the impact on reliability indices. The case study is based on the Belgian power system in 2030.
- **Chapter 5** details a novel formulation for wind farm layout optimization accounting for provision of frequency reserve.
- **Chapter 6** concludes this report, while offering some perspectives for future research.

CHAPTER 2.

Offshore Wind Farms Design and Operation

Wind energy has been used for millennia by successive cultures and civilizations [28]. Since early history, wind power has been exploited by seamen for sailing boats on rivers and lakes and then ships at sea. Windmills primarily refer to wind-powered machines that grind or mill grain and turn it into flour for bread making. But windmills have also had numerous other applications such as grinding spices, sawing timber, pressing oil, mines ventilation, shredding tobacco, and water pumping in the pre-industrial revolution era [22]. However, it was not until late in the 19th century that several inventors on both sides of the Atlantic focused on harnessing the wind to generate electricity. Within a few months of each other, the first wind turbines built for generating electricity were installed in Scotland and France, soon followed by one in the United States and a few years later by one in Denmark. The very first known wind turbine to produce electricity is generally credited to Professor James Blyth, a Scottish electrical engineer [29]. Blyth's 10 m high, cloth-sailed wind turbine was installed in the garden of his holiday cottage at Marykirk (shown in Fig. 2.1). It was used to charge accumulators that powered the lighting in the cottage, thus making it the first house in the world to have its electricity supplied by wind power. However, the invention never really caught on as the technology was not considered to be economically viable, and no more wind turbines were built in the United Kingdom until 60 years later. Actually, with the exception of the work in Denmark, none of these early experimentation resulted in any lasting technological development.

Back in the 19th century, no one would have guessed that there would be, today, more than 1 TW of wind power capacity worldwide (1021 GW), with 117 GW of new installations for 2023 only [14]. At the current rate, the goal is to reach 2 TW before 2030. Around 20% of the final energy we consume in the world is for generating electricity and it comes from different sources.

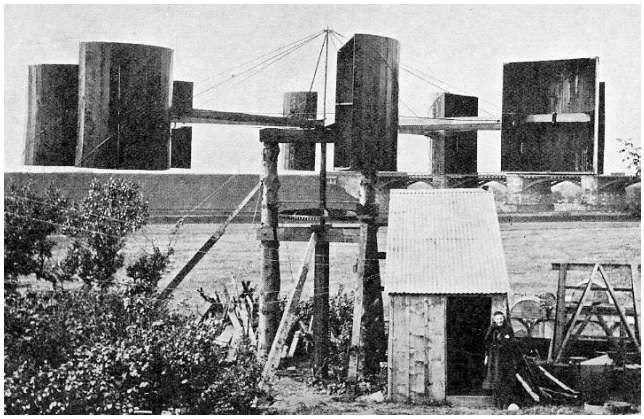

Figure 2.1.: Blyth's wind turbine at his cottage in Marykirk in 1891 [29].

Among renewable sources, the share of electricity coming from wind turbines is about 7.8% [13], [30]. In Belgium, the electricity share in the final energy consumption is 17.4%, among which 18.9% came from onshore and offshore wind turbines [31].

Regarding offshore wind generation, the first offshore wind farm in the world was constructed in Denmark, off the coast of Lolland, in 1991, for an estimated cost of 10 million euros [32]. The Vindeby Havmøllepark consisted of 11 wind turbines of 450 kW each, for a total capacity of almost 5 MW. It was decommissioned for cost reasons in 2017 after 25 years of electricity production. Nowadays, offshore turbines usually have a rated power of several MW, and are expected to reach up to 20 MW in the future [33]. Currently, offshore wind capacity is only 75 GW (i.e., 7% of total wind power) but it has developed rapidly in the past few years (as seen in Fig. 2.2) and it will continue to do so. Indeed, to meet a 1.5°C-trajectory, the world will need at least 380 GW of offshore wind by 2030 and 2000 GW by 2050 [15]. Belgium has been a pioneer when it comes to large offshore wind farms. C-Power, the first Belgian farm, was installed in 2009, for a rated capacity of 325 MW. Ten years later, in 2020, Belgium ranked fourth of the countries with the most offshore wind power in total installed capacity (behind the United Kingdom, Germany and China, and ahead of Denmark and the Netherlands), with a total installed power of 2262 MW [19].

This chapter is structured as follows. The production of electricity from wind is discussed in section 2.1. The wind turbine is described, as well as the main governing equations and the power curve. Section 2.2 details the characteristics of offshore turbines, and the main challenges related to offshore conditions. In section 2.3, resource assessment of a wind site is discussed. Indeed, the

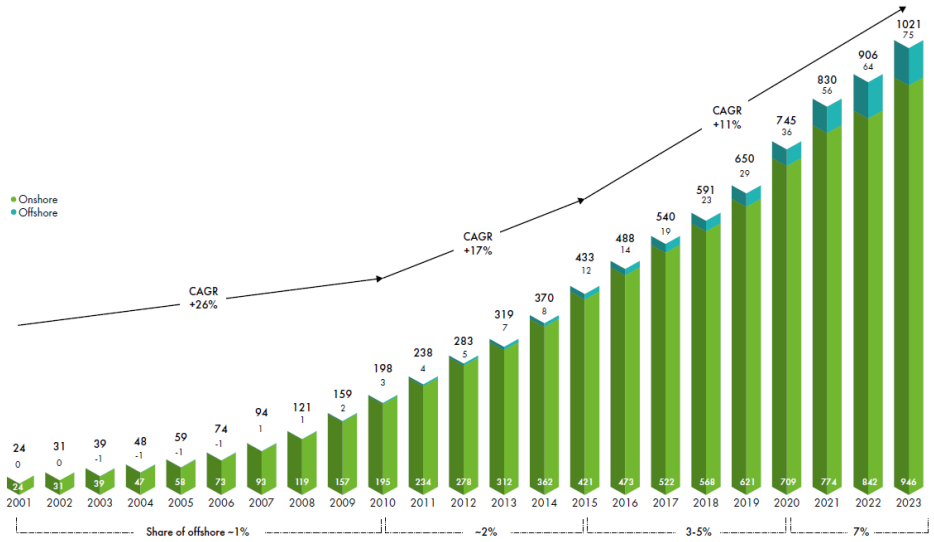

Figure 2.2.: Historic development of onshore and offshore wind worldwide [14].

ability to measure and assess available wind resources at a given location is crucial to the development, siting, and operation of a wind farm. Aerodynamic effects arising within an offshore wind farm are examined in section 2.4. Wake effects and turbulence have a high impact on the electrical output of interacting turbines. Section 2.5 describes the design process of an offshore wind farm, notably the layout (turbine placement, choice of turbine model). In section 2.6, the operation of current offshore wind farms is presented, and future possible control strategies are considered. Finally, section 2.7 concludes this chapter.

2.1. Harvesting Energy from the Wind

Wind is atmospheric air in motion, caused by the uneven heating of the Earth's surface by solar radiation. The velocity of the air motion defines the strength of wind and is directly related to the amount of mechanical kinetic energy in the wind, given by:

$$E_{k,wind} = 0.5\, m_{air} * u^2 \tag{2.1}$$

where m_{air} is the mass of air and u is the wind speed. We define a control volume as a stream tube (cylinder) of cross-section area A through which air is flowing at velocity u. The mass flow rate of air through the control volume is

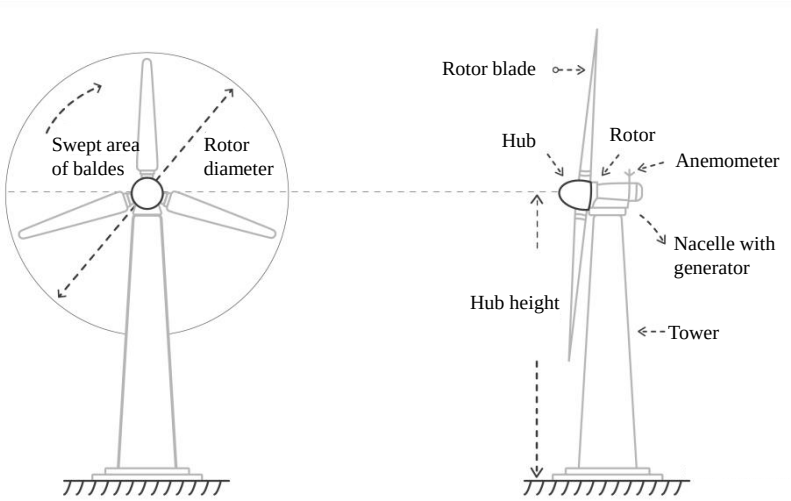

Figure 2.3.: Front and lateral view of an horizontal axis turbine with 3 blades.

given by:

$$\frac{dm_{air}}{dt} = \rho_{air} * A * u \tag{2.2}$$

where ρ_{air} is the air density. The wind power in the flow, i.e., the kinetic energy flowing per unit of time, can thus be written as:

$$P_{k,wind} = \frac{E_{k,wind}}{dt} = 0.5 * \rho_{air} * A * u^3 \tag{2.3}$$

A wind turbine is a machine which converts this kinetic power in the wind into electricity. The conversion process uses the aerodynamic force of lift on turbine blades to produce a net positive torque on a rotating shaft, producing first mechanical power and then transforming it to electricity with a generator. Nowadays, the most common design of wind turbine is the horizontal axis wind turbine (the axis of rotation is parallel to the ground) with 3 blades, pictured in Fig. 2.3. The cross-section area A is then defined as the area swept by the turbine blades and R_{WT} is the rotor radius.

However, not all kinetic power is available for utilization. The efficiency in wind power extraction is quantified by the power coefficient C_p, which is the ratio of power extracted by the turbine to the total power of the wind resource $C_p = P_{turbine}/P_{k,wind}$. Therefore, turbine power is given by:

$$P_{turbine} = 0.5 * \rho_{air} * \pi * R_{WT}^2 * u^3 * C_p \tag{2.4}$$

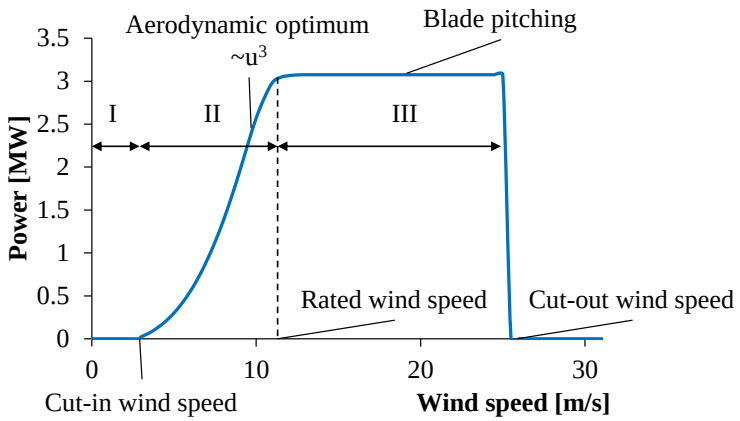

Figure 2.4.: Power curve of the Vestas V112-3MW turbine (data from [36]).

There is a theoretical upper limit on the maximum extractable power fraction, known as the Betz Limit. According to Betz's theory [34] the maximum possible power coefficient C_p is equal to $16/27$, i.e., 59% efficiency is the best a wind turbine can do in extracting power from the wind.

The power output of a wind turbine varies with the wind speed and every turbine has a characteristic power performance curve. With such a curve it is possible to predict the energy production of a wind turbine without considering the technical details of its various components [35]. The power curve gives the electrical power output as a function of the free-flow wind speed at hub height. Fig. 2.4 shows the ideal power curve of a turbine with regard to incoming wind speed. It can be observed that wind turbines are controlled to operate only in a specified range of wind speeds bounded by the cut-in (u_{ci}) and cut-out (u_{co}) speeds, respectively the minimum wind speed at which the machine will deliver useful power and the maximum wind speed at which the turbine is allowed to deliver power for safety constraints. Beyond these limits, the turbine should be stopped to protect both the generator and the turbine.

There are three different operational regions shown in Fig. 2.4 (but more regions are sometimes defined). Region I is the low-speed region, where the turbine should be stopped and disconnected from the grid to prevent it from being driven by the generator. When the incoming wind reaches the cut-in speed, the wind turbine relaxes its braking after passing through this region and starts up. Region II is the moderate-speed region that is bounded by the cut-in speed at which the turbine starts working, and the rated speed (u_r), at which the turbine produces its rated power (generally the maximum power output of the electrical generator). The turbine produces its maximal power in this region, as it is controlled to fully extract the available power from the wind.

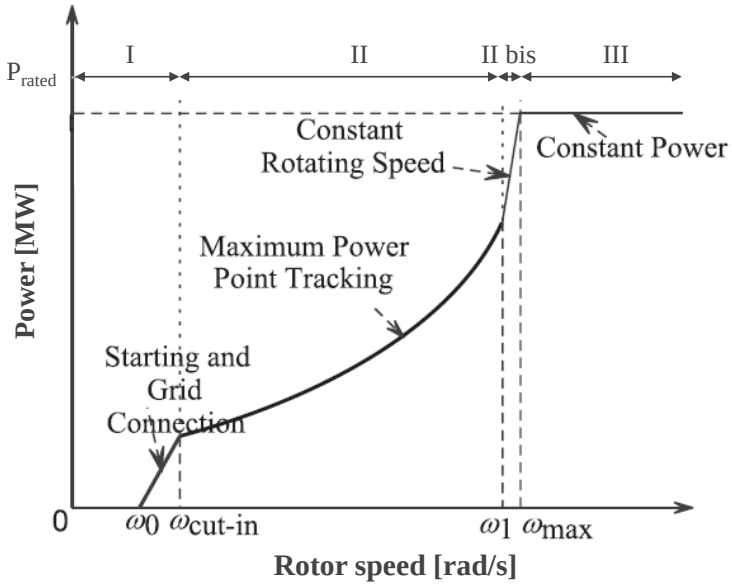

Figure 2.5.: Power curve with regard to rotor speed of a variable speed turbine: wind turbine control mode in different operating regions [37].

Although the speed of the wind turbine could be fixed or variable, maximization of the extracted energy in this region is only achievable with variable rotating speed wind turbines. Since these turbines can change their rotational speed to follow instantaneous changes in wind speed, they are able to maintain a constant rotational speed to wind speed ratio. Fig. 2.5 shows the power curve with regard to rotational rotor speed (and not incoming wind speed, as it was the case in Fig. 2.4). In region II, the Maximum Power Point Tracking (MPPT) control is implemented to ensure that the wind turbine operates under the maximum power coefficient. There are several MPPT control algorithms to determine the optimal operating point of the wind turbine (tip speed ratio control, optimal torque control, perturbation and observation control, ...). In Region II bis, the wind turbine maintains the maximum allowable speed, but the output power of the wind turbine does not reach the maximum limit, which is generally realized through variable-pitch control. In region III, the high speed region (i.e., between rated and cut-out), the turbine power is limited so that the turbine and generator are not overloaded and dynamic loads do not result in mechanical failure. The wind turbine reduces the rotor speed when the wind speed increases by adjusting the pitch angle so that the power can be kept constant. Above the cut-out speed, the turbine should be shut down to protect it from structural overload. Power curves for existing machines can generally be obtained from the manufacturer.

2.2. Building Wind Turbines Offshore

An offshore wind turbine is typically installed at sea, although the term also comprises inshore water areas such as lakes, fjords and sheltered coastal areas. In fact, a wind turbine shall be considered as an offshore turbine if the support structure sustain hydrodynamic loading.

The main reason for seeking offshore conditions is the higher wind speeds offshore than on land, due to the absence of land mass obstacles and the lower surface roughness of water compared to land features (forests, buildings, ...) [38]. The wind speed is also less prone to variations (e.g., diurnal cycle) and the wind direction is more constant, thus alleviating the need to redirect turbines to face the wind. This allows offshore farms to generate more electricity per capacity installed, thus enhancing efficiency and leading to less negative impact for materials and land use. Regarding mining requirements, the amount of rock that has to be mined for the extraction of materials is lower for offshore (34.88 tons per GWh of electricity generated) than for onshore turbines (59.48 t/GWh) [39]. The quantity of materials needed is also lower for offshore wind power (1.95 t/GWh, among which 1.79 t/GWh of steel) than for onshore turbines (7.09 t/GWh) that require a lot of concrete (5.14 t/GWh). Improvements in offshore turbine technology (e.g., larger turbines with longer blades and higher hub heights), along with access to better wind resources, result in a global weighted average capacity factor of 35% for offshore wind farms in Europe, against 23% for their onshore counterparts [40]. However, the average load factor for new wind installations built in 2022 in Europe is expected to reach almost 50% for offshore farms [41]. There is thus a vast wind energy potential in open waters. Moreover, offshore wind turbines have less impact on people and the landscape and are thus more prone to public acceptance. Being miles out from the coast, offshore turbines are further away from the local population. It has also been shown that there are no significant negative environmental impact and restricted access to offshore sites may even help to protect the surrounding marine ecosystems [20].

However, the cost of offshore wind has historically been higher than for onshore [22]. Indeed, offshore wind farms face more challenging conditions throughout installation, commissioning, operation and maintenance, due to the harsh marine environments. Their offshore locations complicate construction and grid connection, further adding to their planning and project development complexity. Therefore, offshore wind projects tend to have significantly longer lead times and higher costs than onshore wind projects. The latest report of the International Renewable Energy Agency indicates a Levelized Cost of Energy (LCOE) of 0.075$ per kWh for offshore wind, against 0.033$ per kWh for

onshore [42]. LCOE is a metric used to assess the cost of electricity generation and the impact from technology design changes, and to compare costs of all types of generation. LCOE combines costs and energy production into one metric, and its computation is expressed as follows [42]:

$$LCOE = \frac{\sum_{t=1}^{n} \frac{I_t + M_t + F_t}{(1+r)^t}}{\sum_{t=1}^{n} \frac{AEP_t}{(1+r)^t}} \tag{2.5}$$

where:

- I_t are the investment expenditures in the year t [$]
- M_t are the operation and maintenance expenditures in the year t [$]
- F_t are the fuel expenditures in the year t [$]
- AEP_t is the electricity generation in the year t [kWh]
- r is the discount rate [%]. It is used to determine the present discounted value of a payment or revenue flow made in the future.
- n is the lifetime of the system [years]

The LCOE of renewable energies varies by technology, country and project, based on the renewable resource, capital and operating costs, and the efficiency/performance of the technology. This difference in LCOE between offshore and onshore wind mainly comes from the total installation costs. The breakdown of offshore wind farms total installation costs is presented in Fig. 2.6, where the variability comes from studying projects from different years and countries.

Development costs, which include planning, project management, insurance during construction, and other administrative costs, represent 2 to 9% of total installation costs. Indeed, data must be collected on seabed characteristics and at site locations for the offshore wind resource assessment, while obtaining permits and environmental consents entails great complexity and can be time consuming. Foundations are major cost items: they typically cost 15% to 20% of the overall project, as offshore wind farms are inherently installed in challenging settings and their foundations need to be well designed and installed because the costs of reworking (corrections and maintenance) can be enormous. Offshore turbines represent approximately 35 to 45% of the overall project costs. Electrical interconnection (collection system, array cables,

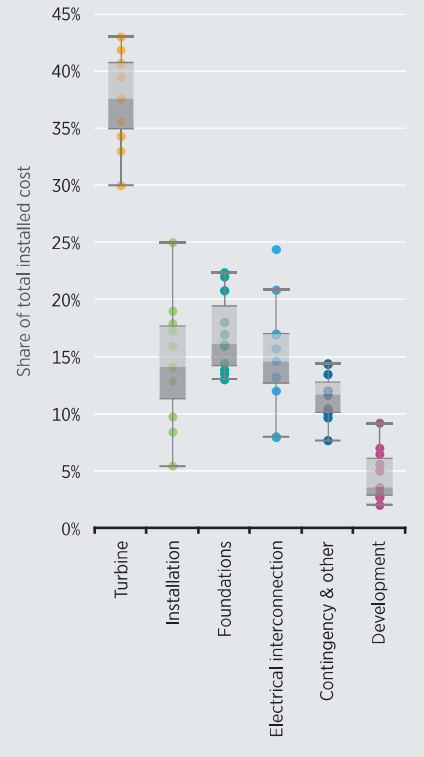

Figure 2.6.: Representative offshore wind farm total installed cost breakdown in the world between 2013 and 2021 [42].

export cables) accounts for 10 to 20%. Installation costs themselves have a large variability: they range between 5 to 25% of the project expenditures. The expense of transporting, operating and installing foundations and turbines offshore, along with the distance to port, are major contributing cost factors. Indeed, installation requires specialized ocean craft, e.g. jack-up vessels, to transport and install the components. These specialized crafts are costly and require a lot of planning because of their scarcity but high solicitation.

2.3. Resource Assessment

The ability to measure and assess available wind resources (wind speed, wind direction, turbulence, stability, ...) at a given site is crucial to the development, siting, and operation of a wind farm. It allows to determine project feasibility, select appropriate equipment and estimate the energy production of a wind farm. Wind resource can be assessed from on-site measurements with meteorological masts, turbine sensors, LiDARs, ... However, the use of meteorological masts

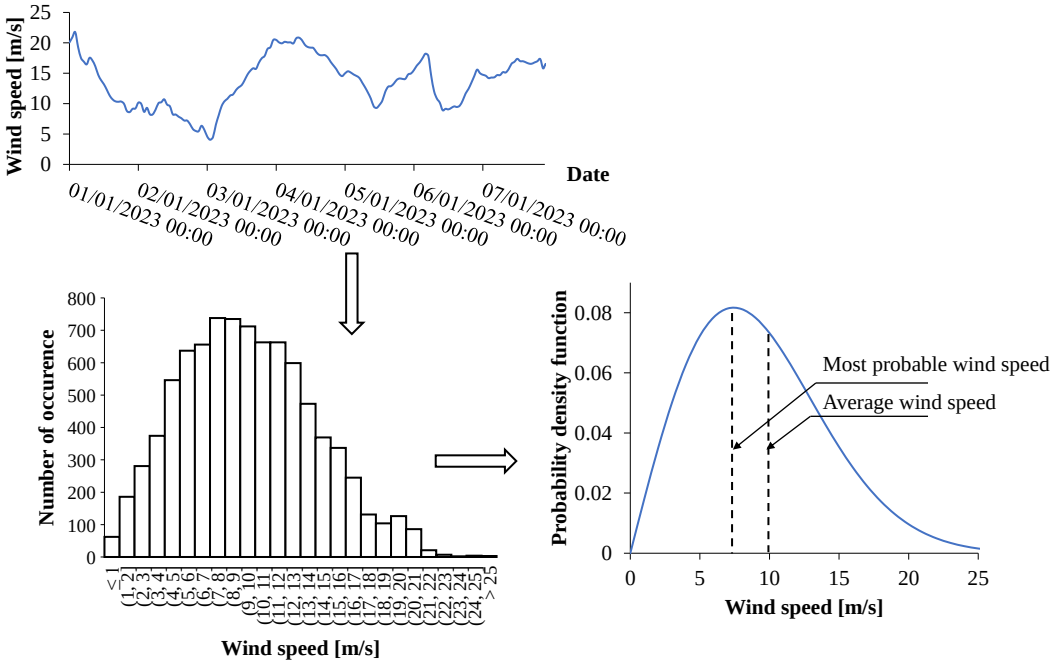

Figure 2.7.: Long term statistics of mean wind speeds. From time series, histograms are plotted and from histograms, the probability density function of a Weibull distribution can be deduced.

can be costly for offshore conditions, where a platform must be set up to install the instrumentation. LIDARs are able to capture the wind speed and direction at specified heights: floating platforms equipped with them could be a viable alternative to deploying costly masts to capture the offshore wind potential [43]. Weather models and wind resource maps can also be leveraged for wind resource assessment. When the wind speed regime (long term hub height wind speeds) has been established, the electrical energy production can be estimated by using wind turbine power curves supplied by manufacturers. The frequency distribution of wind speeds can help developers choose the most adequate turbine model for the assessed site. Usually, the distribution of wind can be approximated by a Weibull law, which gives the probability of wind speed being inferior to u:

$$p(u) = \frac{k}{\alpha} * \left(\frac{u}{\alpha}\right)^{k-1} * e^{-(u/\alpha)^k} \tag{2.6}$$

where α is the scale factor and k is the shape factor (≈ 2 in Northwestern coastal Europe). Fig. 2.7 shows the process of plotting a histogram from historical times series of measured wind at a given site, then deducing the

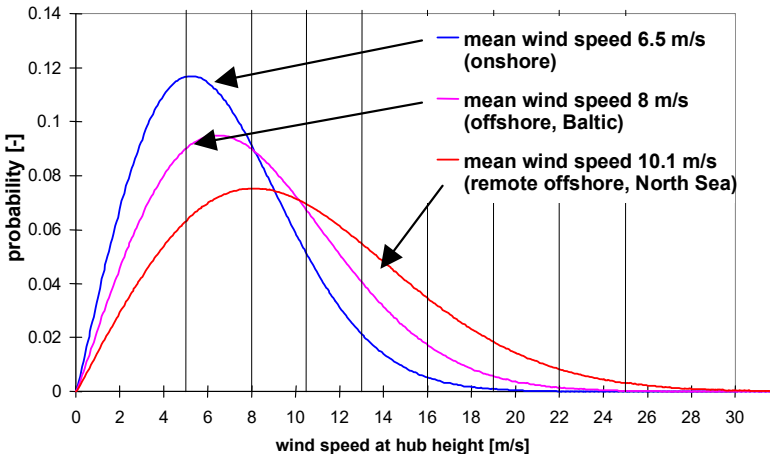

Figure 2.8.: Examples of Weibull distribution of wind speed, onshore and offshore [44].

Weibull law associated with the location. As it was stated before, offshore wind tends to blow stronger than in onshore conditions. This can be seen on Fig. 2.8, where the Weibull probability distributions are very different in shape and values between offshore and onshore conditions: the onshore curve is more narrow, with a lower wind speed and reduced probabilities of higher wind speeds (probability of speeds exceeding 14 m/s under 2%). The offshore curves are broader, especially the one depicting the North Sea wind regime, and the most probable wind speed is around 8 m/s while high values can reach up to 28 m/s.

It should be noted that measuring wind at turbine hub height is not always possible, especially for modern offshore turbines whose hub can reach up to 145 meters [45]. In that case, wind speed profiles (vertical extrapolation) can be deduced with the power law:

$$u(z) = u(z_{ref}) * (\frac{z}{z_{ref}})^{\alpha} \tag{2.7}$$

where $u(z)$ is the wind speed at height z, and $u(z_{ref})$ is the measured wind speed at a reference height z_{ref}. The shear coefficient α is an empirically derived value that varies depending on the stability of the atmosphere. For neutral offshore conditions, α is approximately equal to 0.11 [22].

Although Weibull wind speed distributions give an insight on the mean wind speed regime, it does not describe annual (seasonal), diurnal and short-term variations. Significant variations in seasonal or monthly averaged wind speeds

are common over most of the world. For offshore conditions in the North Sea, wind tends to blow stronger in winter months and can be still for long periods during summer [25]. The diurnal variation is typically an increase in wind speed during the day and the lowest wind speeds during the hours from midnight to sunrise (due to the heating of the ground). However, it is less visible above sea because of the large thermal capacity of the water (the sea-surface temperature is more likely to remain stable) [46]. Short-term variations usually mean variations over time intervals of 10 minutes or less. Turbulent fluctuations in the flow need to be quantified for the turbine design considerations of maximum load, fatigue prediction, structural excitation, control, system operation, and power quality. Turbulence in the wind is caused by dissipation of the wind kinetic energy into thermal energy via the creation and destruction of progressively smaller eddies (or gusts). The most basic measure of turbulence is the ambient turbulence intensity TI_u. It is defined by the ratio of the standard deviation σ_u of the wind speed to the mean $\bar{u}$:

$$TI_u = \frac{\sigma_u}{\bar{u}} \tag{2.8}$$

The length of the time period for computing the mean and standard deviation is normally no more than an hour, and by convention, it is usually equal to 10 minutes in wind energy engineering [35]. Turbulence characteristics vary significantly depending on the stability of the atmospheric boundary layer. The atmospheric stability is characterized by the vertical gradient in potential temperature, θ, which is a measure for comparing the temperature of air at two different heights. Positive, zero, and negative values of $\partial\theta/\partial z$ correspond to respectively stable, neutral, and unstable atmospheric conditions [47]. Onshore, unstable conditions often occur during the day when the sun-heated planetary surface transfers heat to the layer of adjacent air, while stable conditions are usually observed at night when the planetary surface and the adjacent air cool. In offshore conditions, unstable atmosphere occurs when cool air passes over relatively warm ocean water while stable conditions exist when warm air passes over relatively cool ocean water.

2.4. Aerodynamic Effects in Offshore Wind Farms

Wind farms are locally concentrated groups of wind turbines that are electrically and commercially tied together. While there are many advantages to this electrical and commercial structure (such as concentration of repair, maintenance equipment and spare parts, reduced labour costs per turbine, increased

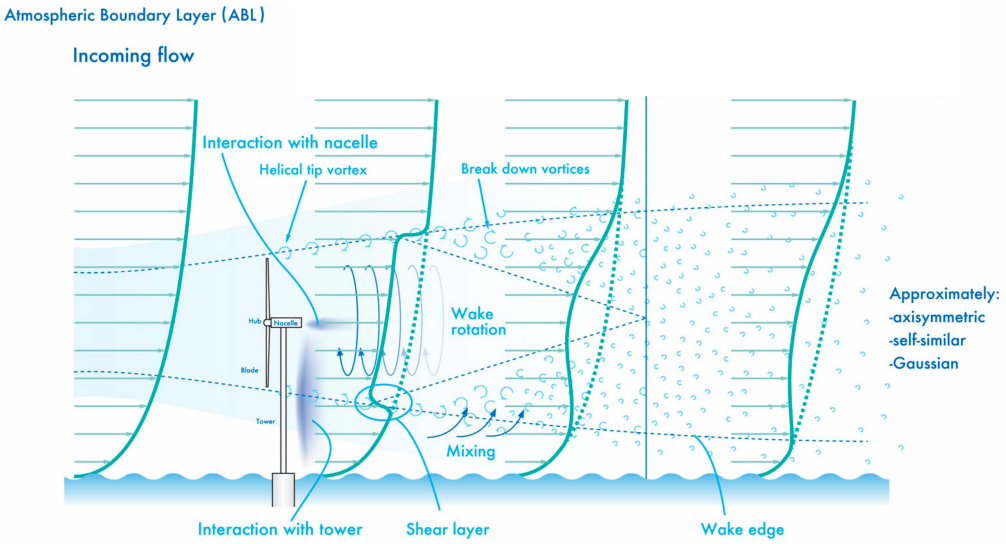

Figure 2.9.: Schematic side view of a wake structure behind a wind turbine [48].

exploitation of areas with profitable wind resources), wind farms are subjected to complex aerodynamic phenomena. As wind flows through a wind turbine and mechanical energy is extracted, the volume of air downwind of the turbine has a lower wind speed than the freestream flow. This volume of air is called a wind turbine wake [49], it is depicted in Fig. 2.9. Moreover, turbine wake flows lead to a substantial increase in the level of downstream turbulence intensity with respect to the turbulence level of the incoming atmospheric boundary layer flow. This effect has been observed in several numerical and experimental studies [50]. As the volume proceeds downstream, it spreads and energy is transferred inwards from the rim such that the difference between the lower energy/higher turbulence wake air and the freestream is gradually reduced. The size and degradation of wake structures depends on many factors such as the ambient wind speed and turbulence. Indeed, higher levels of ambient turbulence intensity leads to more mixing downward, which is favourable to wake dissipation and recovery of the flow. Wake added turbulence, turbine type, terrain, structure of the boundary-layer relating to atmospheric stability, and flow direction are other factors influencing wake propagation. However, it has been shown that after a distance equivalent of approximately 20 rotor diameters, the wake has recovered towards free stream conditions [51]. Moreover, as wakes move downstream, they impact the ground and are subject to downstream and lateral merging with other wakes. Indeed, depending on the wind direction, wind turbines inside wind farms are often exposed to multiple wakes from

Figure 2.10.: Wake effects observed within Horns Rev.
Photo credit: Vattenfall Wind Power, Denmark.

several upstream wind turbines. Fig. 2.10 depicts turbine wakes at Horns Rev, an offshore wind farm in the North Sea, west of Denmark. Particular meteorological conditions allow wake visualization by natural cloud formation.

Within a wind farm, the most obvious effects of wakes are the resulting lower power: wake losses refer to the loss of energy generation capacity of the downstream turbines due to these wake effects. A wind farm will not produce 100% of the energy that a similar number of isolated turbines would produce in the same prevailing wind. Farm wake losses are mainly a function of wind turbine spacing (both downwind and crosswind), wind turbine operating characteristics, wind farm size and density, and turbulence intensity. Moreover, power losses are also a function of the annual wind direction frequency distribution. The crosswind (perpendicular to the direction of incoming wind) and downwind (parallel to wind direction) distances between wind turbines will vary depending on the geometry of the wind farm layout and the direction of the wind. Yearly wake losses need to be calculated based on representative annual wind direction data in addition to wind speed and turbulence data. Wake losses are a major issue for offshore wind farms, as the lower roughness at sea reduces the atmospheric turbulence intensity and leads to generally stable atmospheric conditions. Measured values of the turbulence intensity range between 7 and 9% at 15 m/s for neutral offshore conditions in the North Sea [52]. Power losses due to turbine wakes in large offshore wind farms are predicted by state-of-the-art models to be in the order of 10–20% of the total potential power output, hence they are a significant component of the overall economics of large wind farms [53].

Another consequence of wakes are higher mechanical constraints at turbines experiencing wakes compared to those in freestream flows. Even though ambient turbulence is usually lower in offshore conditions, this may not result in reduced loads on offshore wind turbines due to high levels of wake-generated turbulence in large wind farms. Therefore, the dynamic loading increases significantly for offshore wind farms due to the more turbulent wake of upstream turbines, and hence impacts turbine lifetime. High load fluctuations are especially observed when the swept area of a turbine is partly covered by a wake. Measurements at the Vindeby offshore wind farm indicate that the relative increase in wake turbulence is considerably higher offshore and is more persistent downstream due to the lower ambient turbulence [44].

2.5. Design and Layout Configuration

The upfront costs of offshore wind farm projects are enormous and the initial development costs to mature the project are also significant when compared with onshore renewable development. Offshore wind planning is typically a long process that can take eight to ten years before the offshore wind farm begins generating power. The design phase is thus crucial to ensure that investment costs are compensated throughout the farm lifetime.

2.5.1. Site Choice and Development Phase

Selecting an appropriate location is the first step for building an offshore wind power plant: it requires a complex planning process that is based on diverse environmental, social, and economic factors. Government agencies are central in determining offshore wind farm concessions and in the tendering process. Site selection refers to the process by which government agencies outline offshore wind farm concessions: location, size and number of parcels. This is carried out according to a marine spatial plan and preliminary studies. Maritime spatial planning is a tool to coherently manage the use of seas and oceans and to ensure that human activities take place in an efficient, safe and sustainable way. Fig. 2.11(a) shows the marine spatial plan for the horizon 2020-2026 in Belgium. It can be seen that in the Belgian part of the North Sea, space is scare and determining zones for the production of offshore wind energy must respect constraints for shipping routes, nature protection areas, extraction areas, and zones for commercial and industrial activity. This explains why offshore wind farms are often gathered in clusters, which reduces power production because of wakes losses between neighbouring farms, but facilitates planning and site selection. Even for countries with longer coasts, clustering offshore wind power plants is a common practice, as it can be seen in Fig. 2.11(b), which indicates

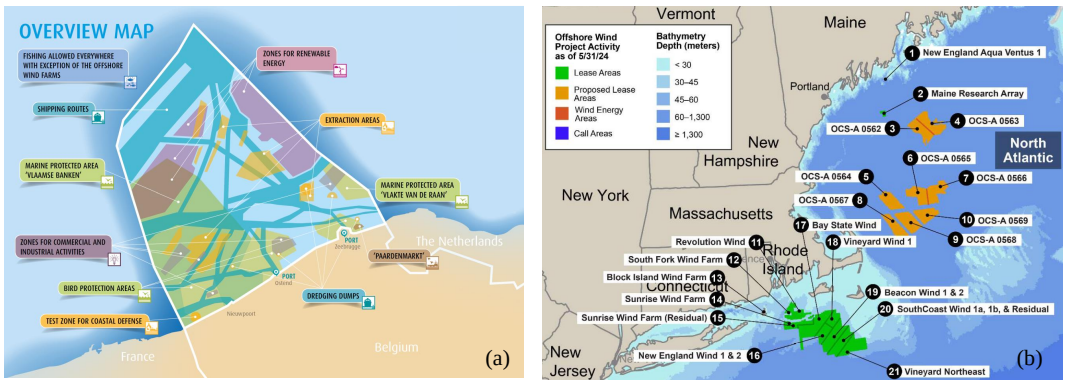

Figure 2.11.: (a) Map of the Marine Spatial Plan (2020-2026) for the Belgian North Sea [54], (b) Locations of US offshore wind energy pipeline activity and Call Areas as of May 31, 2024 in the North Atlantic Sea [55].

the locations of future US offshore wind farms in the North Atlantic.

Once concessions (or lease areas) have been determined by governments, they are awarded to offshore wind farm operators through a tendering process. Candidates submit bids for gaining support from the government for the project they intend to build, then bids are ranked according to bid values. Those bids should conform to admissibility (pre-qualification) criteria such as:

- Technical capacities: the bidder must have previous experience for large-scale offshore projects. This allows to limit the risk of project delays or non-execution
- Financial stability: minimum amount of assets and proof of financial strength through a provision of guarantee.
- Minimum installed capacity: the bidder will have to demonstrate that the minimal capacity fixed for the concerned parcel by the government will actually be built into its project.
- Maximum strike price: in case of support mechanism, this is a guaranteed price for offshore energy producers. If wholesale electricity markets fall under the strike price, wind farm operators receive the difference between the two prices for every produced MWh, usually for a fixed period of time (several years). This mechanism is usually used in contracts for differences (CfD) that can be one-sided (the government pays the producer in case of low electricity prices) or two-sided (producers also pay the government if prices reach the strike price, potentially with an added margin), as

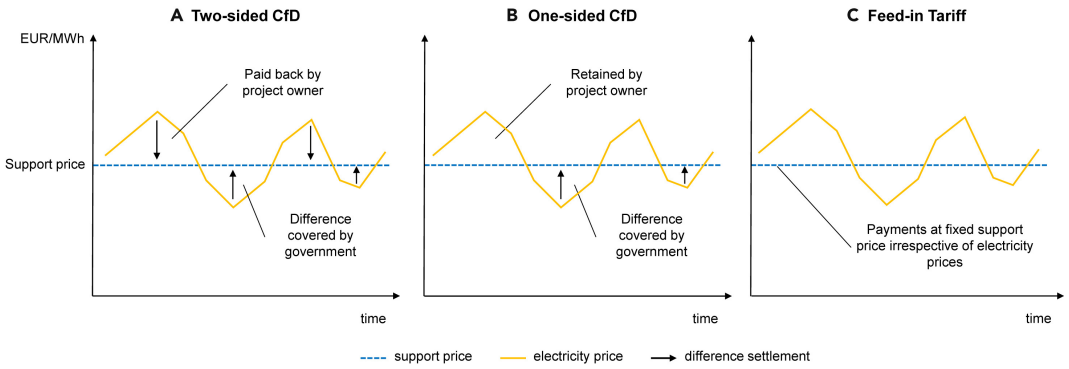

Figure 2.12.: A simplified illustration of different support mechanisms: (A) Two-sided CfDs, (B) One-sided CfDs, and (C) Feed-in Tariffs [56].

illustrated in Fig. 2.12. A maximum strike price set by the government is imposed on the bids: tender bids with a strike price higher than the predetermined maximum are automatically considered as unacceptable.

Candidates willing to participate to the auction make bids, where they stipulate the characteristics of their projects. They study the viability and profitability of the envisioned wind farm, with a view to the tendering process, as well as the management of the different actors or stakeholders involved. This includes environmental planning, site design, assessment of wind potential, technology review and component selection. As it was explained in section 2.3, a thorough knowledge of wind resources in an area is fundamental as it allows an estimation of the wind farms productivity and therefore the financial viability of the project. Marine aspects such as water depth, wave spectrum, ocean floor mapping, and geophysical surveys are also examined as they constrain turbine siting, suitable types of foundations, and choice of technology. At the end of the tender period, bids are then ranked according to awarding criteria, which depend on the type of tender and are set up by the government. They vary between countries and years but existing criteria include strike price, expected amount of energy produced, but also qualitative criteria such as environmental benefits (marine mammals, sea birds, flora), local content (contribution to secure skilled workers and local benefits), citizen participation, system integration benefits, envisaged commissioning date, ... A price-based ranking has the advantage that only the bids with the lowest prices will be awarded, which leads to a cost-effective selection. In a purely price-based auction, any additional objectives for the promotion of renewable energies can only be controlled via pre-qualification requirements outside the auction system. While there is no consensus on the ideal tender design system, auctions generally aim at achieving competitive prices (cost-competitiveness criterion) and high realisation rates (efficiency

criterion). They should also promote research and innovation efforts and allow for the development of cutting-edge wind technologies. The winning bidder receives the permission and the necessary permits for the construction and operation of the offshore installations for the duration of the lease.

In Belgium, no tender process were used for the first 9 offshore wind farms built before 2021: concessions could be requested and were granted without a tendering process, according to a Royal Decree [57]. Bidders had to demonstrate financial capacity, respond to technical criteria, and prove previous references and technical means. The award criteria were technical and environmental conformity, quality of the project, maintenance plan, and provisions for end-of-life dismantling. For the Princess Elizabeth Zone (second wave of offshore wind farms foreseen to be built by 2030), a Royal Decree published in June 2024 sets the rules for the tendering process [58], and the auction for the first parcel (700 MW) is scheduled for the end of 2024. Admissibility criteria include a strike price below 95€/MWh, previous experience for offshore wind projects of at least 300 MW, proof of financial stability (guarantee of 70 millions euros), demonstration that the minimal capacity decided for the parcel will actually be built into the project, and citizen participation (a minimum share of 1% of the investment costs of the entire project should be opened to citizen participation). There are two awarding criteria, each evaluated through points attribution: 90% points given according to the strike price (the lowest bidded price receives the maximum points), and 10% for the degree of citizen participation. The support mechanism will be a two-sided contract for difference, enforced during 20 years.

2.5.2. Turbine Technology

Because of the unique environment, a number of turbine manufacturers are designing wind turbines specifically for offshore use [35]. Offshore turbines are generally larger than their onshore counterparts. There has been a trend towards higher capacity turbines, with higher hub heights and longer, more efficient and durable blades. These turbines, specially designed for the offshore sector, increase energy capture. The larger turbines also provide economies of scale, with a reduction in installation costs and electrical connection, and an amortization of project development and maintenance costs. This trend of increasing rotor diameter can be explained by the fact that a turbine with blades twice as long would, theoretically, be four times as powerful, as it can be deduced from Eq.(2.4). However, the expansion of the area swept by the rotor puts great strain on the entire assembly, and larger designs pose many challenges like taller towers, larger nacelles, and more severe aerodynamic loads. It should be noted that for the same rotor diameter, hub height is lower for

offshore turbines as there are less safety constraints on the distance between blade tip and sea than for onshore, where the blade should rotate high enough above ground. Currently, a big issue concerning offshore turbines is supply chain delays and bottlenecks, due to ever increasing pressure on manufacturers to keep pace with demand [59].

The choice of turbine technology is an important step in the design process, as turbine costs represent approximately 35 to 45% of the overall project costs. Criteria for wind turbine selection are not independant, but often interrelated. For example, more advanced turbine technologies usually require less maintenance costs, but their price is higher as well. Selection criteria include:

- Technical characteristics

  The turbine rated power is an important factor as the total farm capacity usually needs to reach a minimum value associated with the offshore concession. Within a parcel, the number of turbines that can be installed is limited by the parcel boundaries and the minimum distance to ensure between adjacent turbines for safety reasons. Therefore, rotor diameter is also an important factor since the power extracted from the wind is proportional to the square of the rotor radius (see Eq.(2.4)). Hub height is an important criteria as well, as larger rotor diameters require higher towers. If the wind speed regime at the considered site displays reduced wind at lower altitudes, higher towers are necessary to capture the stronger wind speeds above. Moreover, considering the harsh conditions at sea (depicted in Fig. 2.13), features such as anti-corrosion against salt and humidity, lightning protection, typhoon prevention, and resistance to cold temperatures are decisive factors for the turbine choice. Indeed, in cases of failures, maintenance time for offshore turbines is long, and the cost is very expensive. This is also why mature technology including intelligent monitoring and fault diagnosis analysis could be preferred.

- Matching with the wind resource

  The turbine power curve (cut-in, cut-out and rated wind speeds) should correspond with the wind regime at the considered site. Indeed, under the same wind resource conditions, the lower the rated wind speed, the more wind energy absorbed by offshore wind turbines, and the higher the utilization rate of wind resources. Moreover, in case of frequent strong winds, the cut-out wind speed must be high enough to avoid shutting down the turbine too often (protection from mechanical failure). When using time series of wind data (speed, direction, turbulence) measured or modelled for the wind site, the capacity factor (ratio of the actual power

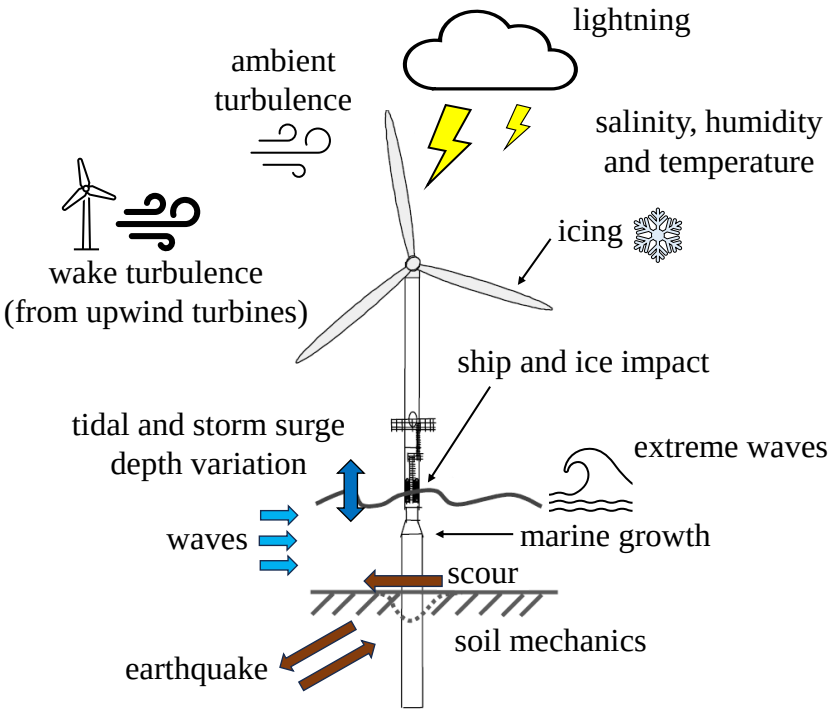

Figure 2.13.: Environmental impacts on an offshore wind turbine.

generation of a wind turbine to the rated theoretical power generation) of the turbine can be deduced. A high capacity factor indicates that the turbine production characteristics fit with the wind resource.

- Economy
  The cost per kW, i.e. per installed power, is an important index to measure the economic performance of wind turbines: it reflects the cost of purchasing wind turbines, which will directly impact the investment cost of wind farm projects. The cost per kWh, i.e. per energy produced, is also essential to evaluate the economic benefits of the whole offshore wind power project. It depends not only on the turbine cost but also on the output energy, and indicates how well the turbine performs with regard to the investment costs. Buying turbines with the cheapest cost per kW does not necessarily leads to low costs per energy if the turbine is not suited for the considered offshore site, thus both factors should be considered.

- Other non-technical criteria
  The reputation and experience of the supplier can also influence the choice

of turbine technology. In Europe, as of 2023, the supply chain for offshore turbines was dominated by two companies: Siemens Gamesa Renewable Energy (66.5% of market shares) and Vestas (26%). Other notable manufacturers include Senvion (formerly called REpower), GE Vernova (formerly General Electric), and Bard, with respectively 4%, 2.5% and 1% of market shares. Moreover, for a considered turbine type, historical performance, production statistics and track record (sales performance) are studied to guarantee reliability. Other aspects such as availability of spare parts, delivery time, and warranty can be considered.

Wind turbine technology has evolved substantially during the past decade, with the development of new designs aimed at improving the system integration of wind power. Indeed, wind power can have a lower (average) market value because turbines tend to produce disproportionately during times when the electricity price is low (and wind speed is high). This has sometimes been referred to as the "self-cannibalization effect", because it is the abundance of renewable energy itself that depresses market prices during periods of high resource availability [60]. Therefore, in a power system supplied fully by wind power, there will be a lack of power at low wind speed and excess at strong wind. To address this issue, low wind speed turbines have entered the market: they are taller and have a larger rotor-to-generator ratio (a lower specific rating per area swept by the rotor). These turbines capture more energy at low wind speeds. For example, the LowWind rotor concept [61] developed by Vestas and the Technical University of Denmark (DTU) is designed to produce more than double the power at low wind speeds compared with a conventional turbine (as illustrated in Fig. 2.14). Initial power system simulations with a LowWind type power curve have shown that this increased power production at low wind where the electricity prices often are high can be quite beneficial [62]. Another feature of the LowWind turbine is that it shuts down at a wind speed around 13 m/s, where conventional turbines have reached their rated power. However, a challenge with low wind speed turbines is the big rotor and blade size, which can increase transportation and installation costs. Moreover, as low wind turbines are optimized to a reduced operational range from e.g. 2 to 13 m/s, it is expected that this will lead to design solutions differing considerably from the conventional variable speed, 3-bladed rotor and pitch regulated turbine.

2.5.3. Turbine Foundations

In offshore wind farms, wind turbines are elevated above the sea level and anchored to the sea bed using foundations. The distance to shore, water depth, and ocean soil conditions will determine the type of foundations to use (floating or fixed-bottom) and the design. The choice of turbine technology is also

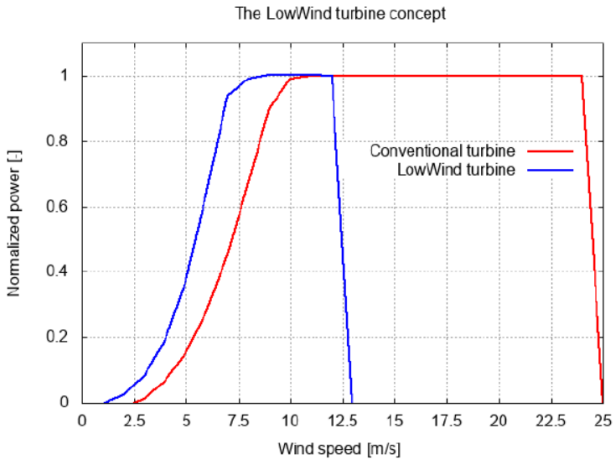

Figure 2.14.: Normalized power curve of the LowWind turbine concept [61].

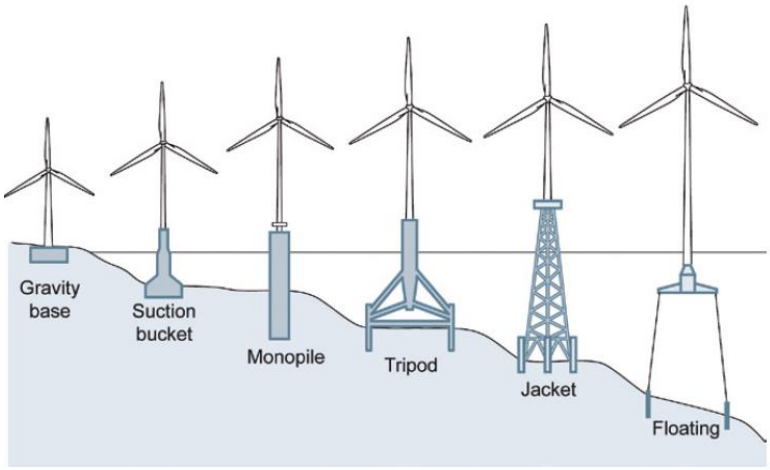

Figure 2.15.: Main types of offshore foundation structures [63].

important as increasing turbine size and head mass have a direct impact on the tower as well as the foundation in terms of mechanical loads. Most offshore wind farms currently consist of fixed-foundation wind turbines in relatively shallow water, usually no deeper than 60 m [64]. There are four main configurations of fixed-bottom offshore foundation structures: monopiles, tripods, gravity base foundations and lattice/jacket structures, shown in Fig. 2.15.

Monopiles consist of a single large-diameter hollow pipe made of steel, buried deep in the seabed, and supporting all the loads (weight, wind, ...) of a large above-surface structure. Monopiles are typically used in shallow water depths

(20 to 40 meters). Nowadays, the monopile structure is considered the dominant concept (cumulative market share of 81.5% in Europe by the end of 2018 [65]). In the offshore wind industry, there is an economic interest to increase the range of applicability for monopiles towards larger turbines and water depths due to the simplicity and relatively low fabrication costs compared to other foundations.

Tripods consist of a large-diameter central, steel tubular section that is supported over its lower length by three braces, which are connected to the seabed using different foundation types (e.g., gravity base, suction bucket or piles). Therefore, the loads applied to the turbine and its support structure are mostly transferred axially (via the braces) to the seabed foundation.

A jacket structure is a lattice frame comprising small-diameter steel struts that are anchored to the seabed. These structures are particularly suited for severe maritime weather conditions because of the additional structural stiffness and larger moment arm for reacting against the bending loads, compared with monopile foundations [66]. Jacket structures are also more adaptable to the conditions encountered on-site, increasing their application range, with geometrical variations of the substructure achieved relatively simply, but without altering the stiffness of the overall structure. There is a shift towards jacket and tripod systems for future offshore wind farms at deeper sea locations that provide consistently higher wind speeds and hence greater wind energy production.

For larger water depths (typically above 50 m), the use of floating structures is necessary. However, floating offshore wind has only recently entered the early commercial stage. Such floating platforms for wind turbines will impose many new design challenges.

In Belgium, 3 structural types of foundations can be found: mostly monopiles, but also jackets and gravity structures, for respectively 86.5%, 7.5% and 6% of installed turbines. Their distance to the coast varies from 23 to 54 km, leading to water depths between 14 and 40 meters [19].

2.5.4. Turbine Layout

Offshore winds are generally characterised by higher annual average speed, more extreme speeds but lower turbulence and gust factors along with a smoother wind shear and more stable directionality. For most sites and with a reasonable turbine spacing, this results in lower aerodynamic loads and offers opportunities for design optimisation [44]. Indeed, wind turbines should be placed so that the local wind resource is maximally exploited while avoiding energy losses from turbine wakes. Finding an optimal layout is critical because even relatively small improvements in energy conversion can translate to significant gains in revenue [67].

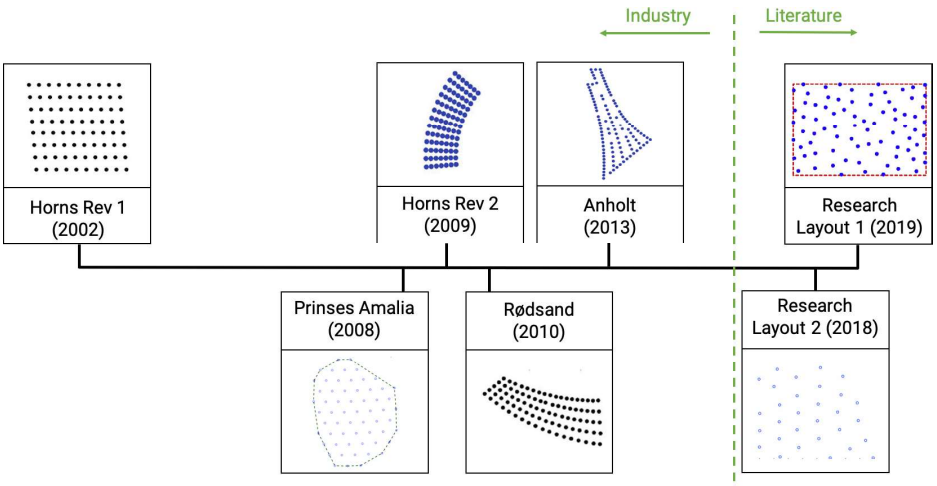

Figure 2.16.: Development of wind farm patterns over time. Left of the dashed green line are wind farm layouts operational in industry, while right of this line are optimised layouts from literature studies [68].

Lower turbulence intensities in offshore conditions require greater spacing between turbines to allow the turbine wakes to be reenergized. Turbine spacing should be adjusted to maximize the amount of energy that can be generated without substantially increasing the investment costs. On the one hand, if the farm is significantly spread out (large spacing between turbines), the inter-array cables length will increase. On the other hand, turbines located too closely will lead to highly detrimental power losses because of wake effects. A compromise is thus required between the objective of maximizing the power generated per turbine and the competing incentive to maximize the number of turbines per unit area. The spacing is therefore an optimization problem between the compactness of the wind farm (which minimizes the investment costs due to subsea cables) and the adequate separations between turbines to minimize the energy loss due to wake effects.

Optimized wind farm designs try to avoid aligning turbines in the directions of dominant wind to minimize wake losses. Wind roses are a useful tool to visualize the wind power potential of an offshore site. They show the frequency of wind speeds blowing from particular directions over a specified period. This allows to determine the dominant wind directions of the site, as well as the directions of higher wind speeds. Earlier offshore wind farms have regular patterns, with turbines often aligned on equidistant rows, but newer and larger wind farms show more variation in patterns, as seen in Fig. 2.16. Optimizing the layout with mathematical tools can lead to highly irregular patterns, which

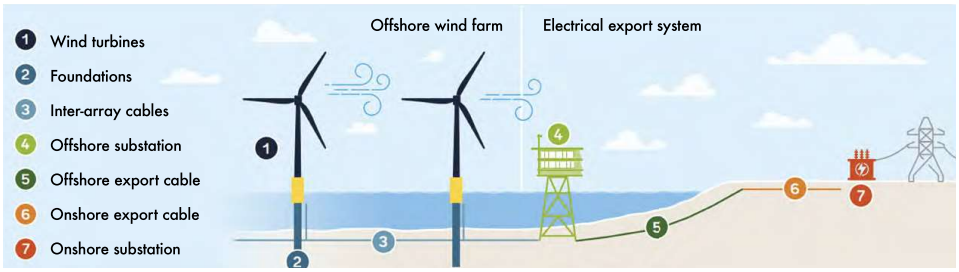

Figure 2.17.: Connection of an offshore wind farm to the onshore grid [15].

have a higher potential of increasing the minimum inter-turbine spacing by strategically relocating a limited number of turbines. Irregular wind farm layouts outperform regular layouts regarding energy production and they also increase the persistence with regard to wind direction [68] (i.e., the power output is less sensitive to fluctuations in wind direction). However, a drawback of irregular layouts is that the turbulence intensity for some turbines may be higher, leading to increased fatigue loads.

2.5.5. Electrical Interconnection

Meticulous design of the electrical infrastructure is also very important. As it is represented in Fig. 2.17, the whole electrical chain includes the inter-array cables within the wind farm, the offshore export cable, the onshore export cable and point of interconnection, and the onshore grid itself. Those four parts are further detailed below.

Within a wind power plant, the collection system comprises the electrical connection of the wind turbine generators to power substations through electrical cables. Those inter-array cables are AC links of lower voltage (the current maximum voltage class available on the market for inter-array cables is 66 kV), usually between 1 and 10 km in length, that carry the energy generated by a single wind turbine (or by a subset of turbines). They enable the energy produced by the turbines to flow to the substations that aggregate their power and export it to the point of connection to the grid [69]. The design of such a cable system is constrained by the limited cable capacity and the avoidance of cable crossings. There are various arrangements for wind farm collector systems employed in existing offshore wind farms, but the four basic designs are [70]:

- Radial: a number of wind turbines are connected to a single cable feeder within a string. The maximum number of wind turbines on each string feeder is determined by the turbines rated power and the maximum capacity of the subsea cable. This design offers the benefits of being

simple to control and also inexpensive because the total cable length is smaller. The major drawback is its poor reliability as cable faults at the end of the radial string have the potential to prevent all downstream turbines from exporting power.

- Single-sided ring: similar to the radial design, but an additional cable runs from the last wind turbine at the end of the string to the collection hub. This design addresses some of the security of supply issues of the radial design by incorporating a redundant path for the power flow within a string, at the expense of additional cables.
- Double-sided ring: the last wind turbine in one string is interconnected to the last wind turbine in the next string. While offering redundancy, it can lead to cables oversizing as the full output power of the wind turbines in one of the strings is diverted through the other string in case of failures.
- Star: individual turbines are connected to a star/cluster point with its own cable. A main cable is then connected to the medium voltage collector hub. This design reduces cable ratings and provides a high level of security for the wind farm as a whole. The main drawback is the more complex switchgear requirement at the wind turbine in the centre of the star.

Offshore wind farms are sometimes dozens of kilometres away from the coast and long-distance power transmission can incur significant energy losses. Without efficient long-distance undersea power transfer, the costs of offshore installations can be prohibitive. For short distances (typically under 70 kilometres [71]), AC connections are suitable, but for longer distances, high-voltage direct-current (HVDC) transmission should be considered. Moreover, careful planning for the installation of power cables is crucial to minimize the lifetime cost of the cables. Indeed, cable laying ships and equipment are very expensive and cables are subject to damage. The greatest hazards are from anchors and fishing, thus the most cost-effective solution to these problems is finding a cable route that avoids fishing and anchoring areas. Inter-array and export cables are buried under the seabed to avoid the risk of entanglement with nets. Another danger are mobile sand waves because they can uncover buried cable in a couple of weeks [35], prompting the need to bury cables 2 to 3 meters deep to avoid wave action. Therefore, a good cable design must balance expensive cable installation and burial costs with the cost of down time and repair.

Another design aspect is finding a suitable site to connect to the transmission grid. Nowadays, almost all offshore wind power plants are connected to onshore grids using point-to-point radial offshore transmission lines [72].

Finding a suitable interconnection point capable of transferring up to several gigawatts of electricity with the existing transmission infrastructure is generally done in coordination with the TSO. However, due to the limited number of points of interconnection in onshore grids close to coastlines, to environmental and community impacts of submarine cables, and to the higher cost to build transmission for a single offshore project, it has become clear that offshore transmission lines that are interconnected, or even meshed, will allow to unlock large amounts of offshore wind energy. Doing so requires proactive and coordinated transmission planning for offshore wind, as well as advancement in offshore transmission technologies. In Belgium, a Modular Offshore Grid (MOG) station centralizes the power of the four most recent offshore wind farms (Rentel, Seastar, Mermaid, and Northwester 2) in an offshore hub, and transports it via three 220 kV AC cables to the onshore substation. This is a cost efficient and reliable way to connect high volumes of offshore wind energy, tackling general increasing cost levels for infrastructure. The combined cable infrastructure guarantees that the wind farms can always transmit the power they generate to the mainland, even if one of the cables is temporarily unavailable. Bundling the cables from several wind farms uses around 40 km less cable than building a separate cable connection for each wind farm, so the MOG project significantly reduces the impact on the seabed and the marine environment [73]. Moreover, the Princess Elizabeth island, planned by Belgium in the North Sea, will be one of the first energy islands. Such hybrid systems allow cost-savings compared to single-purpose solutions because of the need for fewer transmission assets and from optimized operation of the offshore system. Energy islands also have the advantage of remaining readily accessible and expandable, which can lower the risk of future projects.

Finally, in most countries, the onshore transmission grid was built for centralized large generators that were often located away from the coast. With several gigawatts of electricity generated by offshore wind, the existing transmission grid limits may hinder the ability to deliver power to end consumers. In locations with significant offshore wind potential, policymakers are beginning to recognize the need to develop the onshore transmission grid in coordination with offshore planning. For example, in Belgium, to accommodate the future energy production of the second offshore zone planned in the North Sea, a reinforcement of the onshore transmission grid is envisioned, by the addition of two high voltage lines [74] (Boucle du Hainaut and Ventilus projects).

2.6. Operation of an Offshore Wind Farm

Today, offshore wind power is traded on day-ahead markets in many countries [75]. From a wind power point of view, the significant forecast errors associated with the 12–36 h ahead scheduling timeframe would rather suggest trading on a combination between a day-ahead spot and an intra-day adjustment market, if available, allowing the incorporation of more accurate wind power prediction. The current participation of offshore wind farms in electricity markets will constantly be changing, since wind turbines are now able to provide energy and reserve services in the electricity market [76]. There is a growing demand from transmission system operators for wind energy sources to play an active role in balancing the grid through market participation and provision of ancillary services such as frequency control, which have been traditionally provided by conventional power plants [26].

When selling electricity on energy markets, wind farm operators aim at maximizing energy capture. In most commercial wind farms [77], each wind turbine is controlled so that its own power is maximized: this is called the "greedy" strategy. This control allows to optimize the extracted power without exceeding the maximum allowed power and maximum rotor speed (i.e., MPPT mode). Methods for decreasing wake losses have been proposed in the literature: the main ones being wake steering and axial induction control [78]. However, when used in the context of power maximization, these techniques are associated with an increase on loads and fatigue on the turbine blades [79]. The wind industry has recognized the potential of an improved wind farm control but the actual implementation is still difficult because of the inherent system complexities of wind farms and the aerodynamic interactions among wind turbines. In the event of very high winds (or even storms), the turbine must be shutdown so that the generator is not overloaded and dynamic loads do not result in mechanical failure for the turbine. Turbines are then controlled to collectively pitch their blades toward a feather position and shed power [80].

Wind farms require maintenance throughout their typical operational life of 20-25 years [81]. Operation and Maintenance (O&M) costs for offshore wind farms per kW are higher than those for onshore wind, primarily due to the higher cost of accessing the wind site to perform maintenance on turbines and cabling. These costs are heavily influenced by weather conditions and the availability of skilled personnel and specialised vessels. Bad weather and long distances to shore increase maintenance costs and can decrease availability when unexpected repairs are needed. To limit the risk to people in harsh offshore conditions but also to minimize the downtime of the equipment, most of the monitoring is done remotely using sensors and even drones, with diagnostics

performed through embedded sensors in the offshore station and in the wind turbine generators [72]. O&M costs typically constitute 16 to 25% of the LCOE for offshore wind farms with fixed-bottom foundations [42].

2.7. Conclusion

This chapter aimed at providing an overview of offshore wind energy. With declining technology costs, high resource quality, and the increasing scale of turbines and wind farms, offshore wind has become the world's fastest growing renewable generation technology [82]. The LCOE of offshore wind farms is higher than their onshore counterparts because they face more challenging conditions throughout installation, commissioning and O&M due to the harsh marine environments. Their offshore locations thus complicate construction and grid connection, further adding to their planning and project development complexity. However, the stronger wind at sea and the vast potential over open water make offshore wind farms highly profitable. Exploiting offshore wind resources is particularly suitable for countries with a high population density and difficulties to find suitable sites on land, but with an ample and windy coastal maritime space. The complex aerodynamic phenomena arising in offshore wind farms have also been explored. Wake effects, which lead to significant power losses, are exacerbated in offshore conditions because of the lower ambient turbulence. The different aspects involved in the design of offshore wind farms have also been investigated. Many design considerations are interdependent, prompting the need for an integrated design approach.

Considering the massive growth of offshore wind generation in electrical grids, the techno-economic analysis of modern power systems can no longer be envisioned without an accurate modelling of this fluctuating generation within power system computations. In the next chapter, we will thus focus on the modelling of the power output of offshore wind farms, taking into account aerodynamic effects while maintaining a low computational cost.

CHAPTER 3.

Topology-Aware Offshore Wind Farm Surrogate

As the role of offshore wind generation increases in modern power systems, the need for enhanced modelling techniques becomes critical. In problems involving iterative computations, simplified offshore wind farm models often disregard complex aerodynamic effects due to computational issues associated with accurately representing them. For example, the *power curve approach* simply converts free-flow wind speed to power output by using the turbine power curve, then multiplies it by the number of turbines in the farm to assess the total generated power. Wake effects are ignored with that approach, but they have a significant impact on the produced electricity. Wind farm numerical simulations cannot be directly integrated in complex iterative power systems simulations. However, a database can be generated from wind farm simulations, then be used to train fast models based on Machine Learning (ML) techniques. Machine learning focuses on extracting knowledge from data: it is a research field at the intersection of statistics, artificial intelligence, and computer science. The application of machine learning methods has in recent years become ubiquitous in everyday life [83].

This chapter is organized as follows. A bibliographical review for wind farm models using Machine Learning is provided in section 3.1. It highlights the limitations of the current literature, and the subsequent innovations developed in this chapter. Then, section 3.2 details how wind farm simulations can be carried out to build a significant training database. High-fidelity simulations as well as engineering models are considered and described. They are then compared in section 3.3 in terms of computation time, accuracy and practicality. Section 3.4 details the wind farm simulations carried out to build the training database. In section 3.5, a wind farm surrogate using Machine Learning techniques is developed using this training database. Geometric and physics-informed features are added the inputs of the model in order to enable it to be topology-

aware, i.e., applicable to any wind farm configuration. Different algorithms of supervised Machine Learning are considered: they are described, tuned, then compared based on model complexity, inference time, and accuracy. Section 3.6 validates the topology-aware ML surrogate using high-fidelity computations of a real-life wind farm generally used as a benchmark in the literature. Finally, section 3.7 concludes this chapter.

3.1. Literature Review on Modelling Wind Farms Using Machine Learning

Previous research has explored the use of ML for modelling offshore wind generation, focusing on diverse applications such as annual energy production estimates, optimization of wind farm layouts, and real-time monitoring. In references [84]–[86], power measurements of wind turbines and/or wind information from meteorological masts are gathered at onshore wind farms to train a ML model dedicated to predict the power produced by each turbine. Neural networks are used in [84] to estimate wind turbine power generation, while [85] trains adaptive neuro-fuzzy interference system, cluster center fuzzy logic, k-nearest neighbor and neural networks. Authors in [86] compare physics-based, data-driven and hybrid models, using onshore Supervisory Control And Data Acquisition (SCADA) data. A strong limitation of those models is their reliance on measurements, which are often not publicly accessible or even entirely unavailable for future farms that are yet to be built. Authors in [87] train ML surrogates on wind farm simulations, but every wind farm needs its own surrogate, making the training process cumbersome.

All works cited above are building a model *only applicable for the wind farm on which they have been trained*, i.e., for a fixed layout and wind turbine characteristics. This means that the model has to be completely retrained for any modification of the wind farm configuration, i.e., adding/removing turbines or changing the turbine type for, e.g., re-powering. Consequently, the current ML models cannot be applied to various wind farms, such that a different model has to be trained for each wind farm topology. Given the diversity in layout shape, turbine spacing, turbine characteristics, ... of the future offshore wind landscape, current methods are not computationally efficient. Moreover, the topology of future wind farms, which are not yet built, remains unknown and this uncertainty must be taken into account when studying them, which can be achieved by considering different possible configurations (leading to different power outputs) of those farms. Finally, none of the cited works allows the possibility to consider turbine failures. Indeed, in case of maintenance or repair, an idle turbine does not produce electricity, thus does not extract energy

from the wind. Its situation affects all downwind turbines, and the wind energy is redistributed among neighbouring turbines in a complex way. This impacts the wind farm resulting production, especially with turbines that have a large rotor diameter.

A few papers have focused on creating generalized ML models, to ensure that the training process should be carried out only once. In [88], two neural networks (respectively capturing wake and turbulence field) are trained with a database consisting of simulations performed on a standalone wind turbine. While showing strong capabilities to capture the complex spatial relationship between inflow conditions and the wake fields, the developed model exhibits a high computation time for large wind farms. Indeed, power computations for a wind farm require the propagation of the wake field, which involves the neural network to be run many consecutive times. In [89], a dataset is built upon medium-fidelity aerodynamic simulations and the ML model uses atmospheric and physics-informed features to generalize to different layout configurations. However, the proposed model is limited to very specific wind conditions. Authors in [90] train physics-induced graph neural networks, able to generalize to unseen wind farm configurations. However, the use of graph neural networks involves a high computation time that increases with the number of turbines. In this way, the reported time is 0.1 s for a 40-turbines wind farm, which exceeds wind farm simulation tools based on advanced wake models, making them irrelevant for iterative computations. Besides, the proposed model in [90] cannot handle heterogeneous turbine types.

Therefore, the objective of this chapter is to develop an offshore wind farm surrogate built on wind farm simulations (removing the need for measurements), encompassing heterogeneous turbine types and turbine failures, and more importantly able to generalize to unseen wind farm configurations (i.e. applicable to any offshore wind farm in the world, with the training process carried out only once), while exhibiting a very low computation time when making power assessments.

3.2. Offshore Wind Farm Simulations

There are several methods to run wind farm simulations. The simplest and less expensive approach is to use analytical wake engineering models. In a general form, wake models apply aerodynamic simulations considering mass and momentum conservation principles. However, the equations governing the models rely on many assumptions on aerodynamics, model parameters often need to be tuned (either with SCADA data relying on measurements

Table 3.1.: Comparative table between physics-based wake models (engineering models), and CFD simulations.

	Wake models	**CFD**
Based on	Simplified equations of conservation and momentum, and physical assumptions	Navier-Stokes equations (conservation of mass, momentum and energy)
Computation	Analytical, steady-state	Numerical, dynamics
Accuracy	Limited	Medium to high
Computation time	Low	Hours to days
Computation cost	Low	Very expensive
Usage	Simple (few inputs)	Know-how required
Database creation	Fast and easy	Cumbersome
Examples	Jensen, Gaussian, Curl, Ainslie, ...	RANS, LES, DNS, ...

or with more advanced techniques), and power predictions deep inside wind farms can have bias. Nonetheless, their speed and simplicity make them attractive to use in the context of this work. Computational Fluid Dynamics (CFD) rely on a set of partial differential equations to solve with initial and boundary conditions, a discrete representation of the geometry and flow domain (the mesh) and on a numerical procedure (spatial and temporal discretization schemes). In order to choose between the two approaches for running wind farm simulations (CFD or wake models), an existing wind farm will be modelled with the two methods. These simulations first need to be validated against hourly steady-state measurements. The difference should be assessed, as well as their advantages and disadvantages (presented in Fig. 3.1) in order to choose the method that will be used for the remaining of this work. Once validated, they should then be used to create the database for the training of the ML model.

3.2.1. Reynolds Averaged Navier Stokes Simulations

The fundamental basis of almost all CFD problems is the Navier–Stokes equations, which are partial differential equations describing the motion of viscous fluid flows. For air flows around a wind turbine, compressibility effects may only affect at blade tips. We can thus use the incompressible Navier-Stokes equations. The conservation of mass principle leads to the continuity equation,

which applied to incompressible flows is expressed as:

$$\frac{\partial u_i}{\partial x_i} = 0 \tag{3.1}$$

where u_i is the flow velocity in direction i.

The momentum equations are derived from the conservation of momentum (Newton's second law):

$$\frac{\partial u_i}{\partial t} + \frac{\partial}{\partial x_j}(u_i u_j) = -\frac{1}{\rho}\frac{\partial p}{\partial x_i} + \nu \frac{\partial}{\partial x_j}\frac{\partial u_i}{\partial x_j} \tag{3.2}$$

where t is time, i, j=1, 2, 3 are the index of flow direction, ρ is the mass density, p is the pressure, and ν is the kinematic viscosity.

For incompressible flows, the energy is no longer coupled to continuity and momentum, so it can be solved independently. Initial conditions must be specified, as well as boundary conditions at the inlet (prescribed density, energy and velocity), outlet (prescribed velocity or vanishing stress), and at solid walls (e.g., no-slip condition, and given temperature or prescribed heat flux). Solving these equations requires a discretization of space (using finite difference, finite volumes, finite elements, ...) and advancement in time is typically expressed by some kind of finite difference method (implicit or explicit). The discretized conservation equations are solved iteratively: a number of iterations are usually required to reach a converged solution. Convergence is obtained when changes in solution variables from one iteration to the next are negligible and overall property conservation is achieved.

Turbulence is the time-dependent chaotic behaviour seen in many fluid flows. The numerical solution of the Navier–Stokes equations for turbulent flow is extremely difficult, due to the significantly different mixing-length scales that are involved in turbulent flow. The stable solution of this requires such a fine mesh resolution that the computational time becomes significantly infeasible for calculation or Direct Numerical Simulation (DNS). Indeed, to numerically simulate turbulent flows with accuracy, the motion needs to be calculated for all eddies (movements of fluid that deviate from the general flow of the fluid) in time and space, i.e., no turbulence model is used. DNS cannot be used for most engineering flows: it is mainly applied in academic research to obtain the exact solution of basic turbulent flows. Therefore, to reduce computational costs, turbulence models have been introduced. For turbulent flow simulations of offshore wind farms, there are several computational strategies with respect to computed turbulent scales.

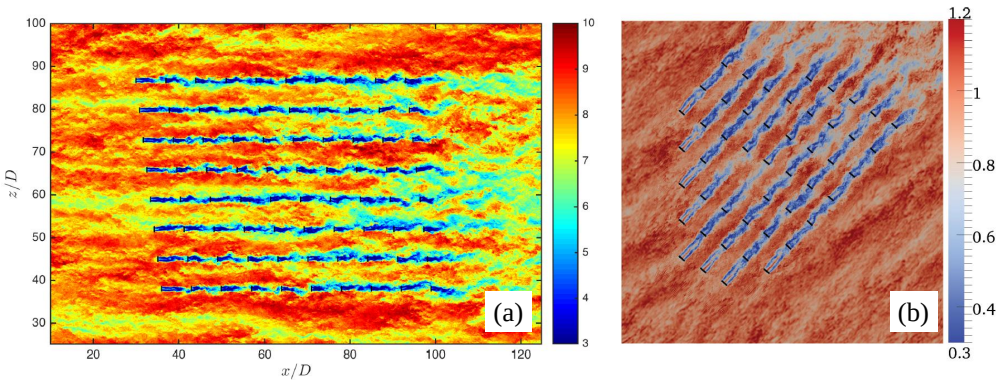

Figure 3.1.: Instantaneous streamwise velocity of two offshore wind farms obtained with LES simulations. The black bars indicate the turbine rotors.(a) Source: [93], (b) Source: [94] (velocity normalized by hub height wind speed).

In Large Eddy Simulations (LES), all flow structures larger than a cut-off length defined by the user (i.e., large eddies) are resolved without modelling, while all flow structures smaller than the cut-off length (i.e. subgrid-scale eddies) are modelled. If the cut-off length is smaller than the smallest eddies, then LES becomes DNS. This approach is computationally very expensive in time and in computer memory, but produces accurate results because it explicitly resolves the larger turbulent scales. For example, in [91], [92], LES are able to capture transitory effects in offshore wind farms and large turbulent scales are resolved. In [93], an offshore wind farm of 80 turbines was modelled using LES (depicted in Fig. 3.1(a)): one complete simulation required 1536 processors during about 55 hours for simulating 67 minutes of wind, which means roughly 85 000 hours-processors. Another offshore wind farm of 48 turbines was simulated in [94] (shown in Fig. 3.1(b)): it required more than a million CPU-hours for 10 minutes of simulation. Because of the prohibitively high computational costs, LES are mainly used for academic research, and a deep know-how is required to run such simulations with relevant results.

In many engineering problems, we are often interested in the mean (or time-averaged) flow characteristics, rather than instantaneous ones. Mean flows contain a lot of important information, such as mean velocity profiles, mean pressure profiles and forces. Mean flows can be obtained by averaging instantaneous flows (from high-fidelity simulations), but it is also possible to average the Navier-Stokes equations before solving them, which yields the *Reynolds-Averaged Navier Stokes (RANS) equations*. A RANS solver models the averaged turbulent quantities so that only mean flow and statistical moments

are obtained, in a steady-state simulation. For assessing the reliability of power systems, e.g., in the context of adequacy studies, the mean power is needed on an hourly basis. The small fluctuations around the mean value are not necessary (which would not be the case if the power was needed, e.g., to assess the ability of wind turbines to participate to very fast frequency balancing). The principle of RANS equations is that any variable can be decomposed into a mean and a fluctuation:

$$u(x_i, t) = \overline{u}(x_i, t) + u'(x_i, t) \tag{3.3}$$

where $\overline{u}$ is the mean, and u' is the fluctuation. We also have $\overline{u'} = 0$. This Reynolds decomposition is injected into the Navier Stokes equations. Equations for the mean quantity are then obtained by applying the averaging operator. Moreover, subtracting instantaneous and mean equations leads to equations for fluctuations. The RANS equations for incompressible flows are then deduced from Eq.(3.1):

$$\frac{\partial \overline{u_i}}{\partial x_i} = 0 \tag{3.4}$$

and Eq.(3.2):

$$\frac{\partial \overline{u_i}}{\partial t} + \frac{\partial}{\partial x_j}(\overline{u_i u_j}) = -\frac{1}{\rho}\frac{\partial \overline{p}}{\partial x_i} + \frac{\partial}{\partial x_j}\left[\nu \frac{\partial \overline{u_i}}{\partial x_j} - \overline{u_i' u_j'}\right] \tag{3.5}$$

The term $\overline{u_i' u_j'}$ in Eq.(3.5) is the tensor of Reynolds stresses. They can be viewed as an apparent stress acting on the mean flow field due to turbulence [95]. They represent the correlations between velocity components and the transport of momentum by the turbulence. The system of RANS equations (3.4) and (3.5) is open: there are more unknown than equations. In particular, the six independant components of the symmetric Reynolds tensor are not known. Therefore, modelling is necessary to close the system: we solve the statistical/mean equations, and we model all fluctuations (motion of eddies). The Reynolds stresses thus need to be expressed. The closure strategy can be of different orders, but in practice, only first-order and second-order closure models are used. For second-order closure models (or Reynolds stress transport models), each of the six Reynolds stress components are modelled individually, thus a transport equation must be derived and solved for each component. However, it is often difficult to obtain a fully converged solution with this approach, and it requires relatively high computational costs. In first-order closure models, the six stress components are modelled all together, assuming a similarity between the viscous stress (due to viscosity) and Reynolds stress (due

to turbulence). This is based on the Boussinesq hypothesis, which introduces the concept of eddy viscosity or turbulence viscosity [96], a function of space and time (and not a fluid property). It is assumed that the Reynolds stresses are proportional to the mean velocity gradient and the eddy viscosity:

$$R_{ij} = -\rho\overline{u_i' u_j'} = \mu_T \left(\frac{\partial \overline{u}_i}{\partial x_j} + \frac{\partial \overline{u}_j}{\partial x_i} \right) - \frac{2}{3}\delta_{ij} k \tag{3.6}$$

where μ_T is the eddy viscosity, δ_{ij} is the Kronecker delta:

$$\delta_{ij} = \begin{cases} 0, & \text{if } i \neq j \\ 1, & \text{if } i = j \end{cases} \tag{3.7}$$

and k is the turbulent kinetic energy:

$$k = \frac{1}{2}\overline{u_i' u_j'} \tag{3.8}$$

The Boussinesq hypothesis reduces the number of unknowns from the six components of the symmetric Reynolds stresses tensor to two: μ_T and k. It should be noted that the Boussinesq hypothesis is only valid for isotropic turbulence. To finally close the RANS equations, models providing μ_T and k need to be established. These can be based on a simple algebraic model (zero-equation model), on a single transport equation (e.g. Spalart–Allmaras model [97]), or on two transport equations (e.g., k-ω [98], k-ϵ [99] and shear-stress transport [100] models).

The different strategies for computing turbulent flows are illustrated in Fig. 3.2. Unsteady RANS (or URANS) simulations allow to capture unsteady flow motions that are not due to turbulence (since the effects of turbulence are already modelled as the Reynolds stress). It is used to study large-scale unsteady flow motions, when there is a very clear time-scale separation between those motions and turbulence. To build a relevant database for the training of the ML surrogates, thousands of simulations need to be run, for different sets of input parameters. In practice, it is not tractable to run such a number of simulations with very advanced CFD models such as LES, as it would take too long to build the database. This is why Reynolds-Averaged Navier–Stokes are used in this work to build a database linking free-flow wind information with power output. Even though the accuracy of RANS is lower than for more advanced CFD solvers (that remain too expensive in time and resources when they are used on large offshore wind farms), it can be more accurate than analytical wake models, especially for deep wind farms. Moreover, it is tractable to run hundreds of RANS simulations for small farms in a reasonable

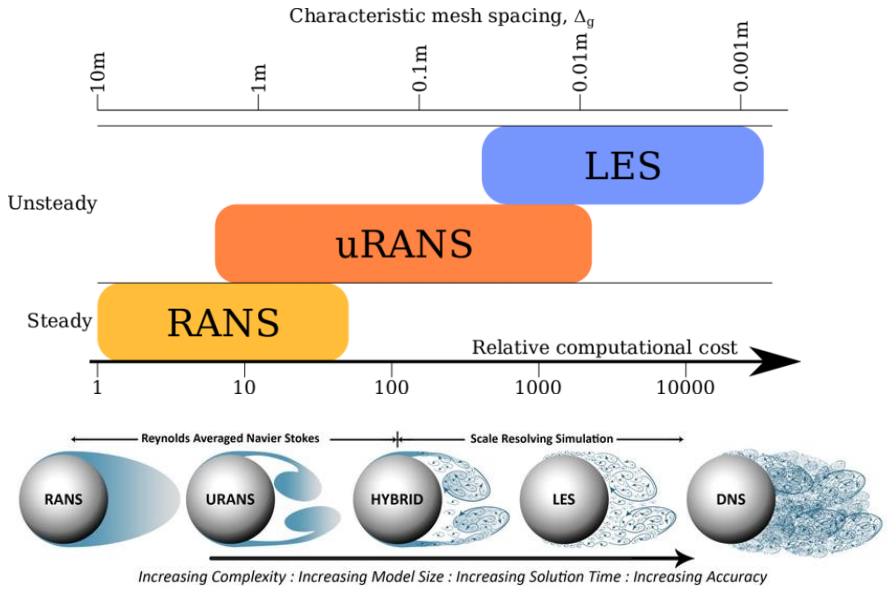

Figure 3.2.: Summary of CFD modelling of turbulent flows [101].

time, if parallel computing is used. It should be noted that properly running RANS simulations still requires specific know-how.

Wind Turbine Representation

In RANS simulations, the wind turbine geometry is not physically modelled; instead, the rotor forces are represented by actuator lines or an Actuator Disk (AD), shown in Fig. 3.3. For the latter, the wind turbine is then seen as an ideal fluid dynamic element that extracts momentum and energy from the wind, uniformly over the rotor area and without any specific load aerodynamic information on the blades. An actuator disk allows air flow to pass through its surface, withstands pressure differences between upstream and downstream disk surfaces, and acts as a momentum source term in the Navier–Stokes equations. Authors in [102] showed that as long as the actuator disk is subject to ambient atmospheric turbulence, the averaged velocity deficit calculated by the disk is similar to that from a CFD simulation in which the full rotor geometry is represented. The thrust, i.e., the force exercised by an actuator disk on the external flow, determines the amount of momentum that is extracted from the wind and is therefore very important in wind turbine wake simulations that are modelled with actuator disks.

The determination of the actuator disk forces in multiple wake configurations is not straightforward. In cases where downstream actuator disks experience

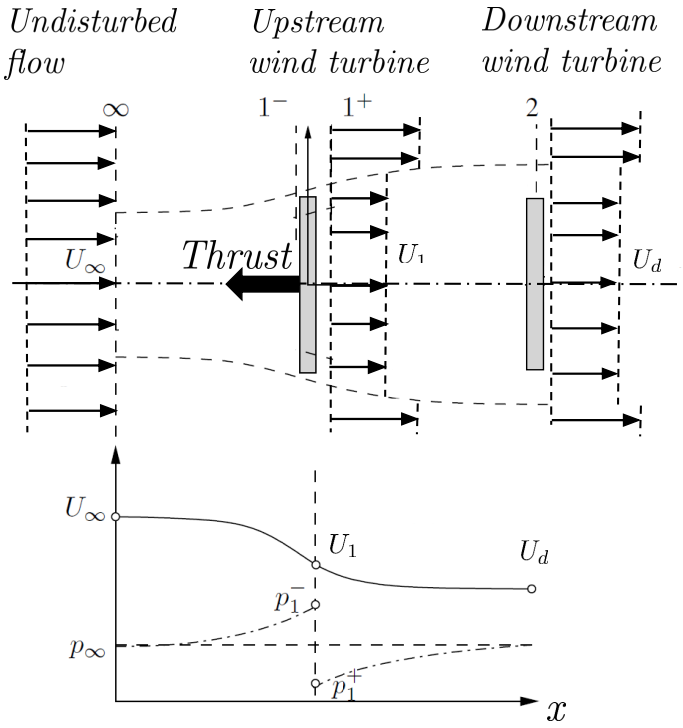

Figure 3.3.: Actuator disk concept and downstream wind turbine. U is the streamwise velocity and p is the pressure.

the velocity deficit of upstream disks, the downstream disks that are positioned in the full wake of others should experience lower normal and tangential forces compared to those that are subject to the undisturbed flow, as shown in Fig. 3.3. Therefore, they will produce less power than the upstream actuator disks. Moreover, determining the power output of waked wind turbines is not trivial, as the power extracted by an actuator disk from the wind can be written as:

$$P_{wind\,turbine} = 0.5 * \rho_{air} * \pi * R^2 * C_p(u_\infty) * U_\infty^3 \tag{3.9}$$

where R is the radius of the wind turbine rotor (and thus the radius of the actuator disk), C_p is the power coefficient and u_∞ is the upstream undisturbed flow velocity at hub height. Eq.(3.9) assumes that the wind turbine is actively controlled in order to optimize the extracted power without exceeding the maximum allowed power and maximum rotor speed, and that the nacelle is aligned with the main wind direction. However, for a waked wind turbine, the reference velocity u_∞ is not readily known and would require arbitrary decisions

about which upstream distance to use when specifying the velocity. Instead, for wind farms, it is useful to base the relations for power on the prevailing axial velocity at the rotor disk position, u_d, such that:

$$P_{wind\,turbine} = 0.5 * \rho_{air} * \pi * R^2 * C_p^*(u_d) * u_d^3 \tag{3.10}$$

The relationship between C_p and u_∞ for most manufactured wind turbines is readily available in the form of power curves or C_p curves. However, the calibrated coefficient C_p^* as a function of the averaged actuator disk velocity u_d is not directly provided. Therefore, a calibration procedure is carried out in order to determine the value of C_p^* with regard to u_d: single standalone wind turbine simulations are run for $2 \leq u_\infty \leq 30\ m/s$ with equidistant intervals of 0.5 m/s. From these simulations, it is possible to extract the corresponding u_d and its associated C_p^* [103].

Modelled Wind Farm

The modelled offshore wind farm is Alpha Ventus, Germany's first offshore wind farm located in the North Sea and built in 2009. Electricity has been produced by the wind farm since 2010. It consists of 12 wind turbines equally spaced: 6 Adwen AD5-116 of 5 MW on tripod foundations with a rotor diameter of 116 meters, and 6 Senvion 5M of 5 MW on jacket foundations with a diameter of 126 meters. The layout can be seen in Fig. 3.4. Because it was the first offshore wind farm in Germany, Alpha Ventus is accompanied by several research projects sponsored by the German Federal Ministry for Environment. Measurements have been extensively collected in the scope of the "Research at Alpha Ventus" project (RAVE) [104] since 2009 by a multitude of sensors installed on 4 of the 12 turbines in the wind farm. The 100-m-high measuring mast Fino 1 is located directly alongside the wind farm, allowing to record meteorological data. In addition, SCADA data and measurements at both substations (onshore and offshore) have been collected. Times series from 2011 to 2014 of wind speeds and wind directions from Fino 1 as well as SCADA measurements of electrical power output for all turbines are available.

Numerical Setup

In CFD simulations, the mesh should be carefully chosen, as a mesh too coarse leads to approximate results and a mesh too refined is computationally too heavy. In this work, the computed domain dimensions are 5500m x 5000 m x 500m, divided into 182 x 167 x 17 cells respectively in the x, y and z direction. This means that the meshing is roughly equivalent to 4 points per wind turbine diameter. In order to capture the most relevant phenomena around the wind

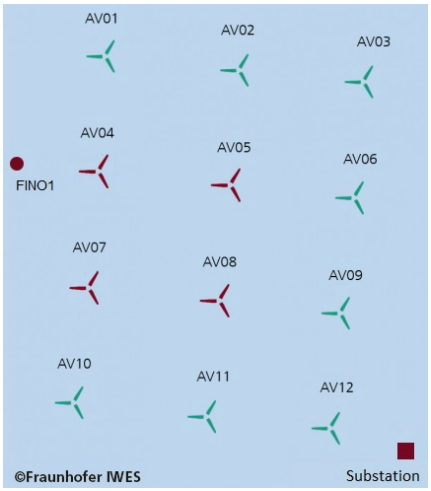

Figure 3.4.: Layout of the offshore wind farm Alpha Ventus. Red turbines are those equipped with extensive measurement technology [104].

turbines rotors, the mesh is refined in the actuator disks areas: the mesh is then equivalent to 16 points per diameter. This refinement is kept for 10 diameters behind each wind turbine so that wake effects are correctly captured.

The RANS equations are closed with the k-ϵ two-equations model for the turbulent viscosity. It is one of the simplest "complete" method because it does not require any flow-dependent parameter to be specified: it is extensively used in the literature, with known performance [103], [105]. The model constants have been carefully calibrated for several different types of basic flows so that the model can (in theory) be applied to a wide variety of flows. One of the limitations is that the model needs a special treatment in the near-wall region. The two transport equations are solved for the turbulent kinetic energy k (Eq.(3.11)) and the turbulent dissipation rate ϵ (Eq.(3.12)).

$$\rho * \left(\frac{\partial k}{\partial t} + \overline{u_j} \frac{\partial k}{\partial x_j} \right) = \frac{\partial}{\partial x_j} \left(\frac{\mu_T}{\sigma_k} \frac{\partial k}{\partial x_j} \right) + \mu_T \frac{\partial \overline{u_i}}{\partial x_j} \left(\frac{\partial \overline{u_i}}{\partial x_j} + \frac{\partial \overline{u_j}}{\partial x_i} \right) - \rho * \epsilon \quad (3.11)$$

$$\rho * \left(\frac{\partial \epsilon}{\partial t} + \overline{u_j} \frac{\partial \epsilon}{\partial x_j} \right) = \frac{\partial}{\partial x_j} \left(\frac{\mu_T}{\sigma_\epsilon} \frac{\partial \epsilon}{\partial x_j} \right) + C_{1\epsilon} * \mu_T \frac{\epsilon}{k} \frac{\partial \overline{u_i}}{\partial x_j} \left(\frac{\partial \overline{u_i}}{\partial x_j} + \frac{\partial \overline{u_j}}{\partial x_i} \right) - \rho * C_{2\epsilon} * \frac{\epsilon^2}{k} \quad (3.12)$$

where $C_{1\epsilon}$ and $C_{2\epsilon}$ are model constants respectively set to 1.44 and 1.92 [106], and σ_k and σ_ϵ, respectively set to 1 and 1.3, are effective Prantdl numbers

relating eddy diffusion of k and ϵ to the momentum equation eddy viscosity. Eddy viscosity μ_T is computed as:

$$\mu_T = \rho * C_\mu * \frac{k^2}{\epsilon} \tag{3.13}$$

where C_μ is another model constant model set to 0.09.

Boundary conditions at the inlet are a Neumann condition (zero gradient) for pressure, and a Dirichlet condition (constant value) for k and ϵ. For wind speed, a generalised log-law type ground-normal inlet boundary condition for the streamwise component of wind velocity is used, leading to a neutral atmospheric boundary layer modelling. At the outlet, pressure is set to 0 while k and ϵ have a zero gradient condition. For wind speed, an inlet/outlet boundary is used, i.e., reverse flow is set to a fixed value while outflow is treated using a zero gradient condition. Lateral and top boundaries have a symmetry condition.

Initial and inlet values for the turbulence characteristics k and ϵ are computed as follows [107]:

$$k = \frac{(u^*)^2}{\sqrt{C_{mu}}} \tag{3.14}$$

$$\epsilon = \frac{(u^*)^3}{\kappa * (z + z_0)} \tag{3.15}$$

where u^* is the friction velocity given by:

$$u^* = \frac{u_{ref} * \kappa}{ln(\frac{z_{ref}+z_0}{z_0})} \tag{3.16}$$

with κ the Von Karman constant (0.41), z_0 the surface roughness (0.0002 in offshore conditions), and u_{ref} the wind speed at the reference height z_{ref}.

The solver employs the SIMPLE (Semi-Implicit Method for Pressure Linked Equation) [108] algorithm to solve the continuity and momentum equations. It is an iterative procedure for the calculation of pressure and velocity fields. Starting from an initial pressure field p^0, its mains steps are to solve the discretized momentum equations to yield intermediate velocity fields, solve the continuity equation for pressure correction, correct pressure and velocity, solve all other discretized transport equations, then repeat until all fields have converged.

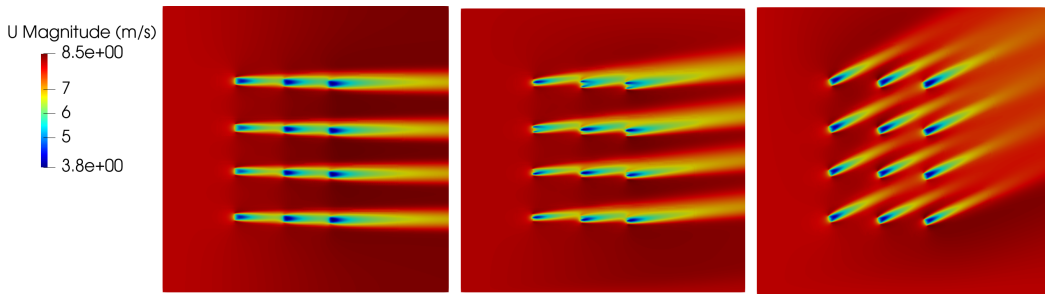

(a) (b) (c)

Figure 3.5.: RANS simulations of the Alpha Ventus wind farm, for a wind speed of 8 m/s and a wind direction of (a) 270°, (b) 265° and (c) 245°.

The RANS simulations are carried out using OpenFOAM, a free open source CFD software [109], for wind speeds ranging between 2 m/s and 32 m/s with intervals of 1 m/s, and for wind directions ranging from 0° to 360 ° by steps of 5°. This amounts to a total of 2232 simulations, where each simulation computes the mean hourly power for a given combination of hourly wind speed and direction. This allows to get the power output of each wind turbine for many combinations of wind speed and wind direction. Each simulation is run in parallel on 25 CPUs for approximately 4 minutes, which amounts to 1.67 CPU hour. Simulations for a wind speed of 8 m/s and wind directions of 0°, 5° and 25° can be seen in Fig. 3.5. Comparatively with more advanced CFD models, a simulation of one single wind turbine using LES needs a computation time of 8000 CPU hours [110].

It is assumed that the wind turbines are actively controlled in order to optimize the extracted power without exceeding the maximum allowed power and maximum rotor speed (i.e., maximum power point tracking mode) and that the nacelle is always perfectly aligned with the main wind direction. This is usually called the "greedy" strategy, where each wind turbine is controlled so that its own power is maximized, and it is used in practice in most commercial wind farms [77].

3.2.2. Engineering Wake Models

Despite having a lesser accuracy than CFD simulations, wake models receive a lot of attention due to their efficiency and fast computation time. These semi-empirical models provide descriptions of the energy loss in the wake of individual turbines. They are based on simplified assumptions about turbine wakes (based on observations) and on conservation of momentum. They may

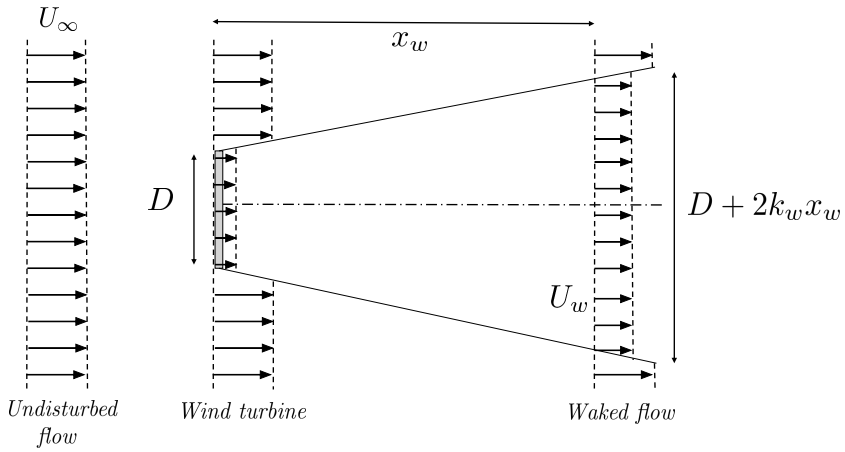

Figure 3.6.: The Jensen wake model concept.

include empirical constants derived from either wind tunnel model data or from field tests of wind turbines. They are useful for describing the important aspects of the energy loss in turbine wakes, and, therefore, for modelling wind farm array losses.

The first wake models were very quick to estimate the waked wind speed between two interacting wind turbines, but their accuracy were limited. For example, the Jensen model [111], developed in 1983, assumes a top-hat shape for the normalized velocity deficit (pictured in Fig. 3.6) and was derived using only mass conservation. The velocity deficit Δu in the wake of a turbine is computed as follows:

$$\frac{\Delta u}{u_\infty} = \frac{u_\infty - u_w}{u_\infty} = \frac{(1 - \sqrt{1 - C_T})}{(1 + \frac{2 * k_w * x_w}{D})^2} \tag{3.17}$$

where u_∞ is the free-flow undisturbed wind speed, Δu is the velocity deficit, u_w is the waked wind speed behind the turbine, C_T the thrust coefficient of the turbine, k_w the Jensen wake spreading parameter, D the wind turbine diameter and x_w the distance downstream behind the turbine. The Frandsen model [112] is another formulation that assumes a top-hat shape for the velocity deficit and apply the conservation of mass and momentum to a control volume around the turbine. Although they are commonly used in the literature and commercial softwares because of their speed, the Jensen and Frandsen models tend to overestimate power prediction in full-wake conditions and underestimate it in partial-wake conditions due to the top-hat velocity deficit assumption.

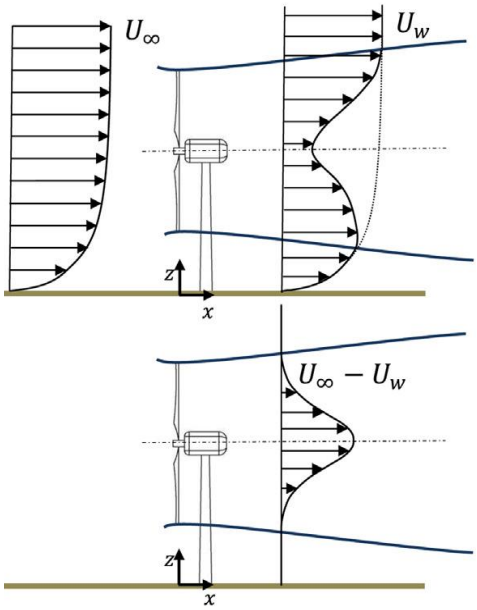

Figure 3.7.: Schematic of the vertical profiles of the mean velocity (top) and velocity deficit (bottom) downwind of a wind turbine obtained by assuming Gaussian distribution for the velocity deficit in the wake [113].

Subsequent studies found that the velocity deficit in wakes is much closer to a bell-shaped distribution rather than linear (see Fig. 3.7), and a series of new wake models have been proposed accordingly [113]–[118]. These past few years, more advanced wake models have been developed and their accuracy keeps increasing. For example, in [119], an adaptive data-driven analytical model is proposed, which significantly improves the accuracy of the initial wake model. It is thus interesting to consider these improving analytical models in the context of this work (hourly steady-state simulations).

Among recent wake models, the Gaussian wake model, using a gaussian function to simulate the velocity distribution in the wake, was proposed. It has been proven to be in good agreement with both numerical and experimental results. Indeed, the Gaussian shape of the hub height velocity deficit in the far wake can clearly be seen in wind tunnel measurements [120], [121], numerical simulations [122], and data of operating wind farms [123]. The Gaussian model uses an analytical solution of the simplified linearized Navier-Stokes equations, which are appropriate for normal turbine operation [124]. It is derived from the mass and momentum conservation equations (if viscous and pressure terms are neglected). If the velocity deficit in the turbine wake is assumed to have

a Gaussian shape, regardless of incoming conditions, the self-similarity in the wake describes the normalised velocity deficit as:

$$\frac{\Delta u}{u_\infty} = C(x_w)e^{-\frac{r^2}{2\sigma_g^2}} \tag{3.18}$$

where $C(x_w)$ represents the maximum normalized velocity deficit at each downwind location which occurs at the centre of the wake, r is the radial distance from the turbine centre, and σ_g is the standard deviation of the Gaussian-like velocity deficit profiles at each downstream distance x_w. Inserting Eq.(3.18) into the momentum equation, the expression for $C(x)$ becomes (the interested reader can find more details of the mathematical development in [113]):

$$C(x) = 1 - \sqrt{1 - \frac{C_T}{8(\frac{\sigma_g}{D})^2}} \tag{3.19}$$

If we assume a linear expansion for the wake region, $\frac{\sigma_g}{D}$ can be written as:

$$\frac{\sigma_g}{D} = k^* \frac{x_w}{D} + \epsilon \tag{3.20}$$

where k^* $(\frac{\partial \sigma_g}{\partial x_w})$ is the growth rate and ϵ is equivalent to the value of $\frac{\sigma_g}{D}$ when x_w approaches 0. In practice, it is set to:

$$\epsilon = 0.25 * \frac{1 + \sqrt{1 - C_T}}{2\sqrt{1 - C_T}} \tag{3.21}$$

Subsequent work [115] posed the growth rate k^* as an empirical formulation depending on the local turbulence intensity TI:

$$k^* = k_a * TI + k_b \tag{3.22}$$

where k_a and k_b are parameters tuned empirically.

The wake model is complemented with a turbulence model to capture the turbulence field, which is essential in the context of interactions among multiple turbines. Indeed, there is a turbulence intensity enhancement in turbine wakes, also called added turbulence as opposed to the ambient turbulence carried by the undisturbed flow. Since turbulence facilitates wind speed recovery in the wake, disregarding this effect may lead to a significant underestimation of the actual generated power. The Crespo-Hernandez approach [125] has been widely used for modelling the added turbulence TI^+ due to turbine operation.

It follows the empirical equation:

$$TI^{+} = C_c * a^{C_a} * TI^{C_i} * \left(\frac{x_w}{D}\right)^{C_d} \tag{3.23}$$

where C are model parameters: the constant coefficients C_c, C_a, C_d, and C_a respectively modulate the dependence on the scale, on the axial induction factor a, on ambient turbulence intensity, and on downstream distance. The axial induction factor a is a measure of the momentum deficit experienced by air flowing past a wind turbine. It is directly related to the power and thrust coefficients of a wind turbine rotor.

Finally, depending on the wind direction, the turbines inside wind farms are often exposed to multiple wakes from several upstream wind turbines. These overlapping wakes are combined using wake superposition models. In some of the earliest work on wake superposition [126], velocity deficits were linearly combined, as it was assumed that the velocity deficit could be treated as a passive flow component, analogous to the transport of a passive scalar. A linear superposition scheme accounts for the continuous decrease in momentum with additional wakes and can be written, for each turbine wake i up to the total number N of wakes being considered, as:

$$u_i(x_w) = u_\infty - \sum_{i=1}^{N} \Delta u_i(x_w) * u_{\infty,i} \tag{3.24}$$

where $u_i(x_w)$ is the local average velocity field, $u_{\infty,i}$ is the local inflow velocity and $\Delta u_i(x)$ is the velocity deficit, defined as:

$$\Delta u_i(x_w) = 1 - \frac{u_i(x_w)}{u_{\infty,i}} \tag{3.25}$$

Other research suggested the superposition of energy deficits (rather than velocity or momentum), leading to a root-sum-squares formulation [127], or takes the maximum velocity deficit in any region of the flow [128].

Floris: a Wake Modelling Engineering Tool

Simulations using wake models are run with Floris (FLOw Redirection and Induction in Steady state) [129], developed by the National Renewable Energy Lab. This open-source code provides a modelling tool of the steady-state wake characteristics in a wind farm that integrates turbine interactions in wind power plants. Floris implements several wake models: in this work, gaussian models for wake deflection and velocity deficit are chosen, the Crespo-Hernandez approach

Table 3.2.: Wake models parameters for velocity deficit and added turbulence.

Gaussian velocity deficit			
k_a	k_b		
0.38	0.004		
Crespo-Hernandez model			
C_c	C_a	C_i	C_d
0.9	0.8	0.0325	-0.32

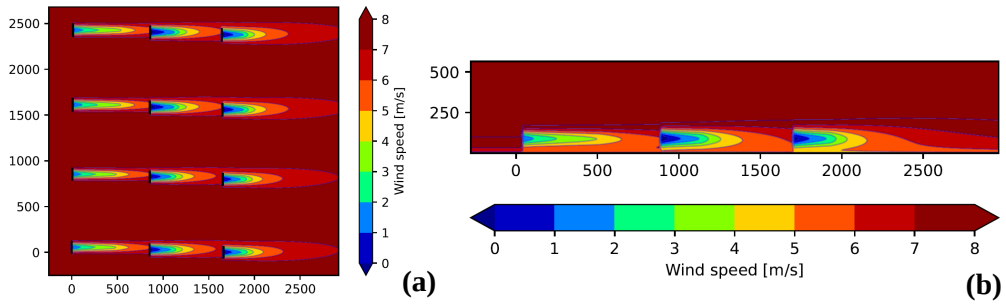

Figure 3.8.: Floris simulations of Alpha Ventus, for a wind speed of 8 m/s and a wind direction of 270°. (a) Horizontal plane cut through the simulation domain at hub height, (b) y-plane cut vertically through the flow field along the wind direction at x=0.

is selected for modelling added turbulence arising from turbine operation, and overlapping wakes are combined using a linear superposition approach. The parameters of the Gaussian velocity deficit and turbulence model are specified in Table 3.2, and are derived from the literature [130], [115].

In practice, the inputs needed by Floris simulations are the wind farm layout, the wind turbines characteristics (diameter and hub height), and a list of wind speeds and directions. Interestingly, the resulting database consists not only in the power output of the entire wind farm for a given set of wind speed and direction, but also integrates individual wind turbine power outputs as well as the waked wind speed u_{WT_i} seen at the rotor of each turbine WT_i. The modelled wind farm is the same as the one described in section 3.2.1: the 12-turbines offshore wind farm Alpha Ventus. Floris simulations of Alpha Ventus, for a wind speed of 8 m/s and a wind direction of 270°, can be seen in Fig. 3.8. This is the same wind case than in Fig. 3.5a of section 3.2.1.

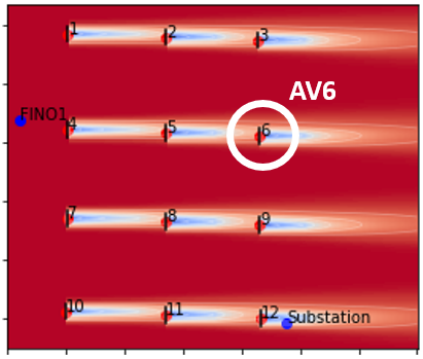

Figure 3.9.: Layout of the wind farm Alpha Ventus and the chosen wind turbine for the benchmark.

Similarly to RANS simulations, it is assumed that the wind turbine is actively controlled for maximum power point tracking and that the nacelle is always perfectly facing the main wind direction. However, if other wind farm controls (such as wake steering or axial induction control) were to be implemented in the future, it could be taken into account. To that end, new simulations where wind turbines are controlled with those strategies could be run, as Floris allows to do so [131].

3.3. Comparing RANS and Floris

In order to validate the two methodologies, a benchmark is set up for the Alpha Ventus wind farm. Times series from 2011 to 2014 of wind speeds and wind directions from the meteorological mast Fino 1 as well as SCADA measurements of electrical power output for one wind turbine in the centre of the wind farm are used as a reference for benchmarking. The measurements were pre-processed and filtered before being used to assess the accuracy of the wind farm simulations. The validation is done in terms of normalized power for a given wind speed over a wide range of wind directions. The reference wind turbine for the validation process is the AV6 turbine (highlighted in the Alpha Ventus layout of Fig. 3.9). When the wind direction is coming from the west and south (respectively wind direction of 270° and 180°), AV6 is in a double wake situation (wake coming from two upwind turbines).

In Fig. 3.10, the normalized power of the wind turbine is plotted against the wind direction, for a wind speed of 9.5 m/s. It can be seen that RANS simulations show a good agreement with the measurements: they are able to predict the width and depth of the power deficits. Floris simulations also

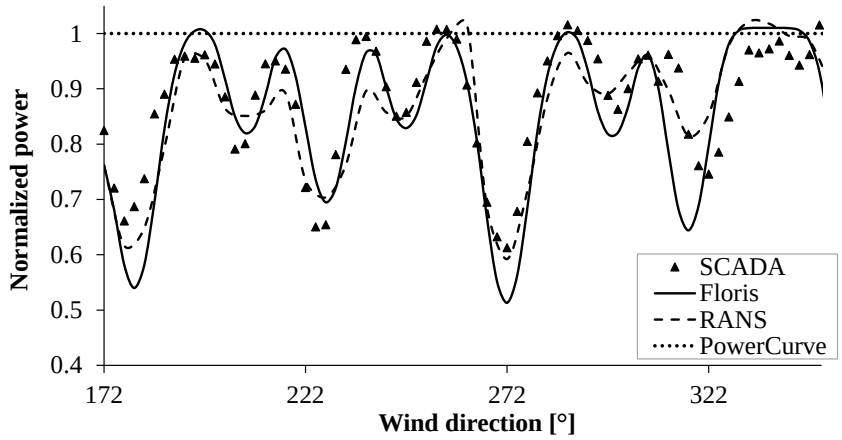

Figure 3.10.: Normalized power against wind direction computed with RANS simulations, Floris, and the power curve approach. Comparison with SCADA measurements.

exhibit a good fit with respect to the measurements. However, they sometimes overestimate the power deficit, and the RANS curve appears to follow the SCADA curve more accurately. The power curve approach does not consider wake effects and the power output of the wind turbine is constant for a given wind speed, independently of the wind direction. Considering that the maximum power loss can reach $\approx 50\%$ in full-wake conditions, this clearly emphasizes the limitations of such an approach. The slight discrepancies could be explained not only by modelling inaccuracies, but also by measurement noise. Moreover, compared with prediction simulation data, reproducing observational data is a more rigorous test for the model because field observations invariably involve uncertainty regarding the wind speed, wind direction and atmospheric stability conditions. The averaged profiles obtained from observations include various stability conditions and cannot be reproduced precisely by models trained on data from well-controlled numerical simulations under neutral stability [49]. Therefore, it can be concluded that both RANS and Floris simulations offer a good representation of reality when assessing the hourly mean power output of a wind turbine within a wind farm.

When studying the variation of wind power with regard to the wind direction, it can be seen that power drops happen when the wind turbine is in a waked condition. These drops can reach up to 50% of the normalized power. However, if the data points used to train the ML model do not cover these drops, then the subsequent model will not be able to capture power losses in an accurate way. It can be seen in Fig. 3.11 that the wind directions chosen as inputs to wind

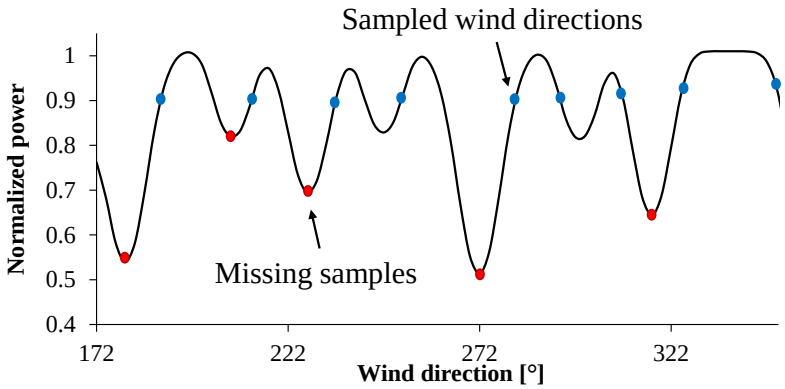

Figure 3.11.: Normalized power of a wind turbine with regard to wind direction: choosing enough data points.

farm simulations should be as close as possible to the power drops. Indeed, if wind directions are sampled in a regular way (blue points), and unfortunately lead to situations with reduced wake effects, power losses arising in more severe conditions (red points) will not be be captured. If such samples are not present in the database used to train the ML model, it will impossible for the latter to capture such phenomena. Granularity of data is thus really important when considering the output of a wind turbine in waked conditions. However, unless plotting every wind scenario, it is not feasible to know beforehand the exact wind directions of the power drops for each turbine in a farm. Therefore, it is preferable to have the highest data granularity as possible. In that case, building a relevant database with RANS simulations (1.67 CPU hour per run) can become too cumbersome. The accuracy that is gained by using more accurate simulations such as RANS is lost by having an incomplete database. Therefore, **Floris simulations based on wake models will be used to build the training database for the ML models**.

Nonetheless, it should be kept in mind that those conclusions are valid because we consider hourly power data (steady-state and averaged over an hour). If one wants to consider transitory effects and large turbulent scales, then the CFD simulations might be the only viable solution.

3.4. Building a Substantial Wind Farm Database

Our Floris-based simulation model is used on six real-life offshore wind farms to generate the training database for the ML model. The wind farms names and characteristics are the following:

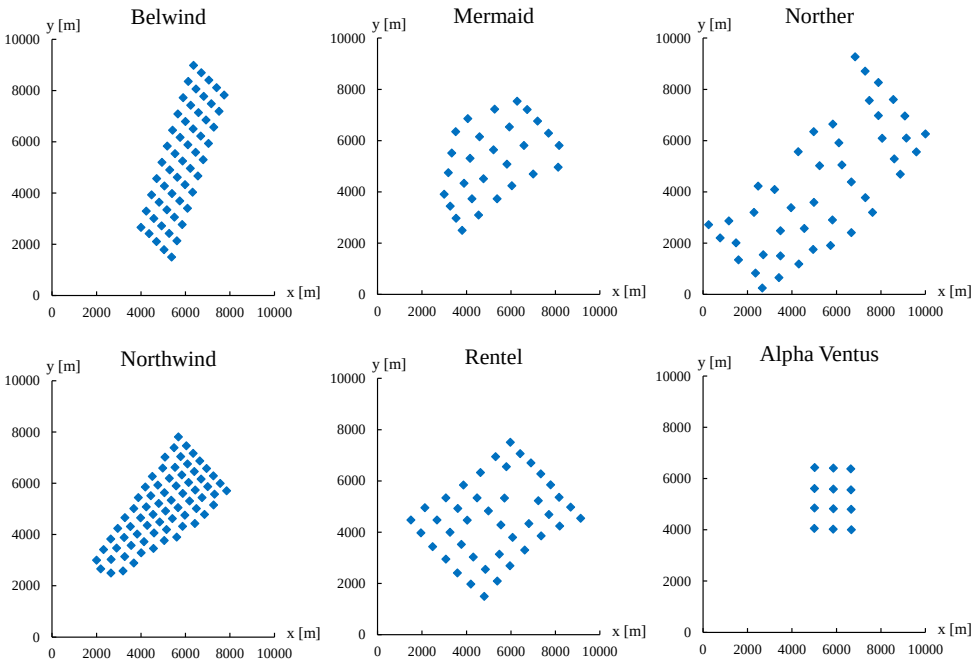

Figure 3.12.: Wind farms used for training the ML model. The scale is the same in all figures, to allow a visual comparison for density and turbine spacing.

- Alpha Ventus: 12 turbines, 4 km^2, 60 MW (15 MW/km^2)
- Belwind: 56 turbines, 17 km^2, 171 MW (10 MW/km^2)
- Mermaid: 28 turbines, 17 km^2, 235 MW (13.8 MW/km^2)
- Norther: 44 turbines, 44 km^2, 370 MW (8.4 MW/km^2)
- Northwind: 72 turbines, 15 km^2, 216 MW (14.4 MW/km^2)
- Rentel: 42 turbines, 23 km^2, 309 MW (13.4 MW/km^2)

They can be visualized in Fig. 3.12. They are all located in the North Sea but they offer variable characteristics in terms of layout and turbine technology. Indeed, their layouts show different wind turbine density, shape and number of turbines. The wind turbines have different rotor diameter, hub height and power curve shapes (see Table 3.3). For each farm, the layout (wind turbine coordinates) is publicly available [104], [132], and the wind turbine characteristics are extracted from manufacturers datasheets. Two wind farms (Belwind and Alpha Ventus) have heterogenous turbine types.

	Type	Rotor Diameter [m]	Hub Height [m]	Rated Power [MW]	Rated Wind speed [m/s]
Alpha Ventus	Adwen	116	90	5	12.5
	Senvion	126	94	5	14
Belwind	Vestas	90	72	3	15
	Heliade	150	100	6	13
Mermaid	Siemens	167	109	8.4	14
Norther	Vestas	164	105	8.4	13
Northwind	Vestas	112	71	3	13
Rentel	Siemens	154	105	7.35	13

Table 3.3.: Characteristics of the wind turbines used for training the ML model.

Regarding the list of wind speeds, wind directions and ambient turbulence used as inputs for wind farm simulations, the ERA5 dataset provided by the European Centre for Medium-Range Weather Forecasts (ECMWF) [133] is chosen. ERA5 is based on reanalysis to generate atmospheric time series covering a large period (from 1959 to 2024), with a spatial resolution of 31 km and an hourly temporal resolution. Reanalysis combines model data with observations from across the world into a globally complete and consistent dataset using the laws of physics. It provides a comprehensive description of the observed climate as it has evolved during recent decades, on 3D grids at sub-daily intervals.

For each wind farm, one year (2019) of hourly wind as well as extreme scenarios (very high wind speeds) at the location of the offshore wind farms were used as atmospheric inputs. Hence, a total of 52,746 (6*8791) simulations were run with Floris (presented in section 3.2.2). The resulting database consists not only in the aggregated power output of the entire wind farm, but also the individual wind turbine outputs, **taking into account potential turbine failures in the farm**. Those failures were randomly sampled from a probabilistic distribution based on offshore turbines reliability data. This means that some data samples represent situations where all turbines are operational, while other account for one or several simultaneous turbine failures.

Moreover, Floris also allows to run simulations with the option to ignore aerodynamic losses. This method is thus equivalent to the traditional way of modelling wind farms in iterative power system computations, where a simple aggregated power curve is used to match free-flow wind speeds to the

Table 3.4.: Comparison of mean annual energy production with and without aerodynamic losses, based on Floris simulations.

	Yearly Production With wake	Yearly Production Without wake	Yearly Wake losses
Alpha Ventus	230.76 GWh	241.82 GWh	4.57%
Belwind	585.25 GWh	650.19 GWh	9.99%
Mermaid	1008.86 GWh	1106.28 GWh	8.81%
Norther	1481.76 GWh	1617.87 GWh	8.41%
Northwind	848.67 GWh	1027.00 GWh	17.36%
Rentel	1148.44 GWh	1279.48 GWh	10.24%

power output. It is then possible to assess wake losses, by comparing the annual energy generation with and without taking into account wake effects. This comparison is presented in Table 3.4, where the mean annual energy is computed and averaged for the years 2019-2021 of the ERA5 dataset and for the six wind farms used for training. It can be seen that although wake losses are similar for the wind farms Belwind, Mermaid, Rentel and Norther (around 8 to 10%), they are significantly higher (17.4%) for Northwind. This can be explained by the different layout and distances between wind turbines. Indeed, as seen in Fig. 3.12, the layout of Northwind is more compact, thus leading to higher losses as the distance between wind turbines is not large enough to allow for wake recovery. Those results clearly emphasize the need to integrate site-specific aerodynamic effects in the offshore wind generation models used in power system computations, if one wants to have a reliable estimation of the real contribution of offshore wind farms.

3.5. Machine Learning Proxy

To train the ML surrogate, the database built in section 3.4 is used. Each wind turbine of every wind farm simulation is considered as a sample. Therefore, without pre-processing, each data sample represents an hourly value of wind speed, wind direction and ambient turbulence, and the corresponding wind turbine steady-state power. We predict the output of a single wind turbine because an evaluation at the turbine level gives a better insight of the ML models performance since turbine errors may compensate when powers are aggregated into total power at the farm level. Moreover, this allows to consider individual wind turbine outages when the model is used in adequacy studies (see section 4.2.3).

In order to have a single model applicable to any wind turbine within any wind farm configuration, cross-series learning is used. Cross-series learning is a technique that builds a single global model from multiple correlated series. After being trained, the global model can then make accurate predictions for any of the input series. Cross-series learning allows the effective learning of various common patterns observed among related series (cross-series information) [134]. In our case, the samples are correlated as the power produced by a wind turbine highly depends on the wake (and thus the power) generated by neighbouring turbines. Moreover, as only one model is built for multiple series, model selection and hyperparameters tuning have to be performed only once, thus saving time and computational resources.

The main challenge is to ensure that the trained ML model is generic, or topology-aware, for any wind farm configuration, i.e., the model should be able to make power assessments for a farm unseen in the training database. An important contribution of this work is therefore to enrich the input space with new features, including atmospheric, geometric, physics-informed, and turbine-specific information, which enable the ML model to generalize to any farm configuration. Moreover, while most ML models in the literature aim at predicting turbine power, **the direct output of our ML surrogate is the waked wind speed** u_{WT_i}, i.e., the wind speed seen at the rotor of the i^{th} turbine WT_i. This waked wind takes into account the influence of all upstream turbines on the free-flow wind speed (i.e., velocity deficit from the wake, but also wake recovery due to turbulence). Indeed, this allows our ML surrogate to generalize to turbine with different characteristics (e.g., different rotor diameter). To obtain the wind turbine power output, the waked wind speed is fed to the turbine power curve, then the wind farm total power is computed by summing individual turbine outputs. The process is detailed in Fig. 3.13. Practically, each sample consists of 16 input features, which are detailed hereafter, while the direct output of the ML model is the wind speed seen at the turbine rotor.

3.5.1. Features for the Topology-Aware Wind Farm Proxy

Atmospheric Features

The wind speed in front of the rotor directly determines the output generated by the turbine. However, this information is not readily available, so the free-flow wind speed measured upstream of the wind farm is used. If the wind measurement height is different than the turbines hub height, vertical extrapolation is carried out using the power law of Eq.(2.7). When taking wake effects into account, wind direction also has a crucial impact. However,

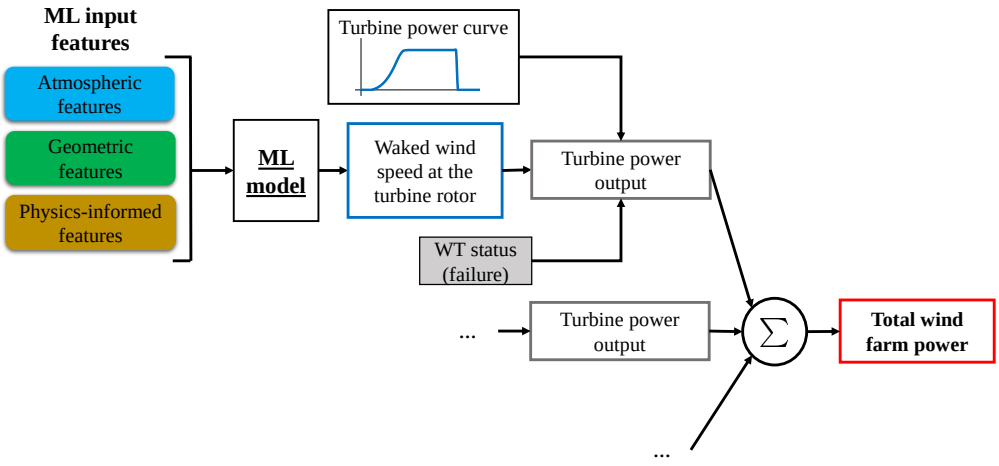

Figure 3.13.: Diagram of the methodology used to predict wind farm power with the topology-aware ML model.

wind direction is not directly used as a feature, but rather implicitly considered when computing the geometric and physics-informed features, as explained hereafter. Ambient turbulence is also an important factor because it influences wake recovery, as explained in sec. 2.4.

Geometric Features

For each sample (corresponding to a specific time step for a wind turbine within a farm), the computation of geometric features allows to convert information regarding wind direction and wind farm layout into usable inputs for the ML model. Based on the knowledge on how wake effects propagate and affect downstream turbines, the following features have been computed for every sample:

- Number of upstream blocking wind turbines

  This feature indicates the number of turbine located upwind, i.e., whose swept area (or part of) coincides with the rotor of the considered wind turbine, potentially affecting its wind access and performance. No blocking turbine means that the considered turbine is unwaked, and produces the maximum power computed for the free flow wind speed. However, more blocking turbines means less available energy in the wind seen by the rotor, thus a reduced wind speed seen at the turbine rotor (and less power produced). The relationship between the number of blocking turbines and the waked speed is not linear.

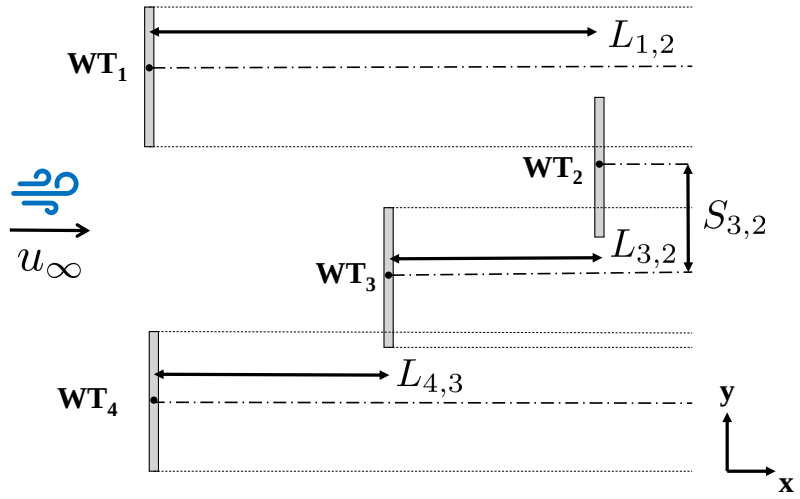

Figure 3.14.: Illustration of geometric features in a simple layout with 4 turbines. Plan view with wind blowing from 270° (rotor diameters are represented by grey rectangles and their swept area by dotted lines).

- Mean distance of blocking wind turbines

  The distances between the considered wind turbine and all upstream blocking turbines are averaged. Distances between turbines are computed perpendicularly to the rotor areas, in the direction of the flow. A high number may indicate a lower turbine density for the wind farm (turbines installed at a larger distance from one another), thus allowing for more wake recovery.

The two features described above are illustrated in Fig. 3.14. In this simple configuration, there are no turbines upstream of WT_1 and WT_4. Turbine WT_3 is only blocked by WT_4, whereas turbine WT_2 is partially blocked by both WT_1 and WT_3: the number of blocking turbines for WT_2 is thus 2, and the mean blocking distance is $(L_{1,2} + L_{3,2})/2$.

Wind farm measurements have shown that the closest upwind turbine aligned with the considered rotor has the most influence on power deficit [49]. Therefore, we identify the closest blocking turbine $WT_{b,1}$ of turbine WT_i in terms of streamwise direction (i.e., direction of mean flow).

- Streamwise distance of first blocking wind turbine

  This is the distance between the considered wind turbine WT_i and the closest upstream blocking turbine WT_b, in the streamwise direction.

- Lateral distance to first blocking turbine

  This distance is the shift between the considered wind turbine WT_i and the closest upstream blocking turbine WT_b, in the spanwise direction (i.e. direction perpendicular to the mean flow). Indeed, the velocity deficit will be maximum if the blocking rotor is completely shadowing the considered turbine. This distance is computed between rotor centrelines.

- Rotor diameter of first blocking turbine

  A turbine with a larger rotor diameter generally extracts more power from the incoming wind, as turbine power is proportional to the square of the rotor radius (see Eq.(2.4)). Therefore, for the same streamwise distance, a larger turbine will lead to a increased velocity deficit in the wake, thus reducing the waked wind speed seen at the rotor of the considered turbine WT_i.

In Fig. 3.14, while turbine WT_2 is blocked by both WT_1 and WT_3, the closest blocking turbine in terms of streamwise distance is WT_3, as $L_{3,2} < L_{1,2}$. Therefore, the lateral distance to the first blocking turbine is $S_{3,2}$. The rotor diameter of WT_3 is also used as feature.

There may be multiple upstream turbines that block the same or additional portions of the swept area of a given turbine. Moreover, as stated before, blocking turbines that are closer have more influence on the waked wind speed at the rotor of turbine WT_i. However, if those turbines are not completely aligned with the considered rotor, their influence decreases. The combination of those two aspects are captured by the two last geometric features described below.

- Blocking ratio

  This is the fraction of the swept area of turbine WT_i that is blocked by the swept area of any wind turbine upstream [135]. This blocking ratio BR_i varies between 0 (not blocked) to 1 (totally blocked) and is computed as:

$$BR_i = \frac{1}{A_i} \int_{(x,y)\in A_i} \chi \, dx \, dy \tag{3.26}$$

  where

  A_i is the swept area of the rotor of turbine WT_i

  (x, y) are grid points on the rotor disk

$$\chi = \begin{cases} 1, \text{ if the grid point is blocked by any turbine} \\ 0, \text{ otherwise.} \end{cases}$$

- Blocking distance

  It represents the weighted average distance to the upstream blocking turbines. The blocking distance BD_i of turbine WT_i is defined as:

$$BD_i = \frac{1}{A_i} \int_{(x,y)\in A_i} [\chi * \min(L, L_\infty) + (1 - \chi) * L_\infty] \, dx \, dy \tag{3.27}$$

  where

  L is the distance between the grid point and any upwind blocking turbine

  $L_\infty = 20 * D$ (for grid points not blocked by any upwind turbine)

  The blocking distance can be seen as the average distance to the upstream blocking turbines, weighted by the fraction of the area obstructed by each upstream blocking turbine. The term L_∞ is an arbitrary large but finite length ensuring that the integral remains finite. In this study, L_∞ is set to a distance equal to 20 rotor diameters since previous studies have shown that the velocity profile in a turbine wake almost entirely recovers its original shape at 20 rotor diameters downstream of the turbine [51].

The blocking ratio and blocking distance are illustrated in Fig. 3.15 (this is the same layout than the one in Fig. 3.14 but seen from a different perspective). Since turbines WT_1 and WT_4 are unwaked, their blocking ratio BR_1 and BR_4 are equal to 0. If turbine WT_2 is considered, it can be seen that its swept area is partially blocked by WT_3 and WT_1, such that $0 < BR_2 < 1$. For examples, for three points (marked by circles) of turbine WT_2, it can be seen that P_1 is blocked by WT_3, located at a streamwise distance $L_{3,2}$, P_2 is not blocked, and P_3 is in in the wake of WT_1 distant of $L_{1,2}$. It should be noted that if a same point is blocked by several turbines, L is the distance to the closest blocking turbine.

As a reminder, it is assumed in the calculations of these geometric features that the turbine yaw angle changes with the wind direction (greedy control strategy) so that the swept area is always perpendicular to the incoming wind. Moreover, for the computation of the blocking ratio and distance, the swept area of each turbine is divided into a large number of discrete areas, and the integrals in Eq.(3.26) and (3.27) are evaluated numerically to give the geometric measures.

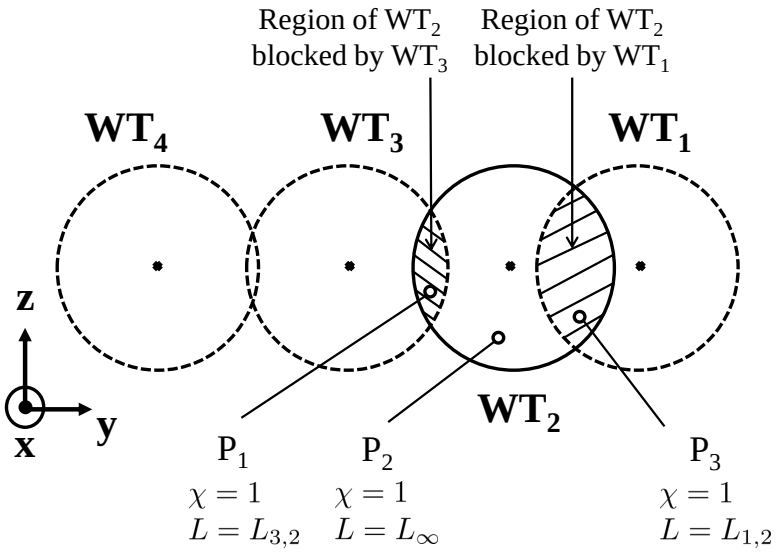

Figure 3.15.: Illustration of geometric features in a simple layout with 4 turbines (identical to the one in Fig. 3.14). Plane cut vertically through the flow field across the wind direction, behind WT_2.

Physics-Informed Features

Complex ML models (such as deep neural networks, or random forests with numerous deep trees) can be plagued by a black-box nature, which makes them difficult to interpret and prone to produce physically impossible results. A recent field of research that has focused on solving this problem is physics-informed Machine Learning [136]. Physics-informed Machine Learning is characterized by the exploitation of the scientific knowledge or the physics laws to guide the optimization, architecture design, and implementation of ML models. In particular, physics-informed feature engineering refers to leveraging the insights of prior physical knowledge to select, transform, and synthesize the most informative input variables from raw data for the ML model [137].

Geometric features simply describe the layout of the wind farm, and it uses turbine rotor diameters to compute the swept area of the upstream turbine rotor and the subsequent wake diameter. However, it is known that the wake expands behind a turbine, meaning that the diameter of the wake increases with the downstream distance [138]. The model performance could be improved by adding information regarding this physical aspect. Indeed, when using only geometric features, the ML model may infer that some turbines are exposed to free-flow wind (if the number of blocking turbines found using rotor diameters is equal to 0), while they are in fact slightly in the wake of another turbine. This

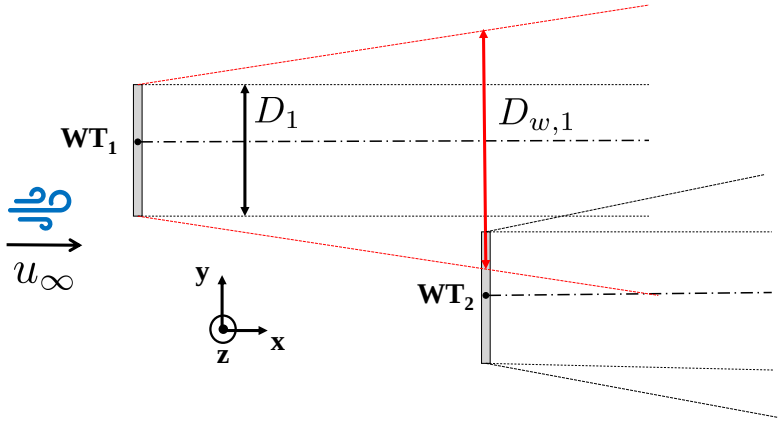

Figure 3.16.: Illustration of geometric features in a simple case with 2 turbines. Plan view where rotor diameters are represented by grey rectangles and their swept area by dotted lines. The wake expansion is shown by the red dashed lines.

could happen if the turbines are not directly aligned such that the downstream turbine is not in the wake cylinder whose cross section is computed using the upstream turbine rotor diameter, but within the cylinder of a an expanded wake. This is depicted in Fig. 3.16.

The determination of the diameter of the expanded wake at the rotor of the downstream turbine bears physical meaning, allowing the ML model to produce results more in line with aerodynamic rules. However, computing this wake diameter should be fast and straightforward, otherwise it will hinder the computation time of ML input features and the speed advantage of using ML will be lost. This is why we use the very simple Jensen wake model [111] to compute the wake diameter D_w. The Jensen model was described in section 3.2.2, but as a reminder, the wake diameter is computed as follows:

$$D_w = D + 2 * k_w * x_w \tag{3.28}$$

where k_w is the Jensen wake spreading parameter, D the wind turbine diameter and x_w the distance downstream behind the turbine. In offshore conditions, k_w is usually set to 0.05 [53]. Therefore, additional values for the number of blocking turbines, mean blocking distance, distance/shift/rotor diameter of the first blocking turbine, blocking ratio and blocking distance are computed. They result from the same equations as for the geometric features, but use a wake diameter D_w instead of turbine rotors D. These new inputs are called physics-informed features.

3.5.2. Supervised Machine Learning Algorithms

Supervised learning is used to learn hidden structures where output data are known. The user provides the supervised algorithm with N pairs of inputs (or features) $\boldsymbol{X} = (x_i)_{i=1}^N$ and desired outputs (or labels) $\boldsymbol{y} = (y_i)_{i=1}^N$, and the algorithm aims at producing the desired output for a given input. In particular, it is able to create an output for an input it has never seen before. The goal is thus to bypass the (possibly complex) physical modelling of the underlying phenomena, by directly exploiting the information contained in the data [139]. While creating a dataset of inputs and outputs is often a laborious manual process, supervised learning algorithms are well understood and their performance is easy to measure [83]. Popular methods of supervised learning include artificial neural networks, decision trees, k-nearest neighbours, linear and polynomial regressions, and support vector machines. The choice of algorithm depends on the data (structure, quantity) and on the problem to be solved. For our ML surrogate, the goal is to predict waked wind speed at the turbine rotor, which is a continuous number: our problem is a regression task.

The relationship between the waked wind speed and the proposed input features is highly non-linear, which motivates the use of the four following supervised ML algorithms.

Decision Tree

Decisions trees are a non-parametric supervised learning method whose goal is to create a tree-like model that predicts the value of a target variable by learning simple decision rules inferred from the data features [140]. A diagram of a decision tree is shown in Fig. 3.17: each node describes a decision criterion considering one particular feature (e.g., comparison with a threshold value). To build a decision tree, all training samples are first gathered in the root node, then each division, called "split", separates each node in two other nodes. The splitting criteria is based on the definition of an impurity function and partitions the feature space such that the samples with the same labels are grouped together. The recursive partitioning of the data is repeated until each leaf in the decision tree only contains a single regression value ("pure" leaf). However, building a tree as described here and continuing until all leaves are pure leads to models that are very complex and highly overfit to the training data. Indeed, the presence of pure leaves mean that a tree is 100% accurate on the training set. One way to avoid overfitting is pre-pruning, i.e., stopping the creation of the tree early. Possible criteria for pre-pruning include limiting the maximum depth of the tree, limiting the maximum number of leaves, or requiring a minimum number of points in a node to keep splitting it. In this work, the hyperparameter used to tune a decision tree is the **maximum depth**

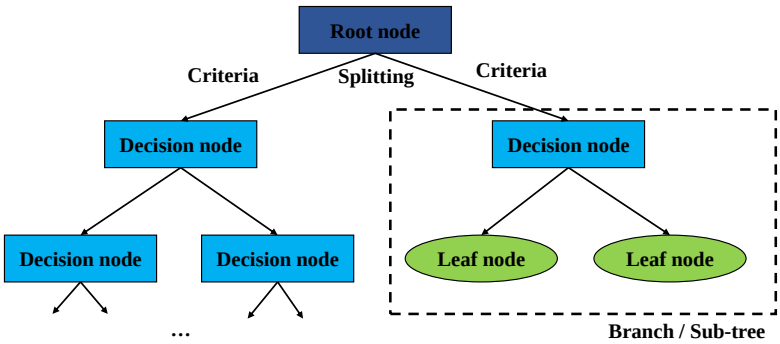

Figure 3.17.: Diagram of a decision tree.

of the tree. Finally, to make a prediction, the tree is traversed based on the tests in each node and finds the leaf where the new data point falls into. The output for this data point is the mean target of the training points in this leaf.

Advantages of decision trees is that they are easily interpreted if the size is small, and there is no need for a heavy data preparation as they are able to work with features of different scale. However decision trees tend to overfit (even with pre-pruning) and their generalization performance can sometimes be poor. Moreover, decision trees can be unstable because small variations in the data might result in a completely different tree being generated.

Random Forest

To mitigate the overfitting problem of a single tree, several decision trees can be combined so that the variance of the resulting model is decreased. Random forests are an ensemble method, which involves combining multiple machine learning models to create more powerful models. A random forest is essentially a collection of decision trees established in a independant way [141]. Each tree is built on a random sub-sample of the training data set drawn with replacement (i.e., a bootstrap sampling). The purpose of this randomness is to make every tree slightly different from the others and thus to decrease the variance of the random forest. Indeed, as individual decision trees typically exhibit high variance and tend to overfit, the injected randomness in forests yield decision trees with somewhat decoupled prediction errors. To make a prediction using the random forest, the algorithm first makes a prediction for every tree in the forest, then average these results to get the final prediction (as seen in Fig. 3.18). By averaging the results of all trees, the overall overfitting is highly reduced. The main parameters to adjust when using this method is the **maximum depth of the trees** (similarly to single decision trees) and

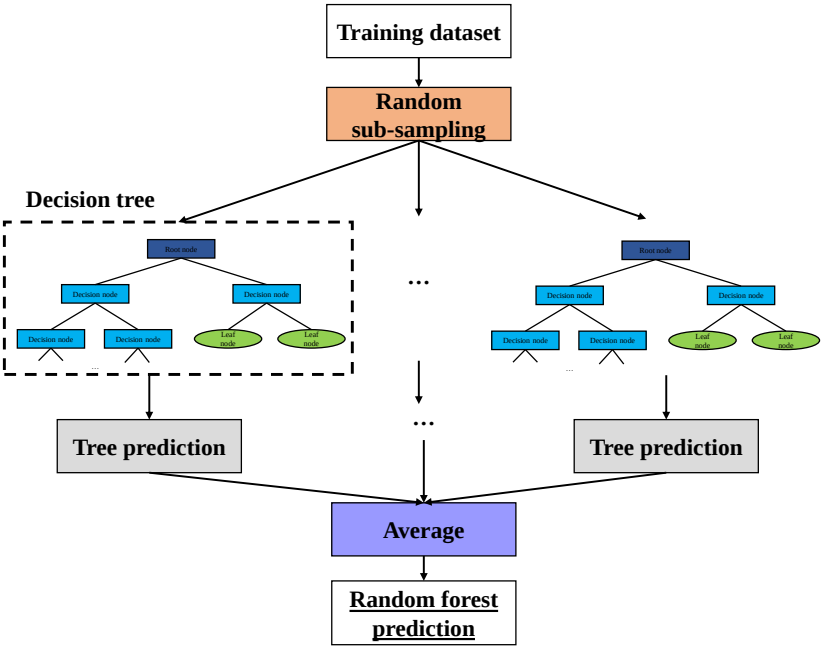

Figure 3.18.: Diagram of a random forest of decision trees.

the **number of trees** (or estimators) in the forest.

Essentially, random forests share all of the benefits of decision trees, while making up for some of their deficiencies. They do not require heavy tuning of the parameters nor scaling of the data. Moreover, because trees are built independently, training can be easily parallelized across multiple CPU cores within a computer. The drawbacks of random forests are their poor performance when applied on very high dimensional and sparse data, as well as the increasing memory requirement and computational time with the number of trees. Indeed, averaging more trees will yield a more robust ensemble by reducing overfitting (although there are diminishing returns [83]).

Gradient Boosting Regression Trees

Gradient Boosting Regression Tree (GBRT) is another ensemble method combining multiple trees. The main idea behind gradient boosting is to combine many simple models (weak learners), like shallow trees. In contrast to random forests, this algorithm builds trees in a sequential way so that each new tree attempts to improve the errors made by the previous one. The gradient boosting iteratively fits new weak learners on the negative gradient of a given loss function. The model is then updated by adding the new tree, weighted by a

Algorithm 1 Algorithm for gradient boosting regression trees

Let $(x_i, y_i)_{i=1}^N$ be the training set, $\mathcal{T}$ the model to build, T a decision tree, $\mathcal{L}(y, \mathcal{T}(\boldsymbol{X}))$ a differentiable loss function, M the number of iterations.

Initialize the model:
$\mathcal{T}(\boldsymbol{X}) = \text{argmin}_\gamma \sum_{i=1}^N \mathcal{L}(y_i, \gamma)$

for $m = 1$ to M **do**

1. Compute pseudo-residuals

$$r_{m,i} = -\left[\frac{\partial \mathcal{L}(y_i, \mathcal{T}(x_i))}{\partial \mathcal{T}(x_i)}\right]_{\mathcal{T}=\mathcal{T}_{m-1}} \quad i = 1...N$$

2. Fit a new tree $T_m(\boldsymbol{X})$ to the pseudo-residuals using the training set $(x_i, r_{m,i})_{i=1}^N$

3. Compute multiplier γ_m by solving

$$\gamma_m = \underset{\gamma}{\text{argmin}} \sum_{i=1}^{N} \mathcal{L}(y_i, \mathcal{T}_{m-1}(x_i) + \gamma * T_m(x_i))$$

4. Update the model

$$\mathcal{T}_m(\boldsymbol{X}) = \mathcal{T}_{m-1}(\boldsymbol{X}) + \eta * \gamma_m * T_m(\boldsymbol{X})$$

end for

Output $\mathcal{T}_M(\boldsymbol{X})$

multiplier computed using the loss function [142]. The procedure is detailed in Algorithm 1.

Apart from the **maximum depth** and the **number of trees** in the ensemble, another important parameter of gradient boosting is the **learning rate** η, which controls how strongly each tree tries to correct the mistakes of the

previous trees. A higher learning rate means that each tree can make stronger corrections, allowing for more complex models. Adding more trees to the ensemble can improve performance as the model has more chances to correct mistakes on the training set, but it also increases the model complexity.

Gradient boosted trees offer the advantage of often using very shallow trees, which makes the model smaller in terms of memory and predictions faster. The main drawback of the GBRT method is the difficulty to find the optimal hyperparameters, as it is highly sensitive to the calibration of their values. The tuning of hyperparameters can thus be a cumbersome process. Moreover, since trees are built in a sequential way, the model is slower to train (no parallelization, unlike random forests).

Feed-Forward Neural Network

An artificial Neural Network (NN) is a Machine Learning model inspired by the structure and function of biological neural networks in human brains [143]. A neural network consists of units (neurons) connected by weighted edges (synapses) with the goal of mathematically representing any relationship between inputs and outputs. Each artificial neuron receives signals from connected neurons, processes them using a non-linear function of the sum of its inputs (called the activation function), then sends a signal to other connected neurons. The strength of the signal at each connection is determined by weights, which are optimized during the learning process. Usually, neurons are aggregated into layers. For a neuron in layer l, receiving H input signals from the previous layer $l-1$, the neuron output s_h^l can be computed as:

$$s_h^l = f_h^a\left(\sum_{h'=1}^{H} w_{h',h} * s_{h'}^{l-1}\right) \tag{3.29}$$

where $w_{h',h}$ is the weight of the connection between unit h' to unit h, and $f_h^a(.)$ is the activation function. This is further illustrated in Fig. 3.19.

For a Multi-layer Perceptron (MLP), or feed-forward neural network, inputs travel from the first layer (the input layer) to the last layer (the output layer), possibly passing through multiple intermediate layers (hidden layers) in a forward way: this is called a forward pass of the network. This can be observed in Fig. 3.20.

The hyperparameters to adjust are the **number of hidden layers**, the **number of neurons in each hidden layer**, as well as the **activation function**. Common options for the activation function include the hyperbolic

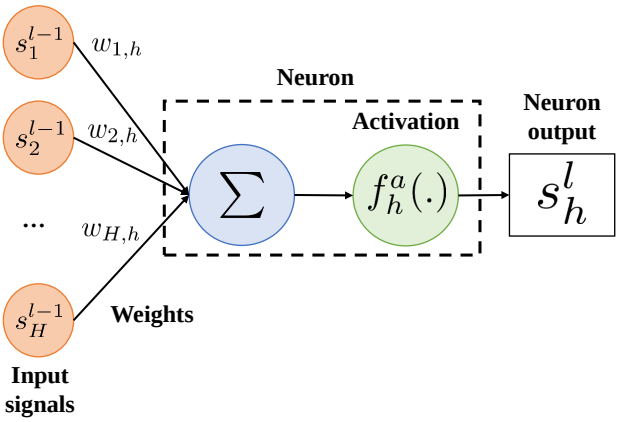

Figure 3.19.: Diagram of an artificial neuron activation.

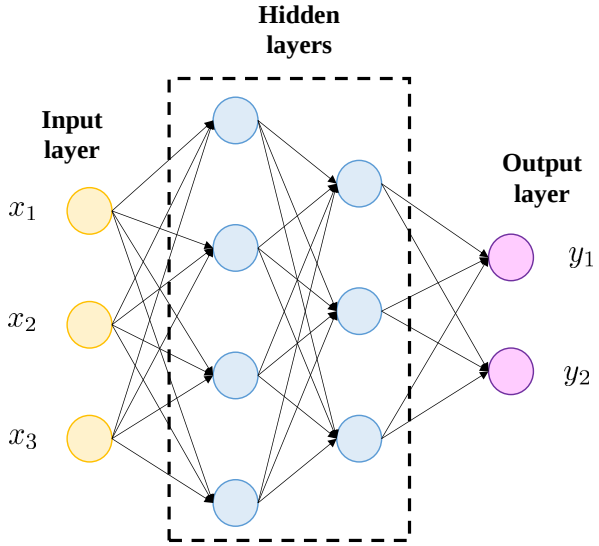

Figure 3.20.: Example of a MLP structure.

tangent, the logistic sigmoid and the Rectified Linear Unit (ReLU) (their shape is pictured in Fig. 3.21). These functions are nonlinear, which can significantly improve the NN performance, and the hyperbolic tangent and logistic sigmoid functions are differentiable, thus making them suitable for gradient methods. The ReLU function is continuous but it is not differentiable at the origin, as it can be seen in Fig. 3.21. However, to overcome this issue, the derivative is simply set to 0 at the origin, as it has been proven to be efficient [144] and being exactly at the origin during ReLU computations is extremely rare. The

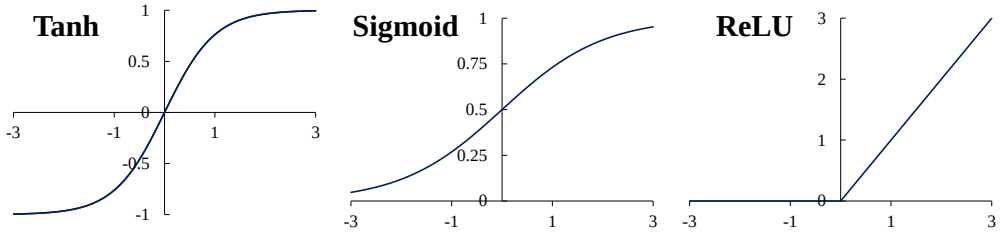

Figure 3.21.: Common activation functions for MLP.

differentiability aspect will be particularly important for Chapter 5.

One of the main advantages of MLPs is their ability to capture information contained in large amounts of data and to build incredibly complex models. However, neural networks (particularly large ones) often take a long time to train and require a careful tuning of the hyperparameters. Moreover, MLPs are sensitive to feature scaling, thus input data should be carefully pre-processed.

Training, validating and estimating performance

The database built in section 3.4 is used to train the models built on the ML algorithms described above. Their training performance is then assessed using an appropriate error with respect to the considered task. For example, the coefficient of determination, noted r^2, represents the proportion of variance of $\boldsymbol{y}$ that has been explained by the independent features $\boldsymbol{X}$. It provides an indication of goodness of fit and therefore a measure of how well unseen samples are likely to be predicted by the model, through the proportion of explained variance. It is computed as follows:

$$r^2 = 1 - \frac{\sum_{i=1}^{N}(y_i - \hat{y}_i)^2}{\sum_{i=1}^{N}(y_i - \overline{y})^2} \tag{3.30}$$

where $\hat{y}_i$ is the model prediction of the i-th sample, y_i is the corresponding true value, and $\overline{y}$ is the average of all labels $\overline{y} = 1/N \sum_{i=1}^{N} y_i$. The best possible score is 1, which means that all outputs predicted by the model are strictly equal to their true value.

Although the training score assesses the performance of the model on the training set, it cannot be directly used to evaluate the ability of the model to make good predictions of unseen samples, i.e. its generalization abilities. To assess the model performance, it should be fed with new data that it has not seen during training, for which labels are available. This is usually done by

splitting the labelled data at disposal into two parts. One part of the data, the **training set**, allows to build the ML model and the rest of the data, the **test set**, is used to assess how well the model performs and generalizes. In our case, the test set consists of a database of simulations performed on an unseen wind farm, with different characteristics than the ones in the training set (this will be further detailed in the next section). Therefore, the only measure of whether an algorithm will accurately generalize on new data is the evaluation on the test set, which can be carried out using various error metrics. Besides the coefficient of determination r^2, other metrics include the Root Mean Squared Error (RMSE) and Mean Absolute Error (MAE). The RMSE is more sensitive to outliers and penalises large errors, while the MAE simply measures the average magnitude of the errors in a set of predictions, without considering their direction. Lower RMSE and MAE values are associated with more accurate models, and should thus be targeted. They are computed as follows:

$$RMSE = \sqrt{\frac{1}{N} * \sum_{i=1}^{N} (y_i - \hat{y}_i)^2} \tag{3.31}$$

$$MAE = \frac{1}{N} * \sum_{i=1}^{N} |y_i - \hat{y}_i| \tag{3.32}$$

Building a model that is too complex for the amount of information is called overfitting, which is usually characterized by a test score rather worse than the training score. Overfitting occurs when the model is fit too closely to the particularities of the training set. On the other hand, if the model is too simple, it might not be able to capture all the aspects and variability in the data, and will do badly even on the training set: this is called underfitting. There is thus a compromise to be found for the model complexity.

One way to control the model complexity is by carefully tuning the hyperparameters. However, this calibration cannot be performed on the test set, as any choice based on the test set accuracy leaks information from testing data into the model. Therefore, it is important to keep the test set separate, and only use it for the final evaluation. One way to resolve this problem is to split the data again (resulting in three datasets) to obtain a **validation set**, used to tune the hyperparameters. In our case, the validation set consists of a database of simulations performed on another unseen wind farm, different from the one used for the training and test sets (it will be described in the next section). The hyperparameters of each model are chosen to maximize the accuracy on

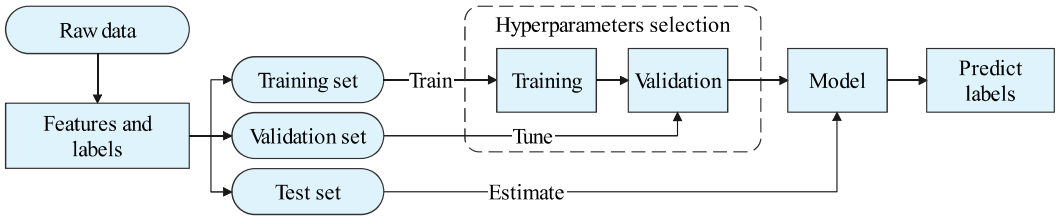

Figure 3.22.: Process to build a supervised ML model [145].

the validation dataset.

To summarize, training data are used to build/train the ML model, validation data help selecting the hyperparameters, and test data are leveraged to evaluate the performance and generalization abilities of the model. The process is outlined in Fig. 3.22. Finally, once the model has been trained, tuned and tested, it can be stored and later used to make predictions, which is called *inference* or *online utilization*.

3.6. Verification and Validation

3.6.1. Performance of the Machine Learning Model

The synthetic database of section 3.4 was used to train the topology-aware ML model. To find the best (combinations of) hyperparameters for the supervised ML algorithms, a validation dataset of wind farm simulations is set up. The latter consists in hourly simulations performed on the Lillgrund offshore wind farm, using Floris and one year (2020) of ERA5 wind data. Lillgrund is located near the coast of Sweden, and the layout of the wind farm is presented in Fig. 3.23(a). This wind farm has a total rated capacity of 110 MW and consists of 48 pitch-controlled, variable speed wind turbines with a rotor diameter of 93 m and a hub height of 65 m. The layout is quite tight, with a mean turbine spacing of 3.3 rotor diameters. The hyperparameters of each ML model were calibrated with a thorough grid search performed on the validation set, and the obtained optimal architectures are:

- Decision tree
  - maximum depth of 20
- Random forest
  - 50 trees
  - maximum depth of 25

- Gradient boosting regression tree
  - 50 trees
  - maximum depth of 15
  - learning rate of 0.1
- Multi-layer perceptron
  - 2 layers of 50 neurons each
  - ReLU as activation function.

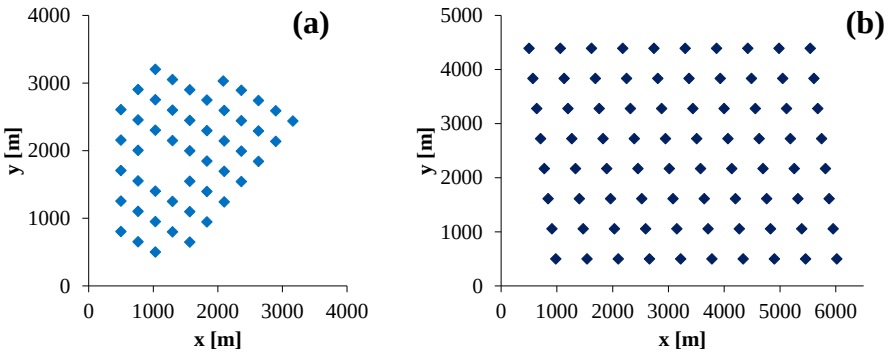

Figure 3.23.: Layout of the (a) Lillgrund and (b) Horns Rev offshore wind farms

Moreover, to quantify the performance of the ML surrogate and assess its ability to generalize to unseen data, the model is evaluated on a test set, which is composed of a new wind farm. The latter consists in hourly simulations performed on the large offshore wind farm Horns Rev, using Floris and one year (2021) of ERA5 wind data. Horns Rev is located in the eastern North Sea, near the coast of Denmark. It consists of 80 wind turbines (Vestas V-80), whose rated power is 2 MW, hub height is 70 m above sea level and rotor diameter is 80 m. The wind farm layout (Fig. 3.23(b)) has a rhomboid shape with a minimum spacing of seven rotor diameters between two consecutive turbines. The total area of the wind farm is about 20 km^2 and the total installed capacity is 160 MW, meaning a power density of 8 MW/km^2. Similar to the training database, random turbines failures are also added to the test set. The performance of each ML model is given in Table 3.5. The RMSE and MAE are computed and given in MW but also in percentage (RMSPE and MAPE) of the wind farm total installed capacity (160 MW for Horns Rev). The inference time corresponds to the total time for obtaining a yearly output of 8760 samples. The chosen algorithm should reflect the best compromise between accuracy, inference time and model complexity.

Table 3.5.: Performance of the Machine Learning models on the test set.

	Tree	RF	GBRT	NN-MLP
RMSE [MW]	2.47	2.23	1.93	1.57
RMSPE [%]	1.54	1.40	1.20	0.98
MAE [MW]	1.28	1.07	1.05	0.84
MAPE [%]	0.80	0.67	0.66	0.53
Inference time [s]	0.31	2.09	0.32	1.77

The four ML models show strong performance regarding both accuracy and inference time. The decision tree has a very low prediction time, but has the highest RMSE (decision trees are prone to overfitting). Random forests exhibit lower errors, but at the cost of a higher inference time. The GBRT algorithm seems to offer a good compromise between accuracy (low errors, with RMSE around 1% of wind farm total capacity) and computation time. The MLP is slower, but shows lower errors than random forests and GBRT, with both RMSE and MAE under 1% of the wind farm rated capacity. **Neural networks (MLP) are thus the supervised algorithm chosen for rest of this work. Throughout the remainder of this thesis, the term "ML surrogate" will refer to the model trained using MLP**.

It should be noted that the time needed to calculate geometric and physics-informed features is to be added to the inference time. For Horns Rev, the computation time is around 10.3 s, which brings the total inference time between 10.6 s and 12.39 s. This value is much lower than the 332 s needed to carry out 8760 simulations (i.e., one year) of Horns Rev with Floris. This means that the ML model is more than 25 times faster than wind farm simulations, making it ideally suited for computations where wind farm total power has to be simulated for thousands or even millions iterative steps.

3.6.2. Validation with High-Fidelity Simulations

We also validate our physics-informed ML surrogate of offshore wind generation with very high-fidelity results of the test offshore wind farm Horns Rev, carried out in [50] using large eddy simulations. Comparisons are performed for a given wind speed over a wide range of wind directions. In Fig. 3.24, the total power of the entire farm is represented as a function of the wind direction, for a wind speed of 8 m/s. This wind speed is selected to be below the Vestas V-80 turbine rated speed to more significantly highlight the impact of wake effects.

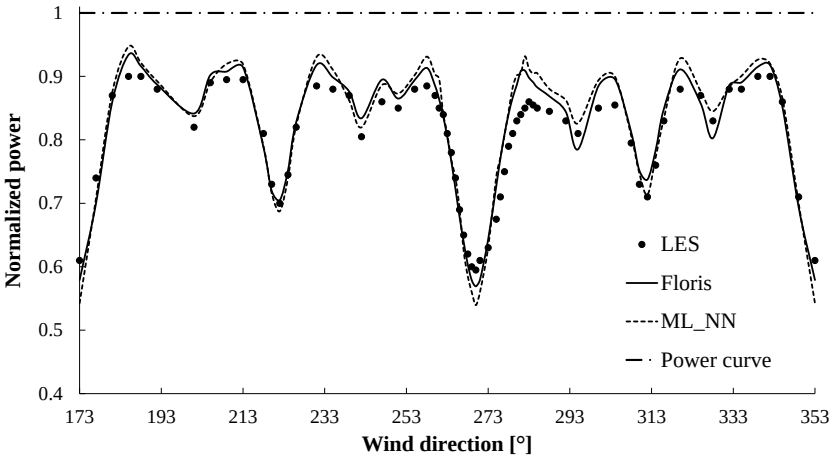

Figure 3.24.: Comparison of normalized farm power at Horns Rev for a wide sector of wind directions and a wind speed of 8 m/s.

On the y-axis, the wind farm power is normalized by the unwaked power, so that the curves reflect the power losses arising from aerodynamic effects.

First, it can be seen that Floris simulations (full curve) provide a good fit with respect to the high-fidelity simulations (scatter points): they are able to accurately capture the width and depth of power deficits. As it has already been observed through low values of RMSE and MAE, the power estimations given by the MLP model (dashed curve, ML_NN) closely follows Floris simulations, such that they also accurately match the LES points. The average absolute error between LES points and ML-based power is 2.92%, and the maximum error reaches 8.17%. Since the traditional power curve approach ignores wake effects, the power remains constant (at 1 p.u.) for a given wind speed, independently of the wind direction. With the power curve method, the average absolute error with respect to LES simulations is 20.06 % and the maximum error can reach 40.50% in full wake conditions (i.e., for a wind direction when turbines in a row are perfectly aligned). These observations confirm the relevance of the proposed model, while clearly emphasizing the limitations (i.e., high errors) of the power curve approach.

3.7. Conclusion

In power systems problems involving iterative computations, simplified offshore wind farm models often disregard complex aerodynamic effects due to the computational issues associated with accurately representing them. However, those effects have a significant impact on the produced electricity. In this chapter, a new methodology is developed to improve the modelling of offshore wind power within time demanding computations. A Machine Learning-based wind farm surrogate is created, allowing to account for aerodynamic losses arising in large offshore wind farms without compromising tractability. The model is trained on a large database built using aerodynamic simulations of real-life wind farms. Two methods for carrying out wind farm simulations are compared: RANS simulations and wake models. Although the RANS approach could yield more accurate results (especially for deeper wind farms), the computation time is prohibitive and does not allow to build a significant training database. Therefore, wake models are used to run numerous wind farm simulations. The ML model is then fed by new geometric and physics-informed input features such that the ML surrogate is generic and topology-aware, i.e., it can be applied to any offshore wind farm. This enables simulating wind farms without historical data, such as those yet to be built. Moreover, this model allows to account for disabled turbines (failures or maintenance) and the subsequent wake redistribution.

The performance of different standard supervised ML algorithms are compared, and the model is validated against very high-fidelity simulations. Neural networks (more specifically multi-layer perceptrons) are the supervised algorithm chosen for the ML model. The computation time is detailed, and compared against wind farm simulations carried out with wake models: the general surrogate is shown to be more than 25 times faster. Moreover, the proposed methodology is easy to implement and to reproduce, as it only uses publicly available data and simulation outputs.

The developed topology-aware ML models can thus be directly integrated within problems involving iterative computations, e.g., adequacy studies using sequential Monte-Carlo simulations. This will be carried out in the next chapter.

Chapter Publications

- **T-H. Nguyen**, J-F. Toubeau, E. De Jaeger, and F. Vallée, "Topology-aware Surrogate for Future Offshore Wind Farms Using Machine Learning", submitted to *Applied Energy*

- **T-H. Nguyen**, J-F. Toubeau, E. De Jaeger and F. Vallée, "Fast and Reliable Modelling of Offshore Wind Generation for Adequacy Studies," *IEEE Transactions on Industry Applications*, vol. 59, no. 6, pp. 7116-7125, 2023
- **T-H. Nguyen**, N. Thils, J-F. Toubeau, E. De Jaeger, and F. Vallée, "Offshore Wind Farm Power Prediction for Security of Supply Assessment Using a Unique Machine Learning Proxy", *2022 EAWE PhD seminar*, Bruges, Belgium, 2022

CHAPTER 4.

Improved Modelling of Offshore Wind Generation in Adequacy Studies

Offshore wind power is intrinsically intermittent and uncertain. Growing concerns are thus expressed regarding the reliability of future power systems, notably regarding the security of supply. In adequacy studies, the traditional way of modelling offshore wind generation consists in generating free-flow wind speeds and converting them to power through the use of a single wind turbine power curve. This power output is then multiplied by the number of turbines to assess the global power generated by the wind farm [146]–[149]. We further call this methodology the *traditional power curve approach*. Such strategies are undermined by the fact that they neglect important factors, such as wind shear, turbulence and wake effects. Those effects, which depend on parameters such as the wind farm layout or the distance between turbines, clearly influence the expected power output, and they must not be disregarded. In the current literature, this aspect is either neglected or modelled in a highly simplified fashion through an efficiency coefficient (typically assumed to be equal to 90%-95% of the total wind farm power [150] or computed using the approximated Jensen wake model [151], [152]). Since wake losses are a major issue for offshore wind farms (they can cause annual energy losses of 10 to 20% [103]), this clearly motivates their inclusion into power system adequacy studies.

The objective of this chapter is thus to account for intra-farm wake losses arising in offshore wind farms in the context of adequacy studies. This is accomplished by directly integrating the topology-aware ML surrogate developed in the previous chapter within sequential Monte-Carlo simulations. The impact of an improved offshore wind generation modelling on reliability indices will then be assessed.

This chapter is structured as follows. Section 4.1 explores the theoretical

foundations of power systems reliability and adequacy. In section 4.2, the sequential Monte-Carlo algorithm used to carry out adequacy studies is detailed. In particular, the improvement for the modelling of offshore wind generation in the context of adequacy studies is explained. Then, section 4.3 presents the case study, which is based on a simplified version of the Belgian power system in 2030. The impact of an improved modelling of offshore wind farms is assessed, and our methodology is benchmarked against the traditional power curve approach. Finally, conclusions are given in the last section.

4.1. Power System Reliability

The International Energy Agency defines power system reliability in its simplest form as "keeping the lights on". In more technical terms, it refers to the ability of the value chain to deliver electricity to all connected users within acceptable standards and in the amounts desired. In the scientific literature, power system reliability is associated with two fundamental dimensions: **adequacy** and **security** [23].

On the one hand, adequacy represents the ability of the electrical system to satisfy load consumption in the present and over time in steady-state conditions, using existing and new resources [24]. On the other hand, security assesses the ability of a power system to cope with severe and sudden perturbations while maintaining its integrity, i.e., without major service interruptions. Perturbations include non-anticipated loss of generation or network key components, electrical short-circuits, loss of fuel, or rapid changes in demand. This is thus a dynamic approach that is mainly used when talking about real-time operation. Therefore, adequacy and security are two distinct concepts that notably differ from each other with regard to the timescale: adequacy focuses on the long-term behaviour of a system while security relates to the response and integrity right after an unanticipated disturbance. A lack of adequacy leads to load shedding, i.e., *scheduled* power outages designed to prevent the failure of the entire system when the demand strains the generation capacity, while insufficient security can lead to power blackouts. Adequacy studies are traditionally carried out by the TSO and policy-makers in order to evaluate the risk of generation shortage, thus assessing the need for investment in additional production units. **This chapter is focused on adequacy considerations, while security will be covered in the next chapter.**

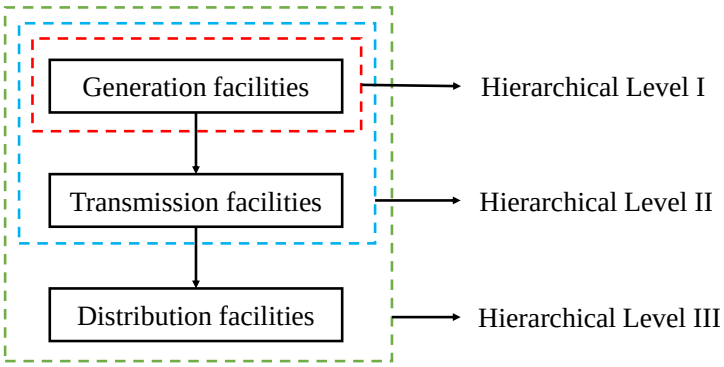

Figure 4.1.: Hierarchical levels for power system reliability assessment.

4.1.1. Hierarchical Levels

Modern electrical systems are highly complex and sometimes cover a large geographical area. They are thus divided into 3 hierarchical levels when their reliability is evaluated [153], as shown in Fig. 4.1. The first hierarchical level (HL-I) is concerned with only the generation facilities and their ability to meet the electricity demand. The second hierarchical level (HL-II) includes both generation and transmission facilities: it assesses the ability of the combined generation-transmission system to deliver electricity to load points, within the limits of the electrical transmission grid. The third hierarchical level (HL-III) includes all three functional zones by also encompassing distribution and its capability to satisfy the energy demand of individual customers. However, HL-III studies are not usually directly carried out on practical large-scale power systems due to the enormity of the problem.

The remaining of this work is limited to the hierarchical level HL-I, as it is the case for many adequacy studies focused on wind generation [146], [154], [155]. Even if it is not in the scope of this thesis, it should be noticed that HL-II assessments are also relevant when considering increased offshore wind generation, as this production is often geographically concentrated in clusters at the coast. There might thus be challenges to deliver the electricity produced at sea by the offshore turbines to the rest of the grid. For example, in Belgium, because of the second offshore zone planned in the North Sea, a reinforcement of the transmission grid is envisioned by the addition of two high voltage lines (Boucle du Hainaut and Ventilus projects) [74].

4.1.2. Towards Numerical Probabilistic Techniques for Adequacy Assessment

Several methods have been developed to assess power systems adequacy, but they can be first divided into two groups: *deterministic* approaches and *probabilistic* methods.

Historically, deterministic techniques were generally used at times when power systems were vertically integrated, i.e., the same company was in charge of producing, transporting and selling the electricity at a single imposed price. The deterministic analysis is based on calculating power system parameters under strictly defined conditions, and computed criteria include [23]:

- Capacity reserve margin: the total installed production capacity must reach the sum of the predicted peak load and a fixed percentage of that load. This criterion thus anticipates an unexpected increase of the load.
- Loss of the largest unit: the power system must be able to meet the load demand even after the loss of the largest production unit.
- Combination of the two above criteria

While appropriate in the past, deterministic approaches for adequacy assessment are not suitable for modern power systems. Indeed, they cannot model generation units using renewable energy sources and they can only consider a limited number of worst case situations. Moreover, the electricity system has been liberalized (unbundling of the electricity sector), international power exchanges have increased, and power systems are required to be as economical as possible, leading to generating units operating closer to their physical limits. Deterministic methods cannot consider random behaviours such as production unit failures and renewable sources variability.

Probabilistic methods, unlike deterministic approaches, allow to consider all possible system states with their associated probabilities, and explicitly encompass random component failures. The risk related to the severity and occurrence of restrictive system states can thus be estimated. This can lead to the development of technically and economically adapted solutions to maintain the electrical system adequacy, by finding the optimal balance between the risk of not always being able to cover the load and the related cost. Therefore, probabilistic techniques are now widely used in the context of power systems reliability [156]. Probabilistic methods can be further divided into two subgroups: *analytical* techniques and *numerical* simulations.

Analytical methods use a mathematical model to represent system states and evaluate reliability indices from the model using mathematical solutions.

Enumeration methods enumerate all possible states of the system and their probability of occurrence, evaluate the reliability of each state, and sum them with their respective weights to obtain reliability indices. Population based methods use optimization tools and evolutionary programming, and they attempt to discover the majority, if not all, of the available states, in order to calculate a good approximation of the reliability indices [157]. Approximate methods use the continuous probability distribution function for formulating an approximate generation system model [158]. For example, the probability convolution combines the probability density functions of the generation system and the load to mathematically evaluate the power system reliability. While analytical methods are fast and exact, they are usually limited to small-scale power systems as the complexity and number of potential system states increase exponentially with the number of system components.

Simulation techniques are used to mimic unpredictable events in power systems, and Monte-Carlo simulations are the preferred method for reliability assessment of large and complex systems [159]. Monte-Carlo simulation methods estimate the reliability indices by simulating the actual process and random behaviour of the system [24], thus treating the problem as a series of random events modifying the system state. Each state is then considered as a snapshot of the system (usually on an hourly basis). Examined random events are failures or maintenance of generation units, as well as load and renewable production variations. Monte-Carlo simulations allow to include numerous system effects without excessive approximation (which would be the case for analytical methods) [153]. For large-scale power systems with numerous elements, the number of possible states can become prohibitive. Analysing all those states is not realistically possible, but the Monte-Carlo approach implements a limited sampling of states. There is thus a compromise between accuracy and the number of samples states. It should be noticed that the required number of samples for a given accuracy level is independent of the size of the system, which is another reason why Monte-Carlo simulations are suitable for large-scale systems. Moreover, they allow to calculate not only reliability indices in the form of expected values of random variables, but also the distributions of these indices. Monte-Carlo methods can be broadly classified into two main types according to the way in which system states are sampled: *non-sequential* Monte-Carlo (random sampling), and *sequential* Monte-Carlo (chronological sampling) simulations.

For non-sequential Monte-Carlo simulations, each system state is randomly sampled and completely independently from previous and subsequent samples. Therefore, in a non-sequential Monte-Carlo assessment, system components are sampled without considering any time dependency between coherent states.

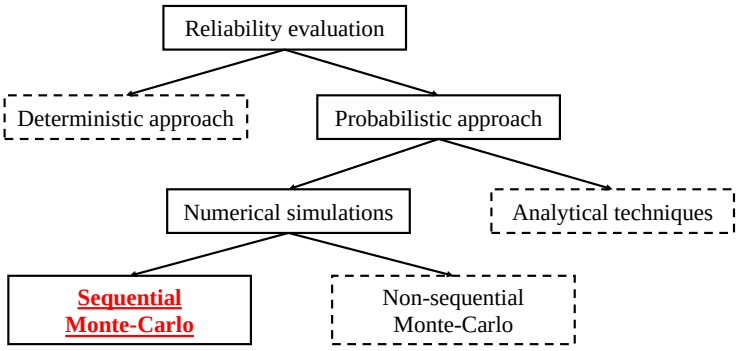

Figure 4.2.: Summary of methods for reliability assessment.

Therefore, with this non-sequential approach, it is not possible to evaluate techno-economic strategies that imply a time coupling, e.g. storage or load shifting. Another source of sequentiality comes from the load (daily, weekly and seasonal cycles) and renewable energy sources. Indeed, time series of renewable generation show characteristics of an auto-correlated signal.

Sequential Monte-Carlo simulations are based on a Markovian approach (a Markov process is a stochastic process describing a sequence of possible events in which the probability of each event depends only on the state attained in the previous event). Therefore, attention is paid to the transition between successive states. Sequential Monte-Carlo simulations typically require higher computational effort than their non-sequential counterparts, but they are more suitable and accurate for modern power systems with a high share of renewable generation. **To carry out our adequacy studies, we will thus use sequential Monte-Carlo simulations**. Fig. 4.2 summarizes the different methods for reliability evaluation, and highlights the one chosen in this work.

4.1.3. Reliability Indices

The adequacy of a given power system is quantified through the computation of **reliability indices**, which measure the frequency, duration, and scale of electricity supply interruptions. Many reliability indicators can be defined to assess adequacy, but two widely used indices will be used in this chapter.

The **Loss Of Load Expectation (LOLE)** [h/year] is defined as the expected yearly number of hours during which the electricity consumption C exceeds the available production P. It can be written as:

$$LOLE = \frac{LOLP}{100} * 8760 \text{ h/year} \tag{4.1}$$

where $LOLP$ is the loss of load probability, defined as the yearly probability that the consumption C is larger than the available generation P:

$$LOLP[\%] = \mathbb{P}(C > P) \tag{4.2}$$

In Belgium, the TSO, Elia, has to comply to a maximum yearly LOLE of **3 hours/year** (and 20 hours/year for the LOLE95, i.e., the LOLE value that has 1 chance in 20 to be encountered). A formal cost-benefit analysis has been applied to derive these reliability standards, based on observations of the decreasing marginal value of adding more capacity beyond a certain level of reliability. Such a cost-benefit analysis depends on the value of lost load, which is a parameter that represents the customer damage from an outage event with a direct monetary value. It is, however, hard to estimate in practice since this value is likely to vary from customer to customer, and it is highly dependent on the timing, frequency and duration of an outage [160].

While widely used by other TSOs, the LOLE does not provide a comprehensive quantification of a power system adequacy. Indeed, it does not allow to quantify the missing power production (or loss load) during periods of scarcity (i.e., when $C > P$). This is why the **Loss Of Energy Expectation (LOEE)** [MWh/year] is introduced: this quantity defines the average energy not served during the year. LOEE is expressed as follows:

$$LOEE = \sum_{i=1}^{M} \int_{P_{g_i}}^{+\infty} F(C)dC * \mathbb{P}(P = P_{g_i}) * 8760 \text{ h/year} \tag{4.3}$$

where $F(C)$ is the cumulative distribution function of the consumption:

$$F(x) = \mathbb{P}(C > x) \tag{4.4}$$

An example of $F(C)$ is shown in Fig. 4.3, where the base load is the minimum level of demand of an electrical grid over a span of time and the peak load is the highest electrical power demand that has occurred in this time period (it is typically characterized as annual, daily or seasonal).

In other words, LOLE allows to quantify the probability of scarcity events, while LOEE measures their severity. These two reliability indices are used in a complementary way to assess power systems adequacy.

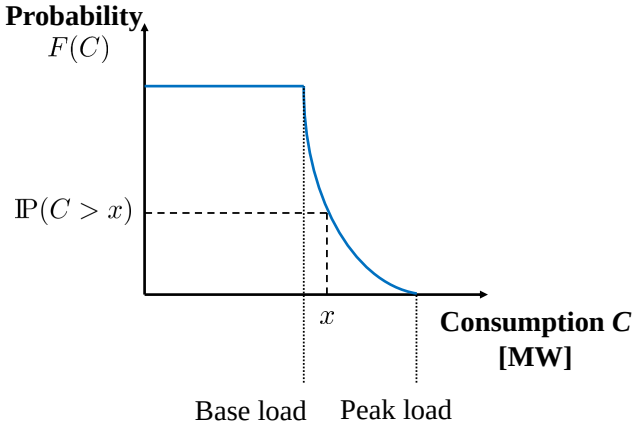

Figure 4.3.: Example of a traditional load cumulative distribution function.

4.2. Sequential Monte-Carlo Simulations for Adequacy Studies

Currently, the more accurate adequacy calculations rely on sequential Monte-Carlo simulations [159]. Indeed, sequential simulations allow the use of detailed hourly generation and load models, which makes them ideally suited to the analysis of intermittent generating sources such as offshore wind generation. Since the Monte-Carlo sampling process is sequential, it models all contingencies and operating characteristics inherent to the power system in a chronological time-consistent way. This is achieved by sampling successive system states while maintaining the time correlation between consecutive steps. The objective is then to compute reliability indices (LOLE and LOEE) on a yearly basis, with an hourly resolution. To that end, time series of wind speed and direction should be generated (and then converted into power using the trained ML models), along with scenarios of load and possible failures of conventional generation units. Each type of time series is further detailed in the next subsections.

4.2.1. Load Modelling

Since the simulations are sequential, a load profile (without load shifting) describing the hourly evolution of electrical consumption throughout an entire year is needed. The load described here refers to the grid load measured on the TSO electrical network, i.e., the aggregated load of all consumers from which the renewable generation at the distribution level is subtracted. This load is highly fluctuating and influenced by more or less foreseeable conditions such as:

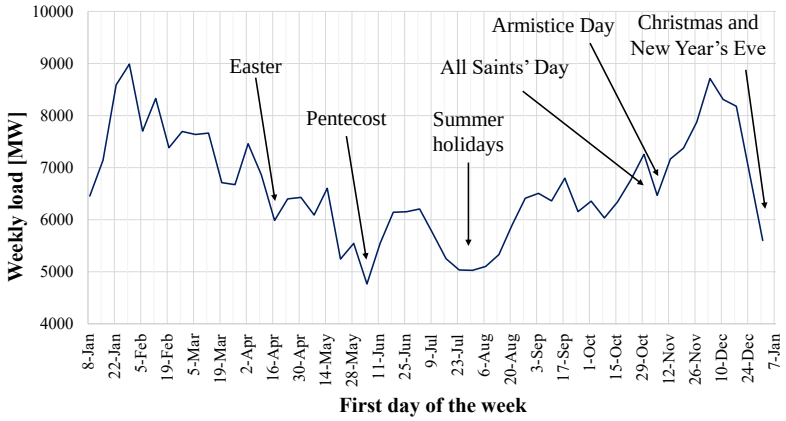

Figure 4.4.: Yearly evolution of the load in Belgium for the year 2023. Summer holidays and several public holidays are highlighted. Data from [10].

- Meteorology: temperature and rain impact heating, while wind and sun variations drive variable generation on the distribution grid.
- Economical activities: there is usually more consumption on working days than during week-end and holidays, and the daily cycle differ as well.
- Pricing incentives: dynamic tariffs such as day/night pricing.
- Rare events: international gathering (e.g., sports events) can cause a sudden peak in load demand.

For example, Fig. 4.4 depicts the yearly evolution of load in Belgium for the year 2023 (data collected on the Elia website). It can be seen that the load tends to decrease during summer while reaching higher values during winter. Moreover, public holidays and summer holidays can be clearly identified by the sudden drops in electrical consumption. On Fig. 4.5, the hourly load evolution for a typical weekday is shown (blue curve): the electrical consumption is reduced during the night, then there is the peak corresponding to people waking up and morning activities. During the afternoon, the load decreases again, before another peak is seen in the evening, when people come home and start cooking and watching television. A typical weekend day is also shown on Fig. 4.5 (grey curve): it can be seen that the load is clearly lower than during a weekday. Time series of load should thus jointly incorporates seasonal trends, diurnal cycles as well as weekday/weekend patterns.

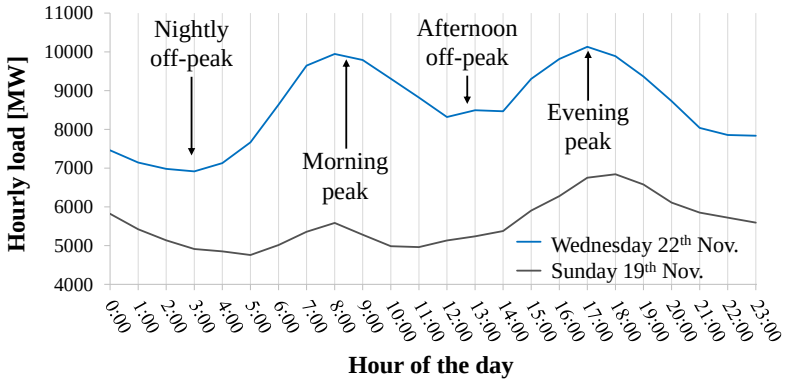

Figure 4.5.: Hourly evolution of the load in Belgium for Wednesday 22^{th} of November 2023 (blue curve) and Sunday 19^{th} of November 2023 (grey curve). Data from [10].

Test systems, available in the literature for the evaluation of adequacy assessment methods, usually combine a peak load and modulation diagrams [161], [162]. While the obtained load profile fully encompasses yearly, weekly, and daily patterns, the same time series is used for all simulated years of the Monte Carlo analysis, unless statistical noise is added. For real-life power systems, if historical data are available, they can be gathered and used to build a load model. The latter can then be leveraged to generate synthetic load profiles, thus allowing to consider the random behaviour of the fluctuating load.

4.2.2. Conventional Units

Conventional power plants (based on natural gas, nuclear, oil but also waste and biomass) can undergo failures inherent to their operation. To account for conventional units outages, the operational cycle of such units is represented through a two-state model, distinguishing between up (operational) and down (non-operational) states. A yearly sequence of up-down-up cycles can be produced by employing a random sampling technique, which draws from the probability distributions of state residence times for each respective state. The Time To Failure (TTF) and Time To Repair (TTR) are typically assumed to be exponentially distributed and can be computed as follows:

$$\begin{aligned} TTF &= -MTTF \ * \ \ln U \\ TTR &= -MTTR \ * \ \ln U' \end{aligned} \tag{4.5}$$

where $MTTF$ is the Mean Time To Failure, $MTTR$ is the Mean Time To Repair, and U and U' are two uniformly distributed random number sequences

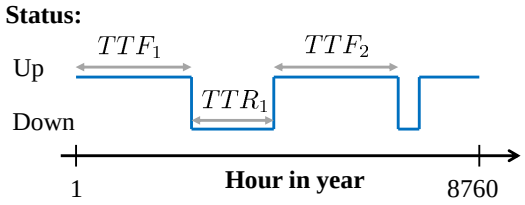

Figure 4.6.: Yearly availability profile of a conventional unit. Modified from [163].

between 0 and 1. The construction of the yearly availability profile of each unit is determined by juxtaposing the status of samples drawn from the TTF and TTR distributions, as shown in Fig. 4.6.

4.2.3. Improved Offshore Wind Generation Modelling

In adequacy studies, offshore wind energy is usually modelled using the traditional power curve approach, thus ignoring intra-farm wake effects. However, those effects clearly influence the expected power output, especially in offshore conditions, and they must not be disregarded. For adequacy studies of modern power systems with a high share of offshore wind generation, the inclusion of complex aerodynamic phenomena in the wind farm modelling is crucial. Moreover, for sequential Monte-Carlo simulations, the wind variability (seasonal trends, daily cycles) should also be considered when generating yearly profiles for offshore wind energy. In this work, the offshore wind generation model is thus composed of three main parts, i.e., the wind model, the Machine Learning surrogate developed in Chapter 3 and the wind turbine availability model. These three parts are described as follows.

Free-flow Wind model

Usually, only a wind speed model is needed for adequacy assessment. However, when taking wake effects into account, the wind direction also has an important influence on the power output of wind turbines. Moreover, when generating wind data, it is important to maintain the correlation between wind speeds and wind directions at different locations. To that end, we use a Vector Auto-Regressive Moving Average (VARMA) model, which augments the ability of ARMA models (that accurately represent time dependencies) with a representation of cross-variables correlations [164].

In ARMA models for wind speed, each value in the simulated time series depends on its own lagged values (AR part) but also on current and various

past values of a stochastic term (MA part). The model is usually referred to as a ARMA(p, q) model where p and q are respectively the order of the auto-regressive and the moving average parts. First, the series y_t is normalized to ensure stationarity, as the hourly wind speed distribution is non stationary due to the daily cycle and seasonality:

$$y_t = \frac{OW_t - \mu_t}{\sigma_t} \tag{4.6}$$

where t is an hour in the year, OW_t is the observed wind speed at hour t, μ_τ is the mean of all observed wind speed at hour t over several years, and σ_t is the standard deviation of all observed wind speed at hour t.

Then, the data series y_t can be used to build the following ARMA(p, q) wind speed time series model [165]:

$$\begin{aligned} y_t = {} & \phi_1 * y_{t-1} + \phi_2 * y_{t-2} + ... + \phi_p * y_{t-p} \\ & + \alpha_t - \theta_1 * \alpha_{t-1} - \theta_2 * \alpha_{t-2} - ... - \theta_q * \alpha_{t-q} \end{aligned} \tag{4.7}$$

where ϕ_i (i = 1, 2, ..., p) and θ_j (j = 1, 2, ..., q) are the auto-regressive and moving average parameters of the model respectively, α_t is a normal white noise process with zero mean and variance σ_a^2, i.e., $\alpha_t \in \text{NID}(0, \sigma_a^2)$ with NID denoting Normally Independently Distributed. The maximum likelihood approach is adopted to estimate the values of ϕ_i, θ_j and σ_a^2. A grid search procedure based on the F-criterion is used to determine the order of the ARMA(p, q) model.

Once the wind speed time series model is established, the simulated wind speed can be calculated as:

$$SW_t = \mu_\tau + \sigma_\tau * y_t \tag{4.8}$$

VARMA(p, q) models for simulating correlated wind speeds and wind directions are just a generalization of ARMA(p, q) models, where the wind speed not only depends on its own lagged values, but also on the lagged values of wind direction. The same goes for the wind direction time series, and the wind vector is written as:

$$\begin{aligned} y_t = {} & \Phi_1 * y_{t-1} + \Phi_2 * y_{t-2} + ... + \Phi_p * y_{t-p} \\ & + \alpha_t - \Theta_1 * \alpha_{t-1} - ... - \Theta_q * \alpha_{t-q} \end{aligned} \tag{4.9}$$

where $y_t = [y_s, y_w]^t$ contains the data series corresponding to wind speed and wind direction and Φ_i and Θ_j are matrices of dimensions [2x2]. The methodology for estimating the parameters and for choosing the (p, q) order is the same as for ARMA models.

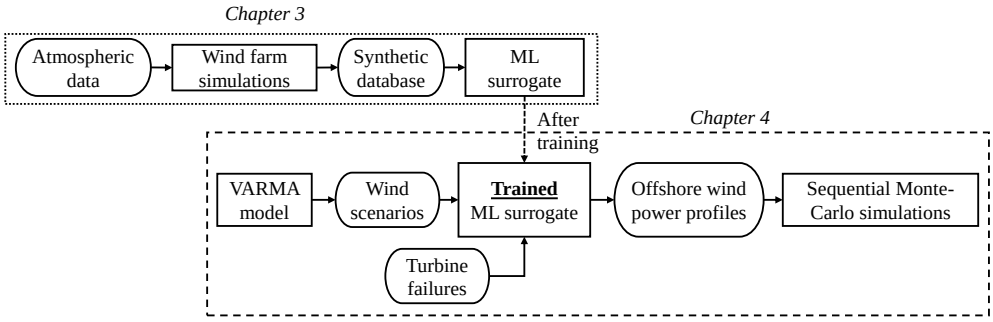

Figure 4.7.: Integration of the developed ML surrogate in the sequential Monte-Carlo framework.

Wind Turbine Availability Model

To account for wind turbine outages, the operational cycle of a wind turbine is represented through a two-state model, similar to the one described in section 4.2.2. For offshore wind turbines, the $MTTF$ is approximately 1298 hours and the $MTTR$ is 34 hours [166]. It should be noted that **turbine failures are fully encompassed by the developed ML surrogate**, which can capture the redistribution of wind due to disabled turbines and the subsequent change in electrical power output.

Wind Turbine Power Surrogate

Wind scenarios are fed to the the ML-based wind farm surrogate developed in Chapter 3, along with turbine availabilities. Offshore wind power profiles are then obtained, fully encompassing the time correlation between consecutive states and power losses due to wake interactions between turbines. The integration of the ML proxy within the sequential Monte-Carlo framework is depicted in Fig. 4.7.

4.2.4. Sequential Monte-Carlo Algorithm

The sequential Monte-Carlo methodology is illustrated in Fig. 4.8. During the initialization, the maximum number of simulated Monte-Carlo years N_{MC} is set. It should be noticed that Monte-Carlo years refer to possible realizations of the physical year for which adequacy is computed (studied time horizon). Then, the procedure for assessing the generation adequacy within a power system is described as follows:

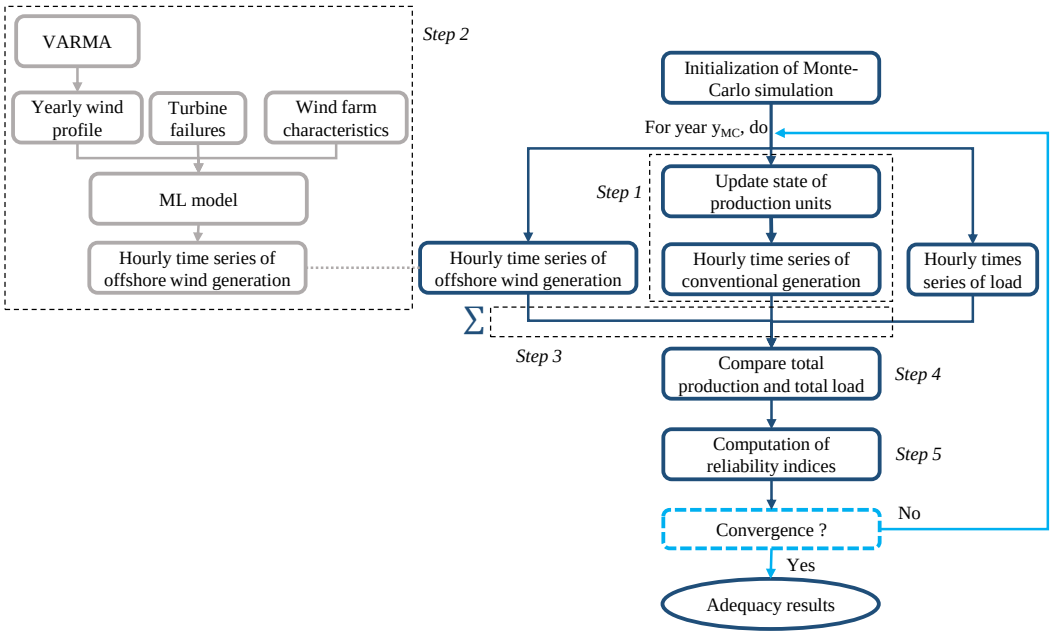

Figure 4.8.: Diagram of the proposed methodology, where the generation of hourly time series of offshore production (using the ML model) is highlighted in grey, while the sequential Monte-Carlo process is given in blue.

1. Create a yearly time series for the availability of conventional generating units using chronological simulations.

2. Generate a yearly time series for the wind power output of every wind farm using the ML proxy and the wind turbine availability model.

3. Compute the total generation capacity of the system (by aggregating conventional and wind powers).

4. Compare the total generation capacity with the load for each state.

5. Compute the yearly reliability indices for the simulated Monte-Carlo year: the number hours when production cannot meet demand i.e., the Loss Of Load (LOL), along with the associated total energy not served, i.e., the Loss Of Energy (LOE).

This process is carried out on a yearly basis (i.e., 8,760 hours), and repeated until a specified degree of confidence has been reached. Once convergence is

achieved, the simulation can be terminated. The stopping criterion used in this work is [25]:

$$\frac{\sigma(X)}{\mathbb{E}(X)} < \epsilon \tag{4.10}$$

where X is a reliability index (LOLE or LOEE), $\mathbb{E}(X)$ is the mean value, $\sigma(X)$ is the standard deviation and ϵ is a convergence threshold, set to 0.005. The mean value and the standard deviation are computed on a set number of years n_{MC} (sliding convergence window). In other words, convergence is achieved when the criteria is met on the last n_{MC} computed years. The purpose of using a stopping criterion (and a maximum number of Monte-Carlo years N_{MC}) is to provide a compromise between the required accuracy and computational cost. At the end of the procedure, final values of LOLE and LOEE are collected and the power system system adequacy is assessed. For Y_{MC} simulated Monte-Carlo years:

$$LOLE = \frac{\sum_{y_{MC}=1}^{Y_{MC}} LOL_{y_{MC}}}{Y_{MC}} \tag{4.11}$$

$$LOEE = \frac{\sum_{y_{MC}=1}^{Y_{MC}} LOE_{y_{MC}}}{Y_{MC}} \tag{4.12}$$

It should be noticed that because of the iterative process of sequential Monte-Carlo simulations, not only expected values of reliability indices are obtained, but also their statistical distribution.

4.3. Case Study

We apply the methodology developed in this paper to a simplified model of the Belgian power system in 2030. Currently, 2.2 GW of offshore wind generation capacity is installed in the Belgian North Sea, in a zone consisting of 9 clustered wind farms. However, aligned with the ambitious objectives of the energy transition, the Belgian government has decided to reach between 5.35 GW to 5.7 GW of offshore capacity by 2030. To that end, a second zone (Princess Elizabeth zone) will encompass 3 parcels, with a total capacity ranging from 3.15 to 3.5 GW. The layout (turbine location, turbine choice, power density) of these future wind farms is still unknown, as the tendering process should begin in late 2024. Therefore, it is important to consider multiple scenarios for this future offshore zone in order to account for the current uncertainty on

the energy that will be provided by the different wind farms. As a reminder, the electrical network is not considered here and is thus simplified using the "copper plate" approach, i.e., there are no constraints to deliver production towards the load consumers.

4.3.1. Data for the Belgian Power System in 2030

Load

Since the simulations are sequential, the load profile describing the hourly evolution of electrical consumption throughout an entire year is needed. This profile jointly incorporates seasonal trends, diurnal cycle as well as weekday/weekend patterns. Historical data of total load gathered from Elia [10] are used to build an ARMA model that captures the yearly load profiles. The peak load is expected to reach 17.72 GW, for an expected yearly consumption of 112.8 TWh.

Solar and onshore wind resources, which are connected to the distribution grid, are aggregated. Historical capacity factors during 2014-2019 in Belgium from [167]–[169] are used, as well as the projected installed capacity, i.e. 14.5 GW for solar and 5.6 GW for onshore wind.

Conventional Units

The installed capacities of the different generation technologies along with their forced outage rates are based on Elia's latest adequacy study [25]. The conventional generation is spread as follows: 2.1 GW nuclear, 7 GW gas, 0.14 GW oil, and 0.97 GW biomass and waste. Specifically, the system consists in 76 large-scale thermal units (i.e., modelled individually by Elia), detailed in Tables 4.1 to 4.6. We assume that by 2030, two nuclear power units (Doel 4 and Tihange 3) are supposed to remain in operation, and two new gas power plants (non-existing today, Seraing with 885 MW, and Flémalle) will be added. Moreover, small distributed conventional units connected on the Elia grid are also considered, but in an aggregated manner. According to Elia, three types of generation are considered: small gas cogeneration units (1600 MW), biomass units (567 MW), and waste units (48 MW). Finally, power plant failures are represented using a probabilistic model similar to the one described in section 4.2.2. Values for $MTTF$ and $MTTR$ are also provided in the tables.

Table 4.1.: Nuclear generation fleet foreseen in Belgium for 2030.

Nuclear power plant	**Capacity [MW]**	**Fuel type**	**MTTF [h]**	**MTTR [h]**
Doel 4	1039	Nuclear	6246	240
Tihange 3	1038	Nuclear	6246	240

Table 4.2.: Diesel generation fleet foreseen in Belgium for 2030.

Turbojet	**Capacity [MW]**	**Fuel type**	**MTTF [h]**	**MTTR [h]**
Aalter	18	Oil	902	98
Beerse	32	Oil	902	98
Cierreux	18	Oil	902	98
Noordschote	18	Oil	902	98
Zedelgem	18	Oil	902	98
Zeebrugge	18	Oil	902	98
Zelzate	18	Oil	902	98

Table 4.3.: Generation fleet of incinerator stations foreseen in Belgium for 2030.

Incinerators	**Capacity [MW]**	**Fuel type**	**MTTF [h]**	**MTTR [h]**
Beveren 2 Indaver	21	Waste	1199	82
Beveren 3 Indaver	24	Waste	1199	82
Beveren Sleco	41	Waste	1199	82
E-wood	22	Waste	1199	82
Intradel	32	Waste	1199	82
ISVAG	12	Waste	1199	82
IVBO	16	Waste	1199	82
Oostende Biostoom	19.4	Waste	1199	82
Oostende Greenpower	20	Waste	1199	82
Schaerbeek 1	15	Waste	1199	82
Schaerbeek 2	15	Waste	1199	82
Schaerbeek 3	15	Waste	1199	82
Thumaide	34	Waste	1199	82
Oostende Biomassa	18	Biomass	1199	82

Table 4.4.: Cogeneration fleet foreseen in Belgium for 2030.

Cogeneration plant	**Capacity [MW]**	**Fuel type**	**Plant type**	**MTTF [h]**	**MTTR [h]**
Aalst GT	43	Gas	CCGT-GT	1735	101
Aalst ST	5	Gas	CCGT-ST	1735	101
Beveren Ineos	25	Gas	OCGT	2250	201
Borealis Kallo	32	Gas	CCGT	1735	101
Euro-Silo	12.9	Gas	CCGT	1735	101
Gent Taminco	6.3	Gas	OCGT	2250	201
Ham GT	39	Gas	CCGT	1735	101
Inesco 1	45	Gas	CCGT-GT	1735	101
Inesco 2	45	Gas	CCGT-GT	1735	101
Izegem	20	Gas	CCGT	1735	101
Jemeppe-sur-Sambre 1	48	Gas	CCGT-GT	1735	101
Jemeppe-sur-Sambre 2	48	Gas	CCGT-GT	1735	101
Jemeppe-sur-Sambre ST	10	Gas	CCGT-ST	1735	101
Lanaken	43	Gas	OCGT	2250	201
Langerbrugge 1	10	Biomass	CL	1199	82
Langerbrugge 2	40	Biomass	CL	1199	82
Lillo Degussa 1	43	Gas	CCGT-GT	1735	101
Lillo Degussa 2	32	Gas	CCGT-GT	1735	101
Lillo Monsanto	43	Gas	OCGT	2250	201
Lillo ST	10	Gas	CCGT-ST	1735	101
Oorderen	43	Gas	OCGT	2250	201
Scheldelaan	140	Gas	CCGT	1735	101
Wilmarsdonk 1	43	Gas	OCGT	2250	201
Wilmarsdonk 2	43	Gas	OCGT	2250	201
Wilmarsdonk 3	43	Gas	OCGT	2250	201
Zandvliet	419	Gas	CCGT	1735	101
Zeebrugge Fluxys	40	Gas	OCGT	2250	201
Zwijndrecht GT	43	Gas	CCGT-GT	1735	101
Zwijndrecht ST	15	Gas	CCGT-ST	1735	101

Table 4.5.: Classical thermal generation fleet foreseen in Belgium for 2030.

Thermal power plant	**Capacity [MW]**	**Fuel type**	**MTTF [h]**	**MTTR [h]**
Knippegroen	305	Gas	1199	82

Table 4.6.: Generation fleet of combined cycle gas turbines foreseen in Belgium for 2030.

CCGT	**Capacity [MW]**	**Fuel type**	**Plant type**	**MTTF [h]**	**MTTR [h]**
Amercoeur 1 GT	289	Gas	CCGT-GT	1735	101
Amercoeur 1 ST	162	Gas	CCGT-ST	1735	101
Angleur 31	25	Gas	OCGT	2250	201
Angleur 32	25	Gas	OCGT	2250	201
Angleur 41	64	Gas	OCGT	2250	201
Angleur 42	64	Gas	OCGT	2250	201
Drogenbos 1	150	Gas	CCGT-GT	1735	101
Drogenbos 2	150	Gas	CCGT-GT	1735	101
Drogenbos ST	160	Gas	CCGT-ST	1735	101
Flémalle	890	Gas	CCGT	1735	101
Ham 31	58	Gas	OCGT	2250	201
Ham 32	58	Gas	OCGT	2250	201
Herdersbrug GT1	157	Gas	CCGT-GT	1735	101
Herdersbrug GT2	156.3	Gas	CCGT-GT	1735	101
Herdersbrug ST	167	Gas	CCGT-ST	1735	101
Inesco	49	Gas	CCGT-ST	1735	101
Marcinelle	413	Gas	CCGT	1735	101
Ringvaart	385	Gas	CCGT	1735	101
Saint-Ghislain	378	Gas	CCGT	1735	101
Seraing	885	Gas	CCGT	1735	101
Seraing 1	150	Gas	CCGT-GT	1735	101
Seraing 2	150	Gas	CCGT-GT	1735	101
T-Power	425	Gas	CCGT	1735	101

Storage

Because sequential Monte-Carlo simulations allow to keep the time dependence between consecutive states, storage can be included in the adequacy assessment. Pumped storage (1.2 GW), aggregated large-scale (1.1 GW) and small-scale (1.02 GW) batteries are considered. Storage is operated in a greedy way, i.e. charging in periods of overproduction, and discharging when there is a shortage of electricity, until energy bounds are reached. This is thus a rule-based operation that does not take economics into account, unlike a price-based optimization.

Imports

Belgium, being a highly interconnected nation, anticipates yearly electricity imports to reach 30 TWh by 2030. Consequently, we impose this annual cap of 30 TWh on imports for each year in our simulations.

Offshore Wind Generation

Scenarios of wind (speed, direction and ambient turbulence) are produced with a VARMA model, as explained in section 4.2.3. Wind data used to build the wind model come from the ERA5 database, presented in section 3.4, at the location of the offshore zone in the Belgian North Sea and for the years 2018 to 2021. For this dataset, the F-criterion leads to a VARMA(3,2) model for the generation of correlated wind speed and wind direction time series. It should be noted that given the proximity of all wind farms, the same wind time series is applied to all of them as free-flow wind. This is rather realistic for farms clustered within the same zone. Moreover, a correlation study performed on ERA5 wind data show that the wind is nearly entirely correlated between the existing cluster and the new Princess Elizabeth area. Since the two offshore wind zones are submitted to the same wind regime, there is no geographical smoothing on the overall electrical production. Wind scenarios are converted to wind power using the ML-based wind farm surrogate developed in Chapter 3.

The turbine coordinates and characteristics for the 9 wind farms located in the first offshore zone are derived from the documentation provided by the Royal Belgian Institute of Natural Science [132]. Their layout is pictured in Fig. 4.9, along with their installed capacity. Turbine power curves can easily be found on the manufacturer website.

Regarding the future offshore wind farms yet to be built in the second zone, different scenarios should be considered, as proposed in preliminary studies

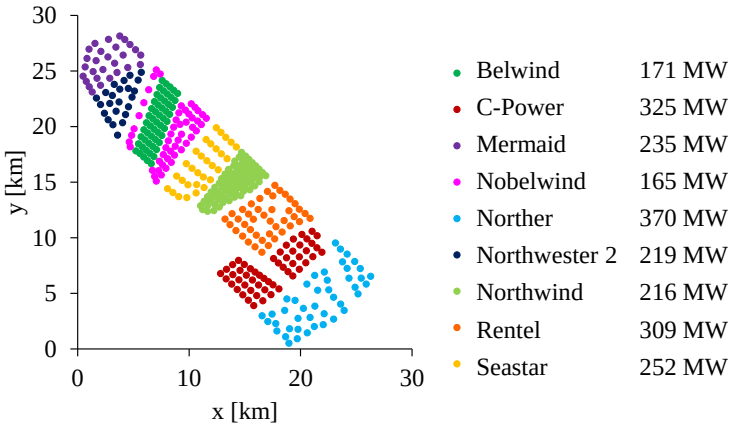

Figure 4.9.: First offshore zone in the Belgian North Sea (already built).

carried out by the Belgian government [170]. Indeed, there is a high uncertainty on how wind farm developers will optimize their installation. Therefore, five different power densities are investigated: 6.2 MW/km^2, 7.5 MW/km^2, 10 MW/km^2, 11.2 MW/km^2, and 12.5 MW/km^2, respectively leading to installed capacities of 1750 MW, 2100 MW, 2800 MW, 3150 MW, and 3500 MW in the second offshore zone. Moreover, different wind turbine technologies are also considered. As the trend in recent offshore wind installations is to invest in larger turbines, the following 3 turbines types are assessed: a 13 MW turbine with a rotor diameter D of 220 m, a 15 MW turbine with D=236 m, and a boosted 17 MW variant of the latter. The location of turbines within the future offshore farms is determined using a simple micro-siting method, complying with inter-turbine distance, environmental and shipping-constraints [171]. Examples of such layouts are presented in Fig. 4.10.

4.3.2. Results

For each sequential Monte-Carlo simulation, besides values of LOLE and LOEE, several outputs can be analysed to assess the power system adequacy. An example of possible results obtained from a Monte-Carlo run is shown in Figs. 4.11 and 4.12: it corresponds to a case where the second offshore zone has an installed capacity of 1.75 GW and turbines with a 13 MW rated power. The distribution of LOL (the number of hours where consumption exceeds production for each Monte-Carlo year) is shown in Fig. 4.11(a). LOLE and LOEE convergence can be seen in Fig. 4.11(b): reliability indices oscillate during the first Monte-Carlo years, before converging after approximately 600 simulated years.

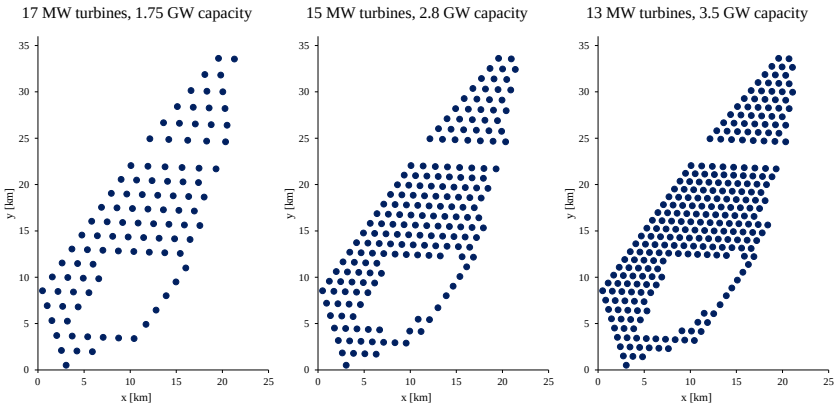

Figure 4.10.: Second (Princess Elizabeth) offshore zone in the Belgian North Sea: examples of possible layouts.

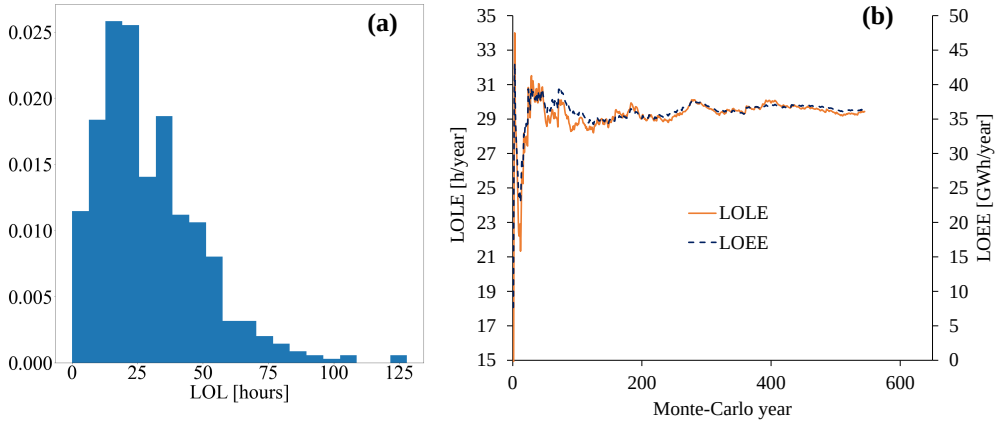

Figure 4.11.: Analysis of reliability indices, (a) Distribution of LOL, (b) Evolution of LOLE and LOEE during Monte-Carlo simulations

A scarcity event is defined as a power shortage, i.e., when the available production is not able to meet the demand. Because sequential Monte-Carlo simulations keep the time correlation between consecutive timesteps, it is possible to quantify the duration and severity of scarcity events (in terms of highest power and total energy not served), as pictured in Fig. 4.12(b). The distribution of durations can be seen in Fig. 4.12(a).

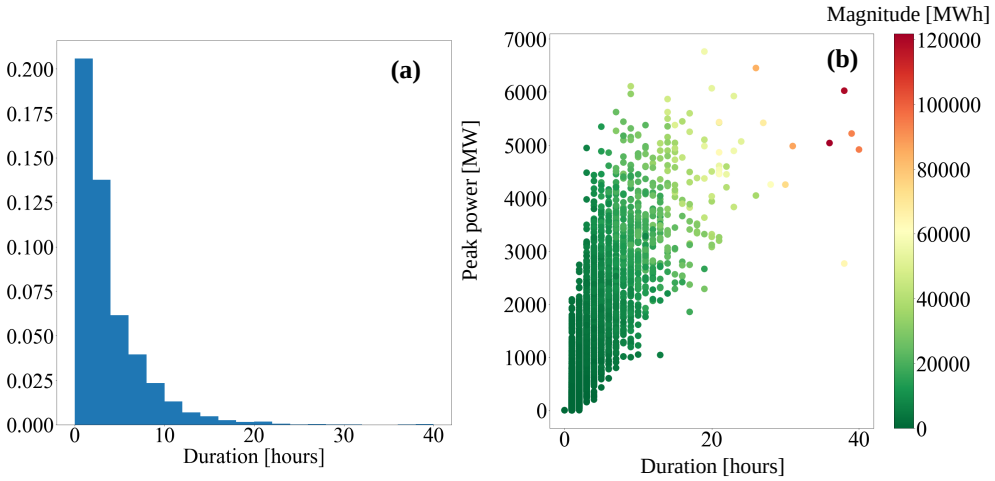

Figure 4.12.: Analysis of scarcity events, (a) Distribution of events duration, (b) Peak power against event duration, with points coloured according to the total energy not served during the event.

Impact of Wake Losses on Adequacy Indices

The offshore wind generation is simulated with both the traditional power curve approach, and the developed topology-aware ML surrogate based on neural networks, i.e., the MLP model whose hyperparameters are specified in section 3.6. All other simulation parameters, e.g. wind speed and wind direction, are the same for both approaches. This allows to quantify the impacts of disregarding wake effects on the annual offshore production, and thus on adequacy indices. Results for four cases (reflecting different capacities of the second offshore zone) are presented in Table 4.7.

First, it can be observed that for each case, the modelling approach for offshore wind power significantly influences LOLE and LOEE values. The relative difference varies from 13% to more than 18%. One can note that increasing the installed capacity (ranging from 1.75 GW to 3.5 GW in the second offshore zone) exacerbates these differences in adequacy indices. Indeed, as the penetration of offshore generation within the power system increases, aerodynamic losses have a higher impact on the yearly offshore production. This can be explained by the fact that, as the power density is higher, the distance between neighbouring turbines is reduced, thereby intensifying wake effects. Moreover, when analysing the two last cases of Table 4.7 (same installed capacity, but different types of turbines), we observe that the difference in LOLE values between the power curve and ML model is approximately 15.5% for 17 MW turbines, while it reaches 19% with 13 MW turbines. Indeed, when

Table 4.7.: Adequacy indices, when offshore generation computed with the ML proxy and power curves.

	LOLE	LOEE	Yearly offshore production
Case 1: 1.75 GW in the 2^{nd} offshore zone, 13 MW turbines			
ML proxy	29.54 h/y	36.43 GWh/y	15.72 TWh
Power curves	26.06 h/y	32.13 GWh/y	17.33 TWh
Difference	3.93 h/y	5.05 GWh/y	-1.72 TWh
	13.29 %	13.85 %	-10.91 %
Case 2: 2.8 GW in the 2^{nd} offshore zone, 13 MW turbines			
ML proxy	25.72 h/y	31.12 GWh/y	19.26 TWh
Power curves	21.63 h/y	26.13 GWh/y	21.94 TWh
Difference	4.27 h/y	5.01 GWh/y	-2.91 TWh
	16.61 %	16.11 %	-15.09 %
Case 3: 3.5 GW in the 2^{nd} offshore zone, 13 MW turbines			
ML proxy	24.42 h/y	30.10 GWh/y	21.33 TWh
Power curves	19.97 h/y	24.53 GWh/y	24.99 TWh
Difference	4.59 h/y	5.92 GWh/y	-3.93 TWh
	18.80 %	19.67 %	-18.40 %
Case 4: 3.5 GW in the 2^{nd} offshore zone, 17 MW turbines			
ML proxy	23.48 h/y	28.40 GWh/y	22.10 TWh
Power curves	19.58 h/y	23.68 GWh/y	25.38 TWh
Difference	3.65 h/y	4.21 GWh/y	-3.15 TWh
	15.55 %	14.84 %	-14.27 %

keeping the same installed capacity, the use of the (larger) 17 MW model reduces the number of wind turbines in the farm. This enables an increase in the spacing between turbine rows, thus mitigating wake losses. Regarding yearly offshore generation, the difference between the power curve and the MLP model ranges between 11% and 18%. This is in line with power losses reported in the literature, where wake effects account for 10 to 20% of the total yearly energy output in large offshore wind farms [49].

Besides studying expected yearly values of reliability indices, it could also be interesting to analyse in more details LOL and LOE values as well as scarcity events for all simulated Monte-Carlo years. Case 3 of Table 4.7, i.e., 3.5 GW in the second offshore zone and 13 MW turbines, is chosen for this more

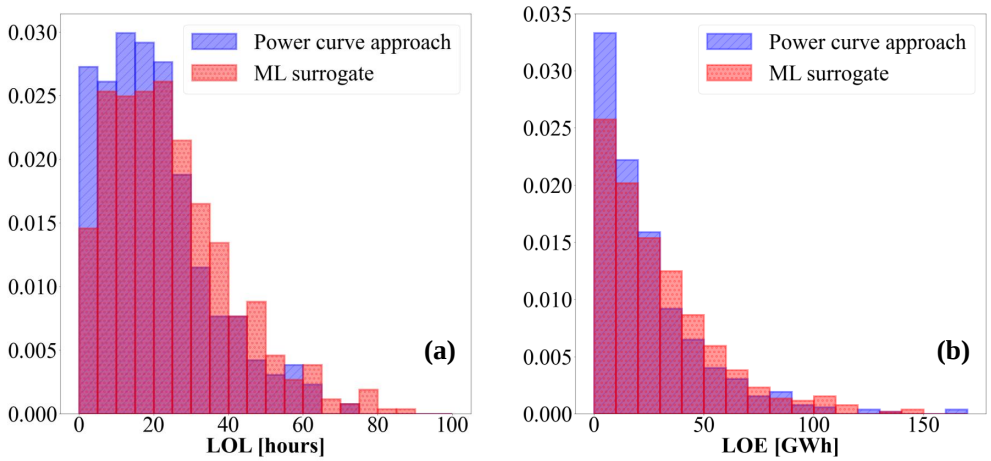

Figure 4.13.: Comparison of the distributions of (a) LOL values, (b) LOE values, when using the ML surrogate and the power curve approach for offshore wind modelling.

thorough analysis. Fig. 4.13(a) shows the distribution of LOL values (number of hours in the year where consumption exceeds production) across all simulated Monte-Carlo years. It can be seen that the distributions differ between the two methods for modelling offshore wind generation. With the power curve approach, the distribution is shifted towards lower values of LOL, since wake effects are ignored and wind power is usually overestimated. With the ML surrogate, the distribution shows a lower density towards small LOL values, and spread over higher values (100 h/year are sometimes reached). The same can be observed for LOE values (energy not served during the Monte-Carlo year), as shown in Fig. 4.13(b). When studying scarcity events in terms of duration, total energy not served, and peak power, it can be observed in Fig. 4.14 that with the ML surrogate for offshore wind modelling, the energy not served can reach up to 140 GWh, while the maximum value with the power curve approach is approximately 120 GWh. Moreover, there is a higher concentration of points towards very severe peak values with the ML surrogate.

These results demonstrate that relying on a more accurate model of offshore wind generation in adequacy studies becomes crucial, especially when the installed offshore capacity increases. In particular, adequacy indices are significantly underestimated when aerodynamic effects are ignored. This could wrongly result in an overly optimistic adequacy assessment, and therefore mislead the subsequent energy policy decisions.

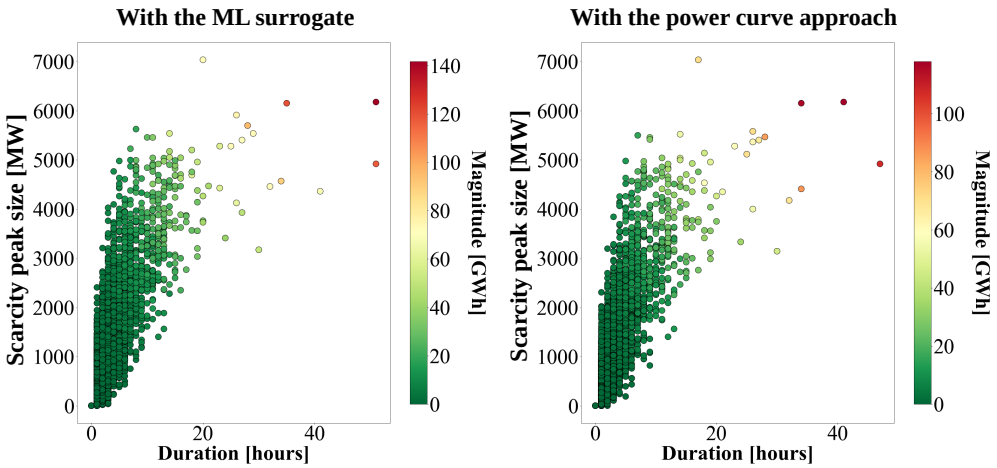

Figure 4.14.: Peak power against scarcity event duration, with points coloured according to the total energy not served during the event, for offshore wind modelled with (a) the ML surrogate, (b) the power curve approach.

Sensitivity to the Power Density within Wind Farms

LOLE and LOEE values, as well as yearly offshore production, are reported in Table 4.8 for each combination of installed capacity and turbine model in the second offshore zone. As expected, when the installed power of offshore farms increases from 1.75 GW to 3.5 GW, the yearly produced energy grows as well. This, in turn, improves reliability indices, leading to a more robust supply of electricity. However, for a given turbine model, this effect becomes less significant as power density increases. For example, for the 13 MW turbine model, values of LOLE decrease from 29.54 to 25.72 hours/year (i.e., -3.82 hours/year) when adding 1.05 GW of wind turbines (by increasing the installed capacity from 1.75 GW to 2.8 GW). But another supplementary 700 MW only reduces the LOLE from 25.72 hours/year to 24.42 hours/year (-1.3 hours/year). These diminishing marginal returns can be explained by the fact that adding more turbines amplifies wake losses. Consequently, wind farm developers should be careful that the extra energy generated does not offset the additional investment costs. The installed capacity should thus result from a well-studied compromise between increasing the yearly offshore production while limiting power losses from wake effects.

Table 4.8.: Adequacy indices, for different wind farm layouts in the second offshore zone (using the ML proxy).

	LOLE	LOEE	Yearly offshore production
Case 1: 1.75 GW in the 2^{nd} offshore zone (6.2 MW/km^2)			
13 MW turbines	29.54 h/y	36.43 GWh/y	15.72 TWh
15 MW turbines	28.73 h/y	35.55 GWh/y	15.92 TWh
17 MW turbines	28.22 h/y	34.30 GWh/y	15.99 TWh
Case 2: 2.1 GW in the 2^{nd} offshore zone (7.5 MW/km^2)			
13 MW turbines	27.42 h/y	33.32 GWh/y	17.05 TWh
15 MW turbines	27.14 h/y	33.19 GWh/y	17.21 TWh
17 MW turbines	26.70 h/y	32.22 GWh/y	17.40 TWh
Case 3: 2.8 GW in the 2^{nd} offshore zone (10 MW/km^2)			
13 MW turbines	25.72 h/y	31.12 GWh/y	19.26 TWh
15 MW turbines	25.04 h/y	30.51 GWh/y	19.68 TWh
17 MW turbines	24.85 h/y	30.54 GWh/y	19.87 TWh
Case 4: 3.15 GW in the 2^{nd} offshore zone (11.2 MW/km^2)			
13 MW turbines	24.44 h/y	29.81 GWh/y	20.30 TWh
15 MW turbines	24.25 h/y	29.41 GWh/y	20.69 TWh
17 MW turbines	24.10 h/y	29.51 GWh/y	20.94 TWh
Case 5: 3.5 GW in the 2^{nd} offshore zone (12.5 MW/km^2)			
13 MW turbines	24.42 h/y	30.10 GWh/y	21.33 TWh
15 MW turbines	24.17 h/y	29.59 GWh/y	21.80 TWh
17 MW turbines	23.48 h/y	28.40 GWh/y	22.10 TWh

Sensitivity to the Choice of Wind Turbines

From Table 4.8, another interesting observation is that the choice of turbine model has a significant impact on adequacy indices. For example, for a 1.75 GW capacity in the second offshore zone, LOLE values are respectively 29.54, 28.73 and 28.22 hours/year for 13, 15, and 17 MW turbines. LOEE values decrease from 36.43 GWh/year to 34.30 GWh/year when the rated power of turbines increases. This difference of 2.13 GWh/year is equivalent to the average yearly consumption of more than six hundred Belgian households. However, the cost of larger turbines is increased, and wind farm operators might choose to install less powerful turbines if the difference in yearly energy does not justify the expense.

4.3.3. Computation Time

As a reminder, since the ML proxy is independent of the wind farm configuration, the training phase is carried out only **once**, and the resulting ML surrogate can be applied for any wind farm layout in the second offshore zone. The whole training process takes approximately 465 minutes (less than 8 hours), including (1) carry out wind farm simulations to build the training database (12 minutes), (2) search for optimal hyperparameters (442 minutes), and (3) train the models (11 minutes). In comparison, the entire training process for the farm-specific models (such as the ones developed in [87]), takes around 157 minutes for a single wind farm. In the proposed case study, training 24 models would have been necessary, resulting in over 62 hours of computational effort. Moreover, exploring an additional layout scenario for the second offshore zone would necessitate developing yet another model, thereby further extending the simulation duration. This clearly shows the advantage of the proposed topology-aware ML surrogate over the conventional approach that consists in building multiple farm-specific models.

Regarding the time needed to carry out Monte-Carlo simulations for each case, the average number of simulated years needed to reach convergence was around 500 to 700 Monte-Carlo years (and each Monte-Carlo year requires a yearly offshore power time series of 8760 samples). For the case 5 in Table 4.8 (3.5 GW in the second offshore zone with 15 MW turbines), one Monte-Carlo simulation would take between 412 and 577 hours with Floris-based simulations, while it only required 13 to 18 hours using the proposed generic ML model. The difference in computation time is huge, especially if one wants to consider several scenarios sensitivities for the future power system.

4.4. Conclusion

In this chapter, the developed ML surrogate is directly integrated within adequacy studies using sequential Monte-Carlo simulations. The fast inference time and topology-aware abilities allow an improved modelling of offshore wind farms without hindering the tractability of the computation process. Wake effects arising within offshore wind farms and leading to significant power losses are fully encompassed with the model, as well as turbine failures.

Results of a test case, based on a simplified model of the Belgian power system in 2030, demonstrate the relevance of an improved modelling of offshore wind generation as it significantly affects adequacy outcomes. Indeed, with a power curve approach (generally used in adequacy studies) that ignores wake losses, we observe a noteworthy underestimation of LOLE and LOEE

values. This error increases with both the installed capacity and power density within the farms, potentially exceeding 18%. This can critically affect adequacy assessments, particularly in a context of increased wind energy integration. Indeed, underestimating reliability indices may conceal adequacy issues, thereby preventing to make the right investments and take the necessary planning actions to ensure a sufficient adequacy of the system.

The generalization abilities allow to account for various possibilities related to future wind farms topology, which is uncertain. Indeed, with the topology-aware ML surrogate, the same model can be used to consider many possible farm configurations, thereby preventing the need to train one model per configuration, as it would be the case with traditional farm-specific surrogates. Outcomes show that increasing power density improves reliability indices, but diminishing marginal returns are observed after a certain point, due to the amplification of wake losses caused by the additional turbines. The installed capacity should thus result from a well-studied compromise between increasing the yearly offshore production while limiting power losses from wake effects. Moreover, the choice of turbine technology also impacts adequacy results, as larger rotor diameters (for the same total farm capacity) decrease LOLE and LOEE values, but at the expense of higher turbine costs.

In the case study, possible configurations for future wind farm layouts were obtained with a simple micro-siting method, complying with inter-turbine spacing and placing turbines in a regular grid. However, this might not be the optimal design, as it does not consider wake effects and dominant wind directions. To address this problem, the developed topology-aware ML surrogate will be integrated within a wind farm layout optimization problem aimed at finding the turbines optimal positions.

Chapter Publications

- **T-H. Nguyen**, J-F. Toubeau, E. De Jaeger and F. Vallée, "Fast and Reliable Modeling of Offshore Wind Generation for Adequacy Studies," *IEEE Transactions on Industry Applications*, vol. 59, no. 6, pp. 7116-7125, 2023
- **T-H. Nguyen**, G. Paternostre, J-F. Toubeau, E. De Jaeger, and F. Vallée, "Adequacy Computations for Power Systems with a High Share of Offshore Wind Generation: Application to Belgium", *2023 EAWE PhD seminar*, Hannover, Germany, 2023
- **T-H. Nguyen**, J-F. Toubeau, E. De Jaeger and F. Vallée, "Adequacy Assessment Using Data-driven Models to Account for Aerodynamic Losses

in Offshore Wind Generation", *Electric Power Systems Research*, vol. 211, 2022

- **T-H. Nguyen**, J-F. Toubeau, E. De Jaeger and F. Vallée, "Machine Learning Proxies Integrating Wake Effects in Offshore Wind Generation for Adequacy Studies," *2021 IEEE International Conference on Environment and Electrical Engineering and 2021 IEEE Industrial and Commercial Power Systems Europe (EEEIC / I&CPS Europe)*, Bari, Italy, 2021

CHAPTER 5.

Wind Farm Layout Optimization With Participation to Secondary Reserve Market

With the sharp increase of renewable energy sources in modern power systems, balancing electrical load and generation throughout the day is becoming a challenge. In case of real-time measured imbalance in the system, the TSO needs to activate reserves in order to restore balance and avoid frequency deviations. In the near future, with a high penetration of weather-dependant electricity generation, intra-hour variability and randomness will become more significant, increasing the need for fast regulation and the value of reserve. Reserve markets, which allow power plant operators to act as Balancing Service Provider (BSP), will be critical for the reliable integration of renewable electricity.

Because offshore wind generation capacity is expected to grow steadily in the future, wind farm operators will have an important role in reserve markets and system balancing. Allowing offshore wind farms to participate in the reserve market will be of mutual interest to TSOs and wind producers. Moreover, it has been proven that variable speed wind turbines in modern wind power plants have intrinsic fast down (virtually at no cost) and ramping up (subject to the availability of wind power) capabilities, which can be effectively used to provide ancillary services [26], [27]. To alleviate frequency deviations, the TSO has several reserve capacities, with different requirements for maximum ramping and activation time. **The focus in this work will be on Automatic Frequency Restoration Reserve (aFRR)**, also called secondary reserve or R2. Indeed, volume needs of secondary reserves are usually higher and are expected to reach even larger values than those for primary reserve in the future [25]. Moreover, primary reserve requires an activation and ramping to full capacity within seconds [172], which might be prohibitive within wind farms, where wind and wake effects take time to propagate. Tertiary reserve is manually activated and is only used to complement and release secondary

reserve (e.g., for very extensive imbalances). It must be able to stay active for a long period of time (hours), which could be a challenge for wind farm operators because of the wind variability. Therefore, secondary reserves seem to be suitable for increasing revenues of wind farms participating to reserve markets [173], [174]. Secondary reserves have a moderately fast response time, are used in both directions to restore a frequency of 50 Hz, and remain active as long as necessary. The TSO activates aFRR automatically by sending a set-point every four seconds and the requested energy is to be activated within 7.5 to 15 minutes in case of selection of the full volume of the aFRR energy bid.

Concerning the participation of wind farms to a Joint day-ahead Energy and Reserve Market (JERM), optimal offering and allocation policies have been investigated, but with the assumption of constant electricity prices [76]. This does not allow to capture the variation of day-ahead and reserve prices with wind speed and wind direction. A combined energy and regulation reserve market model has been developed to encourage wind producers to regulate their short-term outputs [175], but it assumes that marginal revenues of providing day-ahead energy is always higher than the marginal revenues for upward reserve as well as perfect forecasts of market prices. Provision of reserve by wind power units has been considered for generation capacity expansion [176] but simulations were only carried out over 9 representative days of load and generation.

Therefore, the first objective of this chapter is to develop a new formulation for computing the optimal offering, reserve allocation strategy, and subsequent expected profits of a wind farm participating in both day-ahead and secondary upward reserve markets. It will consider the uncertainty in forecasts of wind power, electricity prices and activated reserve volumes. The estimated penalties and balancing costs for failing to provide energy and reserve will also be taken into account.

The remainder of the chapter is structured as follows. Section 5.1 reviews wind farm layout optimization formulations that are available in the literature. Section 5.2 briefly analysis historical data from Belgium of wind speed, wind direction, and electricity prices. In Section 5.3, a general formulation for the computation of revenues from both day-ahead and reserve markets is presented. Section 5.4 details the integration of the new formulation within the wind farm layout optimization problem. In section 5.5, the developed methodology is applied on a real wind farm, using historical data for wind and electricity prices. Yearly profits, supplied energy and AEP of the best optimized layout are compared with regard to the current built configuration

of the test wind farm. Comparisons are also made with more traditional wind farm layout optimization formulations. The study is carried out for the Belgian system using existing market rules. However, although this system has some peculiarities, the main methodology could be applied in other systems with minor modifications. Finally, conclusions are gathered in the last section.

5.1. Literature Review on Wind Farm Layout Optimization

While current wind farms have usually been designed to maximize their power output, future wind farms should be planned and built taking into account the participation to reserve markets. Wind farm layout optimization usually aims at maximizing Annual Energy Production (AEP). It attempts to choose the best placement for turbines, which is equivalent to minimizing wake losses. Indeed, when wind turbines extract mechanical energy from the wind to produce electricity, they cause a reduction of wind speed behind them. Downstream turbines in the wake therefore produce less energy. On a site with specific wind conditions, WFLO will avoid aligning turbines in the directions of dominant wind. Layout optimization for maximizing AEP has been widely studied in the literature, using gradient-based optimization techniques [177]–[179], gradient-free [180]–[182], or comparing both [67]. The idea behind maximizing AEP is that it will maximize profits for wind farm operators selling energy on the Day-Ahead Energy Market (DAEM). However, both objectives might not lead to the same results because of the high volatility of electricity prices. For example, producing much energy in periods of low prices will lead to reduced profits. When considering only day-ahead market, if patterns of low and high prices do not match with wind direction patterns, optimizing AEP is not the same as maximizing profit. Indeed, maximizing profit might lead to higher profits while decreasing supplied energy (and thus turbine loads). WFLO for yearly profit has been studied in previous works [183]–[185], but wind power was sold only on the day-ahead market. Adding participation to reserve market will also impact results if Day-Ahead (DA) and reserve prices do not show the same variations with regard to wind direction.

Therefore, the second objective of this chapter is to use the new formulation for wind power bidding in JERM as the objective function of a wind farm layout optimization maximizing yearly profits. Because computing yearly profits at each iteration step of the optimization is too costly, Stochastic Gradient Descent (SGD) will be used. This prompts the need to make the profit function differentiable. The gradient of the total profit is then estimated

for a limited amount of timesteps. This allows to obtain rather accurate results in a reasonable computation time.

5.2. Analysis of Historical Data

To help better understand the motivations of this chapter, we analyse historical data of wind, electricity prices and activated reserve volume for the year 2023 in Belgium. Data of wind speed and wind direction at the location of the offshore wind farms in the Belgian North Sea have been gathered from the ERA5 database. Electricity prices for the day-ahead market were available on the European Network of Transmission System Operators (ENTSO-E) transparency platform [186]. Prices for reserve capacity and reserve activation, as well as activated upward aFRR reserve volumes were provided by Elia, the Belgian TSO [10].

From Fig. 5.1, we can study the variations of price with regard to wind direction and wind speed, and the mean activated reserve per wind sector. It can be seen in Fig. 5.1(a) that mean day-ahead prices do not follow the same pattern as mean reserve capacity and activation prices with regard to wind direction. Indeed, mean day-ahead prices show a lower mean value for the wind sector centred around 230°. This wind sector corresponds to the direction of dominant wind in this area of the North Sea (direction with most occurrences), as it can be seen in Fig. 5.1(d). This leads to a discrepancy between maximizing profits and energy production. Indeed, when prices are not considered, WFLO will try to avoid aligning turbines in the dominant wind direction. However, since prices tend to be lower in that wind section, it might be more profitable to avoid wake losses in other directions, where prices are higher. Mean reserve capacity prices, on the other hand, tend to be higher in that wind direction sector, while reserve activation prices do not show a significant increase or decrease. This means that accounting for participation to reserve will affect the optimization results, as day-ahead and reserve prices have different patterns with regard to wind direction. Fig. 5.1(c) shows the volumes of activated reserve normalized by the maximum activated volume for aFRR upward reserve (117 MW in 2023). We can see that mean activated volumes tend to be lower in the direction of dominant wind. Another interesting analysis can be made in Fig. 5.1(b), which displays the mean electricity prices with regard to wind speed. One can see that day-ahead prices tend to decrease with higher wind speeds, while it is the opposite for reserve capacity prices. One reason that explains this reduction of day-ahead price with increasing wind speed is the high penetration of offshore wind generation in the Belgian power system (10% of yearly consumption produced by offshore wind farms). Because wind energy

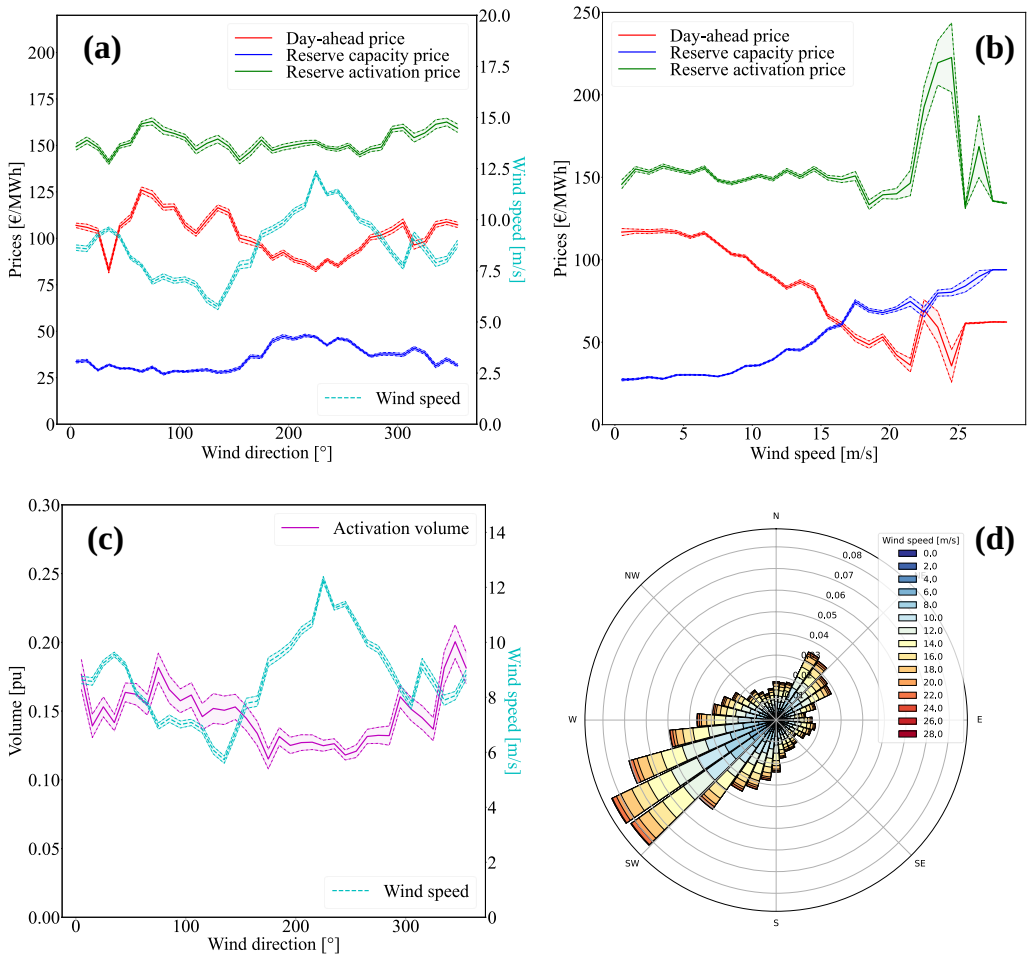

Figure 5.1.: Mean electricity prices with regard to (a) wind direction and (b) wind speed in 2023. (c) Mean normalized activated volumes of reserve with regard to wind direction. (d) Wind rose at the location of Belgian offshore wind farms for 2023, from ERA5 data (latitude: 51.5°N, longitude: 2.75°E).

has lower production costs than conventional thermal power plants, a high production of electricity through wind turbines can lead to lower prices in the day-ahead market. This highlights the relevance of the development of low wind turbines (described in section 2.5.2), which are designed to capture more energy at low wind speeds. Reserve activation prices remain constant until approximately 20 m/s, but show a sharp increase around 25 m/s, which is the cut-off wind speed of most Belgian offshore wind turbines. This is the limit at which turbines are shut down to prevent mechanical damage, and the farm

output goes from rated power to 0. Therefore, a small prediction error in wind speed can lead to a tremendous need of reserve.

5.3. Optimal Joint Participation to Day-Ahead and Reserve Markets of Offshore Wind Farm

One day before real-time delivery (market closure is at noon), for each timestep t of the 24 hours of the next day k, a wind farm operator:

- forecasts available wind power $\hat{P}_{k,t}^{wind,\,avail}$
- decides the total amount of power sold to both day-ahead and reserve markets $P_{k,t}^{c}$
- decides the amount of reserve capacity to procure to the reserve market $R_{k,t} = \alpha_{k,t} * P_{k,t}^{c}$
- computes the power to be sold in the day-ahead energy market $P_{k,t}^{DA} = P_{k,t}^{c} - \hat{R}_{k,t}$

The wind farm reserve capacity represents the amount of power that the wind farm holds back from electricity production, to sell in the reserve market instead of the day-ahead energy market. Based on weather forecasts (and thus wind power forecasts), a wind farm operator bids its electricity production in the day-ahead market and the reserve capacity in the secondary reserve market. On the day of delivery, the wind farm must be able to supply both the day-ahead and activated reserve quantities. In this work, it is assumed that wind farms always prioritize providing reserve (as the wind farm is contractually bound to make the reserve capacity available).

The accuracy of weather and thus wind power forecasts is crucial in order to make relevant bids in both markets: underestimation leads to lower bids and decreased profits, while overestimating production results in inability to supply contracted bids, thus incurring financial penalties. Moreover, electricity prices can be highly volatile, and the actual activation of reserve depends on the system imbalance, which is also fluctuating. Forecast errors on electricity prices and activation volume can lead to a wrong estimation of expected profit. In this work, we assume that forecast errors follow a gaussian distribution with a given mean and standard deviation. For each considered timestep, S forecast errors are randomly sampled using a Monte-Carlo approach.

5.3.1. Wind Power Forecasts

The forecast of available wind power $\hat{P}_{k,t}^{wind,\,avail}$ depends on (previously) forecasted free-flow wind speed $\hat{u}_{k,t}^{\infty}$ and wind direction $\hat{\theta}_{k,t}$.

$$\hat{P}_{k,t,s}^{wind,\,avail} = f(\hat{u}_{k,t,s}^{\infty}, \hat{\theta}_{k,t,s})$$

The index s denotes the Monte Carlo sample number related to forecast error sampling. The operator $f(\cdot)$ indicates the conversion of wind data to wind power: it is based on the wind turbines power curve and should account for wake effects arising within the wind farm.

The forecasted wind speed $\hat{u}_{k,t}^{\infty}$ is derived from the actual realization of wind speed (normally not known by the wind farm operator) and a forecast error sampled from a normal distribution.

$$\begin{aligned} \hat{u}_{k,t,s}^{\infty} &= u_{k,t}^{\infty} + \epsilon_{k,t,s}^{u} \\ \epsilon_{k,t,s}^{u} &\sim N(0, \sigma^{u}) \end{aligned} \tag{5.1}$$

The same process is used to forecast wind direction

$$\begin{aligned} \hat{\theta}_{k,t,s}^{\infty} &= \theta_{k,t}^{\infty} + \epsilon_{k,t,s}^{\theta} \\ \epsilon_{k,t,s}^{\theta} &\sim N(0, \sigma^{\theta}) \end{aligned} \tag{5.2}$$

Therefore, forecasts of available wind power can be written as:

$$\hat{P}_{k,t,s}^{avail} = f_P(u_{k,t}^{\infty} + \epsilon_{k,t,s}^{u}, \theta_{k,t}^{\infty} + \epsilon_{k,t,s}^{\theta}) + \epsilon_{k,t,s}^{f_P} \tag{5.3}$$

$\epsilon_{k,t,s}^{f_P}$ is the modelling error associated with the wind farm model. For wind speed forecasting, literature shows that forecast errors follow a gaussian distribution with a mean value of 0 and a standard deviation approximately equal to 15% [187]. For wind direction, day-ahead forecasts show a root mean squared error of 4.2 ° [188].

5.3.2. Day-ahead Market

The day-ahead energy market is a financial market where participants purchase and sell electrical energy at financially binding day-ahead prices for the following day. Electricity is traded at 12h00 for the 24 hours of the next day and the market is cleared based on an auction mechanism, where market price and volume is the intersection point between the demand and supply curves. After the auctions on day-ahead markets are closed, existing shortfalls or surpluses

can still be evened out through intra-day trading. However, intra-day market is not considered in this work, as prices are extremely volatile and tend to have similar patterns than imbalance fees. Indeed, market participants are charged with imbalance fees every time they deviate from their nominations. These fees, set on a quarter-hourly basis, aim at ensuring that participants contribute efficiently at balancing the electrical system and reflect the cost related to the activation of reserves by the TSO. Revenues from the day-ahead market for timestep t of day k can be written as (assuming perfect forecasts):

$$\text{Profit}_{k,t}^{DA} = P_{k,t}^{DA} * \lambda_{k,t}^{DA} - \Delta P_{k,t}^{DA} * \lambda_{k,t}^{imb} \tag{5.4}$$

where $\lambda_{k,t}^{DA}$ is the day-ahead price, $\Delta P_{k,t}^{DA}$ is the contracted power not supplied, and $\lambda_{k,t}^{imb}$ is the imbalance fee.

Day-ahead prices and imbalance penalties need to be forecasted by the wind farm operator before making a bid on the market. For the gaussian distribution parameters of day-ahead electricity prices, μ is approximately 0 and σ is around 7% [189].

5.3.3. Reserve Market for aFRR

Upward regulation is activated in case of negative imbalance in the system (frequency deviation because consumption exceeds production), and downward regulation is used for positive imbalance. In this work, we only consider the provision of upward reserve regulation since wind farms are not able to benefit from fuel-saving returns in downward regulation [190]. Indeed, activation of downward reserves can yield both positive (the TSO pays the BSP) and negative prices (the BSP pays the TSO) [191]. Negative prices result from producers (e.g., gas-fired power plants) willing to lower their output since their energy is already sold in long-term markets and they can save operating costs: they are usually willing to pay the TSO a small amount. However, when facing scarcity of downward flexibility, BSP may bid positive activation prices, i.e. being paid for the service, which is the only case where providing downward reserve would be profitable for wind farm operators. It should be noted that this assumption strongly depends on market conditions, but it is suitable for the Belgian case study considered in this work. Therefore, **we will only focus on upward reserve**.

Revenues from the aFRR upward market are twofold. BSPs earn revenues from the procurement of reserve capacity (through capacity bids), and balancing revenues from the real-time activation of procured reserves. The reserve capacity price $\lambda^{R,c}$ is determined through a pay-as-bid process. We assume that because

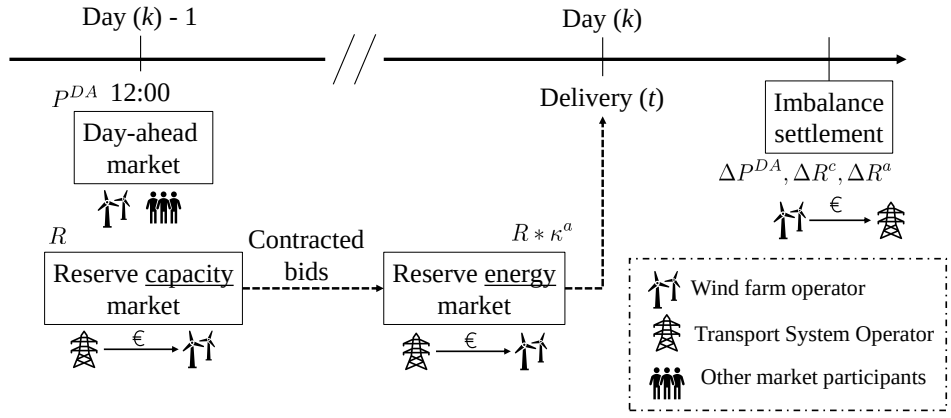

Figure 5.2.: Bidding process of an offshore wind farm operator participating in both day-ahead and reserve markets.

of the lower production costs for wind generation than conventional power plants, capacity bids from wind farm will be well placed in the merit order and will be chosen first by the TSO. The reserve activation price $\lambda^{R,a}$ is pay-as-cleared and contracted aFRR energy bids for possible activation on day k have to be submitted by the BSP to the TSO at the latest in day-ahead (day k-1). The TSO may activate partially or entirely aFRR energy bids, depending on the negative system imbalance. This process is presented in Fig. 5.2. The uncertainty in the balancing actions (i.e., the total amount of activated upward reserve) is modelled through scenarios of reserve activation $\kappa^a \in [0, 1]$. Moreover, in case of several market players bidding in the balancing market, we assume an equal distribution of reserve among all market participants.

Failing to provide the activated reserve requested by the TSO leads to activation penalties that are calculated as follows [192]:

$$\text{Penalties}_{k,t}^{R,a} = \gamma^a * \frac{\Delta R_{k,t}^a}{R_{requested}} * (\text{Capacity remuneration} + \text{Activation remuneration}) \tag{5.5}$$

where γ^a is a penalty multiplier for failing to provide activated reserve. It is set by the TSO and in Belgium, Elia has chosen a value of 1.3 for γ^a. The reserve discrepancy during activation (contracted reserved not supplied when requested), $\Delta R_{k,t}^a$, is defined as:

$$\begin{aligned} \Delta R_{k,t}^a &= R_{requested} - R_{supplied} \\ \Delta R_{k,t}^a &= R_{k,t} * \kappa_{k,t} - \min(R_{k,t} * \kappa_{k,t}, \hat{P}_{k,t}^{wind,\, avail}) \end{aligned} \tag{5.6}$$

In our problem, this translates to this equation:

$$\begin{aligned} \text{Penalties}_{k,t}^{R,a} &= 1.3 * \frac{\Delta R_{k,t}^{a}}{R_{k,t} * \kappa_{k,t}^{a}} * (R_{k,t} * \lambda_{k,t}^{R,c} + R_{k,t} * \lambda_{k,t}^{R,a} * \kappa_{k,t}^{a}) \\ \text{Penalties}_{k,t}^{R,a} &= 1.3 * \frac{\Delta R_{k,t}^{a}}{\kappa_{k,t}^{a}} * (\lambda_{k,t}^{R,c} + \lambda_{k,t}^{R,a} * \kappa_{k,t}^{a}) \end{aligned} \tag{5.7}$$

Moreover, Elia controls the availability of the aFRR capacity by performing availability tests. Elia has the right to perform at maximum 12 availability tests on a rolling window of 12 months and each test lasts 3 quarters of an hour. In case of a failed availability test, the BSP must pay financial penalties.

$$\text{Penalties}_{k,t}^{R,c} = \gamma^{c} * \Delta R_{k,t}^{c} * \lambda_{k,t}^{R,c} \tag{5.8}$$

$\Delta R_{k,t}^{c}$ is the missing reserve capacity during the availability test and γ^{c} is the penalty factor, equal to 0.75 by default. However, in case the penalty concerns a second consecutive failed availability test, γ^{c} is equal to 1.5. But more importantly, Elia hinders the possibility of participating to reserve markets by adapting the upper limit of aFRR capacity bids in case of two or more failed consecutive availability tests of the same aFRR capacity product. To account for this technical penalty, we should set a very high penalty price when available power for activation in real-time is lower than reserve capacity bids. This allows to account for this technical constraint in the profit formulation. Therefore, we set γ^{c} to 10.

For a timestep k, t where a wind farm decides to participate to the reserve market, revenues from reserve are computed as follows:

$$\begin{aligned} \text{Profit}_{k,t}^{reserve} = &(R_{k,t} * \lambda_{k,t}^{R,c} + R_{k,t} * \lambda_{k,t}^{R,a} * \kappa_{k,t}^{a}) \\ &- \left(1.3 * \frac{\Delta R_{k,t}^{a}}{\kappa_{k,t}^{a}} * (\lambda_{k,t}^{R,c} + \lambda_{k,t}^{R,a} * \kappa_{k,t}^{a}) + \gamma^{c} * \Delta R_{k,t}^{c} * \lambda_{k,t}^{R,c}\right) \end{aligned} \tag{5.9}$$

Reserve and regulation prices are characterized by higher volatility, lower mean, more frequent price spikes and a more skewed distribution compared to electric energy prices, thus modelling their behaviour is potentially more challenging [193].

5.3.4. Profit Computation

To summarize, revenues from the participation of both day-ahead and reserve markets over T timesteps of K days can be written as:

$$\begin{aligned}\text{Profit} = \sum_{k}^{K}\sum_{t}^{T} \mathbb{E}_s \big[& (P^{DA}_{k,t} * \hat{\lambda}^{DA}_{k,t,s}) \\ & + (R_{k,t} * \hat{\lambda}^{R,c}_{k,t,s}) \\ & + (R_{k,t} * \hat{\lambda}^{R,a}_{k,t,s} * \hat{\kappa}^{a}_{k,t,s}) \\ & - (\Delta P^{DA}_{k,t,s} * \hat{\lambda}^{imb}_{k,t,s}) \\ & - (1.3 * \frac{\Delta R^{a}_{k,t,s}}{\hat{\kappa}^{a}_{k,t,s}} * (\hat{\lambda}^{R,c}_{k,t,s} + \hat{\lambda}^{R,a}_{k,t,s} * \hat{\kappa}^{a}_{k,t})) \\ & - (\gamma^{c} * \Delta R^{c}_{k,t} * \hat{\lambda}^{R,c}_{k,t,s}) \big]\end{aligned} \tag{5.10}$$

The first line of Eq. (5.10) represents the revenues from the day-ahead energy market, the second line is the revenues stemming from the procurement of reserve capacity, the third line is the profits earned for the real-time activation of reserves, the fourth line is the imbalance fees when deviating from day-ahead market nominations, the fifth line is the penalties for failing to provide the activated reserve requested by the TSO, and the last line represents the penalties related to the reserve capacity availability tests.

For each timestep t of day k, an inner optimization problem gives the optimized total power contracted to the market (day-ahead and reserve), and the percentage of power allocated for reserve.

$$\begin{aligned}\underset{\alpha_{k,t},\beta_{k,t}}{Max} \quad \mathbb{E}_s \big[& (P^{DA}_{k,t} * \hat{\lambda}^{DA}_{k,t,s}) \\ & + (R_{k,t} * \hat{\lambda}^{R,c}_{k,t,s}) \\ & + (R_{k,t} * \hat{\lambda}^{R,a}_{k,t,s} * \hat{\kappa}^{a}_{k,t,s}) \\ & - (\Delta P^{DA}_{k,t,s} * \hat{\lambda}^{imb}_{k,t,s}) \\ & - (1.3 * \frac{\Delta R^{a}_{k,t,s}}{\hat{\kappa}^{a}_{k,t,s}} * (\hat{\lambda}^{R,c}_{k,t,s} + \hat{\lambda}^{R,a}_{k,t,s} * \hat{\kappa}^{a}_{k,t,s})) \\ & - (\gamma^{c} * \Delta R^{c}_{k,t,s} * \hat{\lambda}^{R,c}_{k,t,s}) \big]\end{aligned} \tag{5.11}$$

with:

$$\begin{aligned} P_{k,t}^{DA} &= (1-\alpha_{k,t}) * \beta_{k,t} * P^{farm,rated} \\ R_{k,t} &= \alpha_{k,t} * \beta_{k,t} * P^{farm,rated} \\ 0 \leq &\alpha_{k,t} \leq 1 \ \forall k,t \\ 0 \leq &\beta_{k,t} \leq 1 \ \forall k,t \end{aligned} \tag{5.12}$$

$$R_{k,t} \in [0, R_{max}] \tag{5.13}$$

The agreed upon power schedules, $P_{k,t}^{\mathrm{DA}}$ and $R_{k,t}$ are the true design variables in this problem. The total contracted power in reserve and day-ahead markets cannot exceed the wind farm installed capacity, which is translated with constraints (5.12). Moreover, reserve bids are limited to a maximum value R_{max}, ensured by constraint (5.13). Indeed, according to Elia rules for BSP participating to aFRR markets, each bid should not exceed 50 MW per delivery point. Furthermore, aFRR requirements for the Belgian power system was 117 MW in 2023 (total power contracted by Elia with BSPs), which sets an absolute value as well. For each timestep, the wind farm operator chooses to contract $P_{k,t}^{c}$, the total contracted power, to the JERM. This quantity is optimized through the $\beta_{k,t}$ variable. The allocation of this contracted power to the day-ahead and reserve markets is then given with $\alpha_{k,t}$. As a reminder, in case of missing power (available power lower than power contracted in the JERM, i.e. $\Delta P_{k,t,s}^{DA}$ and/or $\Delta R_{k,t,s}^{a} \geq 0$), the supply of activated reserve will always be prioritized, regardless of imbalance prices.

This optimal allocation of day-ahead and reserve power is similar to the flexible stochastic formulation available in the literature [76]. This approach is characterized by its total freedom to choose the energy and reserve share in each stage of the problem; i.e. the wind farm can take advantage of the intermediate information about wind power production, thereby reducing the penalties at the balancing stage. This means that the operator can adjust the share of energy and reserve in the balancing stage in line with the expected power production in each scenario s. Optimal values of $\alpha_{k,t}$ and $\beta_{k,t}$ can be found with a combinatorial exploration (since their range is limited and the granularity does not have to be very high, as power bids are submitted by steps of 1 MW).

5.4. Formulation of the Wind Farm Layout Optimization Problem

Taking into account uncertainty on wind (thus wind power) and price forecasts, we can write the optimization problem:

$$\begin{aligned} \underset{\boldsymbol{x},\boldsymbol{y}}{Max} \quad & \sum_{k}^{K}\sum_{t}^{T} \mathbb{E}_s \left[\left(P_{k,t}^{DA} * \hat{\lambda}_{k,t,s}^{DA}\right) \right. \\ & - \left(\Delta P_{k,t,s}^{DA} * \hat{\lambda}_{k,t,s}^{imb}\right) \\ & + \left(R_{k,t} * \hat{\lambda}_{k,t,s}^{R,c} + R_{k,t} * \hat{\lambda}_{k,t,s}^{R,a} * \hat{\kappa}_{k,t,s}^{a}\right) \\ & - \left(1.3 * \frac{\Delta R_{k,t,s}^{a}}{\hat{\kappa}_{k,t,s}^{a}} * \left(\hat{\lambda}_{k,t,s}^{R,c} + \hat{\lambda}_{k,t,s}^{R,a} * \hat{\kappa}_{k,t,s}^{a}\right)\right) \\ & \left. - \left(\gamma^{c} * \Delta R_{k,t,s}^{c} * \hat{\lambda}_{k,t,s}^{R,c}\right) \right] \end{aligned} \tag{5.14}$$

subject to

$$\sqrt{\left(x_i - x_j\right)^2 + \left(y_i - y_j\right)^2} \leq \ d_{min} \ \forall \ i, j > i \tag{5.15}$$

$$\begin{aligned} & x^l \leq x_i \leq x^u \ \forall i \\ & y^l \leq y_i \leq y^u \ \forall i \end{aligned} \tag{5.16}$$

The design variables are $\boldsymbol{x}$ and $\boldsymbol{y}$, the vectors of x- and y-coordinates of wind turbines. Constraint (5.15) ensures a minimum spacing d_{min} between adjacent turbines while (5.16) keeps turbines from being outside the farm boundaries ($[x^l$-$x^u]$, $[y^l$-$y^u]$). The objective function aims at maximizing the total profit over T timesteps of K days. The total power contracted in the JERM, the allocation of reserve and the distribution of potential missing power is determined from Eq.(5.11).

The complete methodology is summarized in Fig. 5.3. The ML surrogate based on neural networks (MLP) developed in Chapter 3 is used for wind power conversion: it is especially appropriate for a wind farm layout optimization problem. Indeed, at each optimization step, turbines are moved within the farm boundaries until convergence is reached for the optimal positioning. Therefore, a different layout is seen at each iteration, justifying the need for a topology-aware model, applicable to any wind farm configuration. Moreover, as the optimizer will aim at placing turbines to minimize power losses due to wakes,

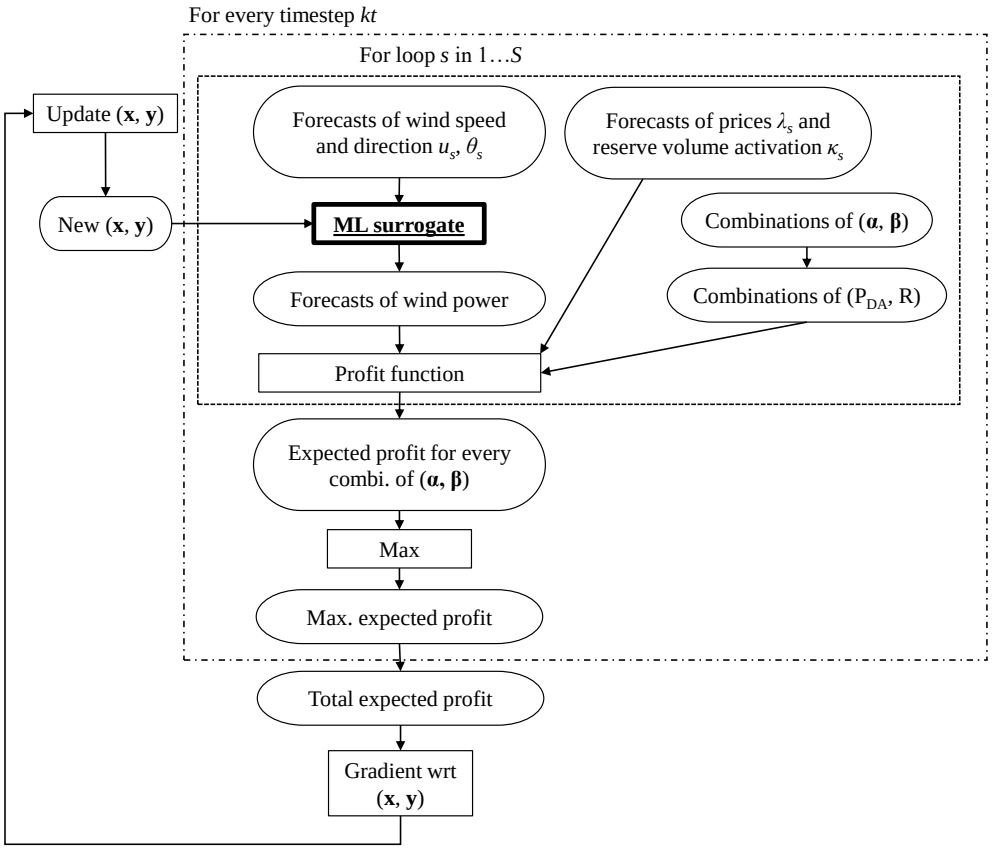

Figure 5.3.: Methodology for layout optimization accounting for reserve participation.

accurately modelling wake losses is crucial as it will directly influence the optimized solution.

The optimization is carried out using Stochastic Gradient Descent (SGD), which is an iterative method for optimizing a differentiable objective function. It replaces the actual gradient (calculated from the entire data set) by an estimate (calculated from a randomly selected subset of the data). Therefore, the algorithm follows the mean gradient by a specified distance, which is equivalent to optimizing the expected value of the objective function [177]. This reduces the very high computational burden in high-dimensional optimization problems, achieving faster iterations but at the cost of a lower convergence rate. The search path of the stochastic gradient method is compared with the standard gradient descent in Fig. 5.4. The deterministic constraints of Eq.(5.16) and (5.15) are implemented within the stochastic gradient descent by aggregating them to a penalty term with units that are consistent with the objective [177].

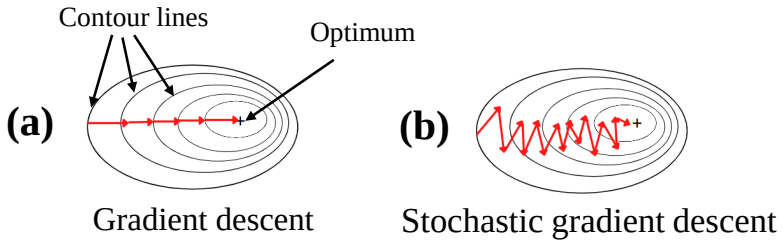

Figure 5.4.: Illustration of search paths of (a) the gradient descent and (b) the stochastic gradient methods on a 2D plane.

The penalty term is designed so that, initially, the penalty gradients are of similar magnitude to the profits gradients and so that the penalty gradients overwhelm the profits gradients as the optimization continues.

Because computing the total profit for a year (365 days * 96 quarters of an hour, i.e., 35,040 timesteps) at each iteration would bee too costly, SGD is particularly relevant for our proposed WFLO formulation. However, an important condition for using SGD is that the objective function needs to be differentiable, since SGD is a gradient-based method. As a reminder, neural networks (MLP) are the method used to build the ML surrogate. When making predictions, input features are fed to the first hidden layer of the network, where neurons are activated and propagate the signal through all the hidden layers along the synapses to the output layer. Since the propagation only involves weighted sums, and the activation function (ReLU was chosen) can be made differentiable (as explained in section 3.5.2, we just need to define a value for the derivative at the origin), MLP neural networks can be directly integrated within gradient methods. Moreover, the inner optimization for the optimal bidding strategy in the JERM, defined by Eq.(5.11), is solved through a combinatorial exploration, which makes it differentiable and thus compatible with the SGD algorithm.

5.5. Case Study

We use data from Northwind, a Belgian offshore wind farm situated 38 km from the coast in the North Sea, within the first Belgian offshore cluster. Northwind consists of 72 Vestas turbines, for a total installed capacity of 216 MW. Each turbine has a rotor diameter of 112 m, a hub height of 71 m, and the rated power is 3.075 MW. The layout of this wind farm can be seen in Fig. 5.5. Northwind was built in 2014, when provision of reserve by offshore wind farms was not even discussed. The layout is quite regular, with turbines aligned on

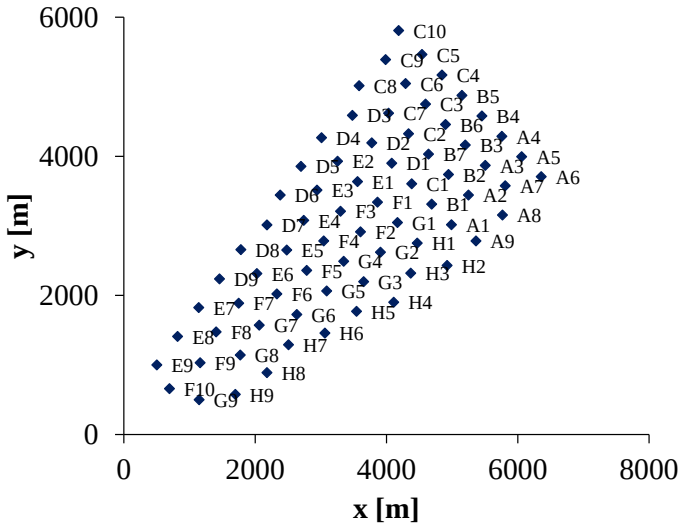

Figure 5.5.: Layout of Northwind offshore wind farm.

rows, probably aimed at maximizing production with regard to the directions of dominant wind.

Before optimizing the layout, expected yearly profits and supplied energy are computed for the current built layout (further referred to as the base layout), for different modes of operation (with and without reserve). The maximum amount of power that can be allocated to reserve R_{max} is set to different values. First, Elia has set a limit of 50 MW per delivery point in its current BSP agreement. Then, the required volume of aFRR reserves that Elia should ensure throughout the year was 117 MW for 2023. However, with the growing penetration of renewable energies foreseen in the future, one can expect that this requirement will increase as well. Indeed, power systems will become highly weather-dependant, thus more prone to variability and unpredictability. We therefore set two more values for the maximum allocated reserve: Elia's total aFRR needs (approximately equal to half of the wind farm rated capacity, if the operator wants to keep a part of available wind power for other markets), and the full farm capacity.

WFLO is then carried out with the new formulation for the objective function that maximizes profits from both day-ahead and reserve markets. Historical data from 2023 in Belgium (see section 5.2) are used during the optimization process. To assess the influence of accounting for reserve in the WFLO process, optimization with day-ahead market only is also simulated. Then, to compare with state-of-the-art WFLO formulations, the layout will also be optimized with

the objective of maximizing AEP. Results will be compared in terms of expected yearly profits and yearly production. Moreover, it is important that the optimal layouts are not only relevant for the data used in the optimization process. Therefore, yearly profits are also computed for unseen data, i.e. historical data from another year (2024).

The new objective function for WFLO has been integrated into the TOP-FARM framework ([194]), comprising the SGD optimizer. Profit and AEP gradients are computed using automatic differentiation. Turbine powers are obtained from the topology-aware wind farm surrogate developed in Chapter 3. The minimum turbine spacing d_{min} (constraint of Eq.(5.15)) is set to 2 rotor diameters. The SGD optimizations are carried out using the following parameters: the initial learning rate is one rotor diameter, the maximum number of iterations is 2000, and the initial value for the constraint aggregation multiplier is 0.1. We use several values of $K * T$ (numbers of samples for every SGD iteration) when optimizing for profits and AEP. To obtain statistically significant results, each case of SGD optimization is run using 5 different initial random starting conditions.

5.5.1. Operating the Current Built Layout with Reserve Participation

Before optimizing the layout of the Northwind wind farm, yearly profits are computed for the current layout using historical data from 2023. Three modes of operation are considered:

- Producing as much wind power as possible (referred to as prod. max. operation in results tables). Energy bids are not risk-based as they only rely on forecasts of available power, regardless of market conditions. This is the most simple operation as the operator does not need to derate the turbines in case of unfavorable market conjuncture.
- Wind power is only sold on the day-ahead market but energy bids are made based on forecasts of available wind power, day-ahead prices and imbalance penalties (referred to as DAEM optimized operation in results tables)
- Wind power is sold on JERM (provision of reserve)

The optimal allocation of day-ahead and reserve power on JERM is solved with Eq.(5.11) for every quarter of an hour of the year, and the expected profits are summed over 35,040 timesteps. The maximum value allowed for reserve bids is first set to 50 MW. The optimized operation on DAEM only uses the

same formulation but with $R_{k,t} = 0 \; \forall k, \forall t$. This allows to assess the impact of participating to the upward secondary reserve market.

The expected supplied energy is the yearly production of the farm actually injected to the grid. For the JERM case, it encompasses both the energy sold on the day-ahead energy market and the activated reserve. It should be noted that electrical losses and downtime due to maintenance and failures are not taken into account. AEP_{theory} is the *theoretical* yearly production of the farm, computed solely by converting data of wind speed and wind direction to potential wind power. It does not include any forecasting errors.

Expected yearly profits and supplied energy are reported as $\mu \pm \frac{\sigma}{\sqrt{S}}$, where the standard deviation relates to forecast uncertainty (sampling of S forecast errors). To obtain statistically significant results, we set S to 500 when computing yearly profits. Since one year is divided into 35,040 quarters of an hour, converting 500 times wind data to wind power per timestep leads to more than 17 million wind power evaluations. With Floris, the tool used to carry out wind farm simulations in section 3.2.2, it would take 161 h, while the computation time with the ML surrogate was only 4 h.

It can be seen in Table 5.1 that operating Northwind for maximizing production leads to the lowest profits. Indeed, making energy bids on DAEM only for profits maximization increases expected yearly profits by 6.47%. This can be explained by two factors. First, producing much wind power when day-ahead prices are negative is detrimental, but timesteps with such prices only occur 2.52% of the time in data from 2023. Then, forecasting prices allows to adopt a risk-aware approach, i.e., bidding more when imbalance penalty prices are expected to be close to day-ahead prices (the risk is acceptable), and bidding less than the forecasted available power in case of very high imbalance prices. This confirmed in Table 5.2, which shows the profits breakdown between positive profits and imbalance penalties. Total imbalance penalties are higher when operating for profit maximization, but the significant increase in positive profits allows to compensate for the penalties losses. Regarding supplied energy, maximizing production obviously leads to more wind power injected to the grid. The reduction of supplied energy of 4.47% when maximizing DAEM profits is very interesting, because it could lead to lower load constraints on wind turbines, thus extending turbines lifetime. However, this aspect needs to be further investigated.

Supplying secondary upward reserve (operate the wind farm on JERM) increases expected yearly profits by 7.82%, while the supplied energy is decreased by 7.67%. Indeed, bidding a given amount of power in the reserve capacity

Table 5.1.: Expected yearly profits and supplied energy in 2023 for the initial base layout of Northwind, operated for maximizing production on DAEM (a;d), maximizing profits on DAEM only (b;e), and maximizing profits on JERM (c;f, with maximum reserve bids R_{max}=50 MW). Results reported as $\mu \pm \frac{\sigma}{\sqrt{S}}$, where μ and σ relate to forecast uncertainty.

	Base layout	
Expected yearly profits		
(a) On DAEM only (prod. max.)	60.6208 ± 0.0077 M€	
(b) On DAEM only (profits max.)	64.5432 ± 0.0081 M€	▲6.47% w.r.t. (a)
(c) On JERM (with reserve)	69.5877 ± 0.0083 M€	▲7.82% w.r.t. (b), ▲14.79% w.r.t. (a)
Expected energy supplied		
(d) On DAEM only (prod. max.)	812.61 ± 0.04 GWh	
(e) On DAEM only (profits max.)	776.28 ± 0.05 GWh	▼4.47% w.r.t. (d)
(f) On JERM (with reserve)	716.72 ± 0.05 GWh	▼7.67% w.r.t. (e), ▼11.80% w.r.t. (d)
AEP_{theory}	918.39 GWh	

Table 5.2.: Breakdown of expected yearly profits in 2023 for the initial base layout of Northwind, operated for maximizing production on DAEM (a), maximizing profits on DAEM only (b), and maximizing profits on JERM (c, with maximum reserve bids R_{max}=50 MW).

	Positive profits on DAEM	Imbalance penalties on DAEM	Reserve profits	Reserve penalties
(a) On DAEM only (prod. max.)	75.5925 M€	14.9717 M€	/	/
(b) On DAEM only (profits max.)	87.0894 M€	22.5462 M€	/	/
(c) On JERM (with reserve)	82.4348 M€	22.4393 M€	9.9334 M€	0.3412 M€

and energy markets does not mean that this power will be entirely supplied. If the system negative imbalance is not too severe, only a fraction of contracted reserves is actually activated by the TSO. However, the wind farm operator still earns profits by making this power available to restore balance in the system. This is particularly profitable when day-prices are very low. It can be seen in Table 5.2 that while positive profits on DAEM are quite lower when providing reserve (earnings are "transferred" to the reserve markets), imbalance penalties do not decrease significantly. This is inherent to our formulation, because in

Table 5.3.: Expected yearly profits and supplied energy in 2023 for the initial base layout of Northwind, operated for maximizing production on DAEM (a;f), maximizing profits on DAEM only (b;g), and maximizing profits on JERM (c-e;h-j, for different limits on reserve participation, R_{max}). Results reported as $\mu \pm \frac{\sigma}{\sqrt{S}}$, where μ and σ relate to forecast uncertainty.

	Base layout	Comparison
Expected yearly profits		
(a) On DAEM only (prod. max.)	60.6208 ± 0.0077 M€	
(b) On DAEM only (profits max.)	64.5432 ± 0.0081 M€	
(c) On JERM (with reserve, R_{max}=50MW)	69.5877 ± 0.0083 M€	▲7.82% w.r.t. (b)
(d) On JERM (with reserve, R_{max}=117MW)	74.3597 ± 0.0090 M€	▲15.21% w.r.t. (b)
(e) On JERM (with reserve, R_{max}=221.4MW)	77.8529 ± 0.0111 M€	▲20.62% w.r.t. (b)
Expected energy supplied		
(f) On DAEM only (prod. max.)	812.61 ± 0.04 GWh	
(g) On DAEM only (profits max.)	776.28 ± 0.05 GWh	
(h) On JERM (with reserve, R_{max}=50MW)	716.72 ± 0.05 GWh	▼7.67% w.r.t. (g)
(i) On JERM (with reserve, R_{max}=117MW)	662.08 ± 0.04 GWh	▼14.71% w.r.t. (g)
(j) On JERM (with reserve, R_{max}=221.4MW)	625.46 ± 0.05 GWh	▼19.43% w.r.t. (g)
AEP_{theory}	918.39 GWh	

case of imbalance (available wind power is lower than total power bidded on both DAEM and reserve markets), priority is given to the reserve provision.

Sensitivity to Reserve Limit

Currently, the maximum value per delivery point of reserve capacity bids established by Elia is 50 MW. Moreover, the static volume need of aFRR reserves for the Belgian power system in 2023 was set at 117 MW. However, as stated before, in future weather-dominated power systems, the need for frequency regulation, including aFRR, will increase. Therefore, the wind farm is operated considering two other values of R_{max}: 117 MW (approximately 1/2 of rated capacity, in case the operator always wants to keep a part of available wind power for other markets), and 221.4 MW (full farm capacity).

With R_{max}=117 MW, it can be observed in Table 5.3 that for the base layout, expected yearly profits increase by 15.21% when the wind farm offers aFRR services, while supplied energy drops by 14.71%. Compared to the

previous case (R_{max}=50 MW), doubling the allowed maximum value for reserve capacity bids leads to a profit improvement also multiplied by 2 (15.21% against 7.82% previously). Regarding yearly supplied energy (on DAEM and activated reserve), it decreases when R_{max} is increased ($\approx$ 662 GWh against $\approx$ 717 GWh with R_{max}=50 MW). Indeed, allowing for higher reserve bids enables wind farms to participate more in frequency reserve services. But if reserve energy bids are not entirely activated by the TSO, less energy is supplied, while profits are increased.

With the full wind farm capacity (221.4 MW) as R_{max}, expected yearly profits on JERM in 2023 for the base layout are even higher. However, even though R_{max} is doubled compared to the previous case, profit increments are not multiplied by 2 this time. Indeed, the improvement is at 20.62%, against 15.21% when R_{max} was set at 117 MW. This shows a flattening of profits augmentation, and wind farm operators might want to avoid allocating all available power to the reserve market. Indeed, because of potential forecast errors, there is a significant risk to bid in only one market, and operators could want to keep a part of available wind power for other markets (or even a security margin to avoid penalties when the contracted power cannot be entirely supplied).

5.5.2. Optimized Layout Accounting for Reserve Provision

WFLO is carried out with the objective of maximizing profits on JERM, with SGD optimizations performed for different values of Monte-Carlo samples ($K * T$) and several initial conditions. Reported results are those obtained with the best optimized layout out of all simulations, i.e. the one leading to the highest expected yearly profits on JERM.

As it can be seen in Table 5.4, the best optimized layout leads to an increase of yearly profits on JERM by 2.23%, as well as 2.35% more supplied energy. This augmentation of production could be explained by two reasons. On the one hand, a better placement of wind turbines to avoid wake losses leads to an improved electricity production in general. On the other hand, this increase of power output coincides with wind directions related to higher electricity prices, which boosts profits. Considering that the average lifespan of an offshore wind farm is approximately 20 years [81], a profit increased by 1.56 M€ per year leads to a significant improvement in the wind farm profitability: more than 30 M€ over the farm lifetime. It should be noted that these numbers cannot be directly generalized for other electricity pools, but since most European electricity markets have a similar structure, applying this methodology is also

Table 5.4.: Expected yearly profits and supplied energy in 2023 for the best layout optimized on JERM, operated for maximizing production on DAEM (a;d), maximizing profits on DAEM only (b;e), and maximizing profits on JERM (c;f, with maximum reserve bids R_{max}=50 MW). Results reported as $\mu \pm \frac{\sigma}{\sqrt{S}}$, where μ and σ relate to forecast uncertainty.

	Base	Layout optimized on JERM
Expected yearly profits [M€]		
(a) On DAEM only (prod. max.)	60.6208 ± 0.0077	62.1989 ± 0.0073 (▲2.6% w.r.t. base)
(b) On DAEM only (profits max.)	64.5432 ± 0.0081	66.0759 ± 0.0077 (▲2.37% w.r.t. base)
(c) On JERM (with reserve)	69.5877 ± 0.0083	71.1430 ± 0.0078 (▲2.23% w.r.t. base)
Expected energy supplied [GWh]		
(d) On DAEM only (prod. max.)	812.61 ± 0.04	829.71 ± 0.04 (▲2.10% w.r.t. base)
(e) On DAEM only (profits max.)	776.28 ± 0.05	793.32 ± 0.04 (▲2.20% w.r.t. base)
(f) On JERM (with reserve)	716.72 ± 0.05	733.58 ± 0.04 (▲2.35% w.r.t. base)
AEP_{theory} [GWh]	918.39	935.41 (▲1.85% w.r.t. base)

expected to result in higher yearly profits for layouts optimized for profit maximization with reserve participation.

The best optimized layout is plotted in Fig. 5.6 and compared to the current layout of Northwind. Turbines that were on the farm boundaries in the base layout kept their position on the outer limits (even though turbines had random positions in the starting initial conditions of the optimization). However, inner turbines positions have been significantly modified compared to the base layout. Indeed, while the structure of rows has been approximately maintained, it can be observed that more turbines are placed together on a row, while consecutive rows are more distant from one another and are not parallel (which was the case for all rows in the base layout). A few turbines have a more irregular position (in-between rows).

Another interesting characteristic to compare between the optimized and base layouts is the power rose. It shows the power output of the wind farm with regard to wind direction, for a given wind speed. In Fig. 5.7, the power is normalized by the wind farm rated capacity (for Northwind, 221.4 MW). It allows to identify the wind directions leading to higher wake losses.

The power rose of Fig. 5.7(a) shows that the base layout exhibits many power drops, with wake losses being the most severe for directions of 135° and 315°

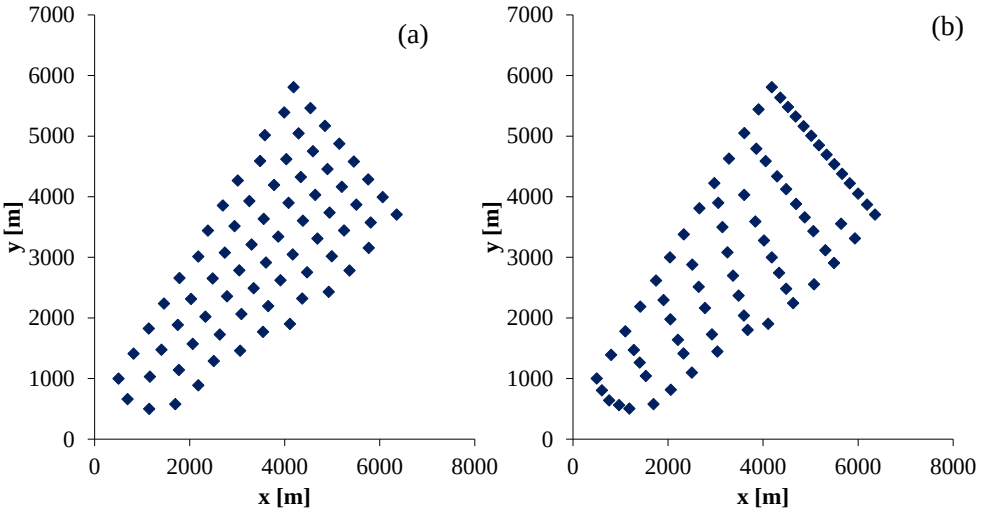

Figure 5.6.: (a) Base layout of Northwind offshore wind farm, (b) Best layout optimized for profit maximization with participation to reserve market.

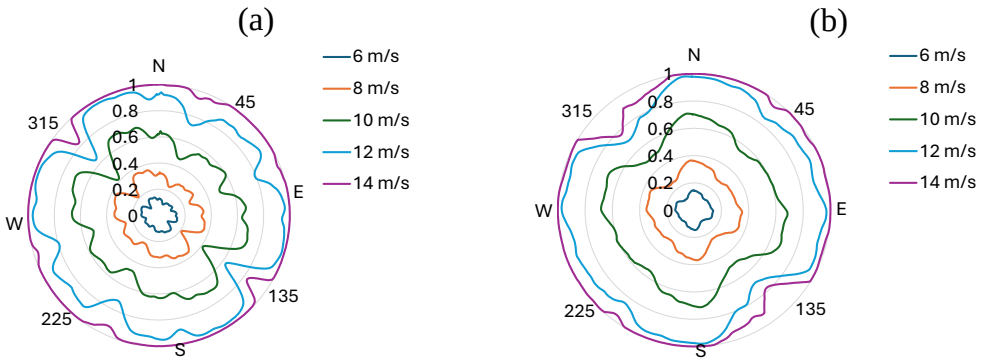

Figure 5.7.: Power roses of Northwind (a) Base layout, (b) Layout optimized for profit maximization on JERM.

(0° corresponds to wind blowing from the North, then clockwise counting). This pattern is inherent to regular layouts, where turbines are placed in rows equidistant from each other and wake losses are at their maximum when most turbines are aligned with the wind direction. In Fig. 5.7(b), wake losses are still prevalent for wind directions of 135° and 315°, but they are less severe, and power drops are smoothed for other directions. Indeed, while still located on rows, turbines from different rows are more distant, allowing wind speed to recover between consecutive rows. However, it should be noted that a more

irregular turbine placement can lead to higher installation costs and fatigue loading [68].

5.5.3. Comparison with Layout Optimized without Reserve

To assess the impact of including participation to reserve in the layout optimization process, the objective function has been modified as to only include profits from the day-ahead market (i.e., setting $R_{max} = 0$ MW), referenced as the DAEM case. Like before, SGD optimizations are performed for different values of Monte-Carlo samples ($K * T$) and several initial conditions. For every obtained layout optimized without consideration of reserves in the objective function, expected profits on DAEM only (i.e., wind farm operated without reserve) are computed. The optimized layouts for DAEM are also operated with reserve in order to compare yearly profits on JERM with those computed for the layouts optimized with reserve participation.

Fig. 5.8 shows the expected yearly profits on JERM in function of expected yearly profits on DAEM only for the layouts optimized for profits maximization with and without reserve participation. The highest profits on JERM are obtained for layouts optimized with reserve: this highlights the importance of accounting for participation of wind farms to reserve markets in the layout optimization process. Moreover, it can be seen that both yearly profits are linearly linked, i.e., higher profits on DAEM only leads to higher profits on JERM. Surprisingly, the best total yearly profits on DAEM only are obtained for cases optimized with reserve. One reason that could explain this is that during the optimization without reserve, the wind farm can only participate to one market (the DAEM). If day-ahead prices are very low or negative, wind farm will not bid on the DAEM, resulting in no profit, thus leading to a zero gradient and the solution space being less explored. This means that even if reserve market rules change dramatically, causing the wind farm to be unable to participate in the reserve market, operating the optimized layout with reserve on DAEM only would still be profitable.

5.5.4. Comparison with Layout Optimized for AEP Maximization

We compare our novel formulation for WFLO with the objective function widely used in the current literature, i.e., AEP maximization. For the latter, wind speeds and wind directions from the 2023 historical data are used during the optimization process. To benchmark the performance of our methodology, expected yearly profits on JERM are computed with reserve participation, for

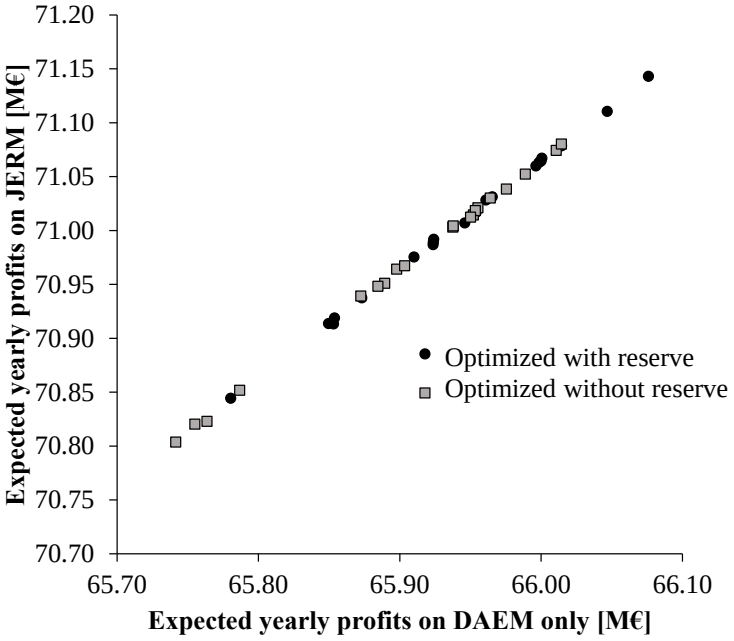

Figure 5.8.: Expected yearly profits on JERM plotted versus expected yearly profits on DAEM only (wind farm operated without reserve). Each point corresponds to one optimized layout, with the black circles representing layouts optimized with reserve, and the grey squares are for layouts optimized without reserve.

the layouts optimized for AEP maximization. It is worth reminding that while the total energy supplied indicates the actual electricity sold (or activated, in case of reserve provision) and injected to the grid, AEP gives the theoretical energy that could be supplied by the wind farm given the wind conditions, regardless of prices and errors on wind power forecasts.

Fig. 5.9 shows the expected yearly profits on JERM in function of AEP for the layouts optimized for profits maximization with reserve and AEP maximization. The uppermost black circle on the right represents the optimized layout giving the highest profits on JERM but also the highest AEP. It may seem confusing at first that the best AEP is not obtained for a layout optimized for AEP maximization. A plausible explanation is that the profit function has better gradients than the AEP objective function, allowing to avoid local minima. It should be noted that this layout corresponds to the best layout optimized for profits maximization with reserve for which results are given in Table 5.4.

Another interesting observation is that yearly profits on JERM are generally

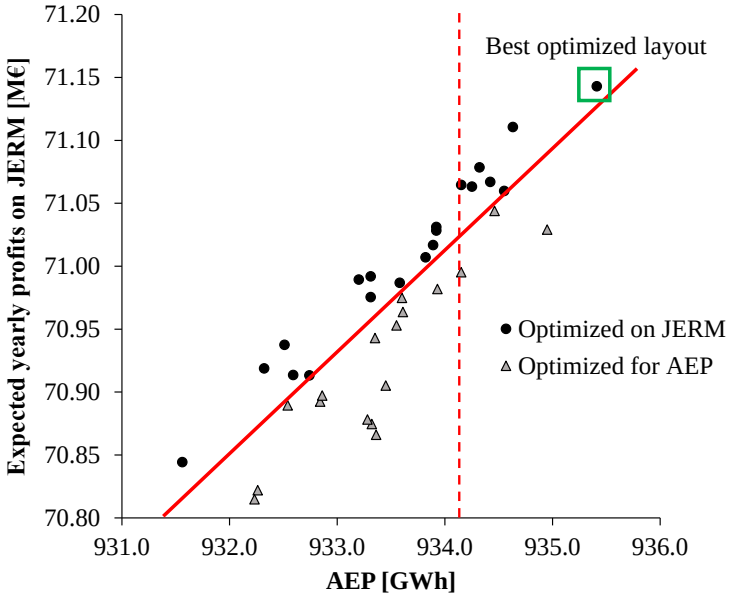

Figure 5.9.: Expected yearly profits on JERM plotted versus AEP. Each point corresponds to one optimized layout, with the black circles representing layouts optimized with reserve, and the grey triangles are for layouts optimized for AEP maximization.

higher for layouts optimized for profits maximization with reserve: if a diagonal is drawn in the scatterplot, all triangles are located below that line compared to the circles. And if a vertical line is plotted for a given AEP, black circles are always located above the triangles. In other words, for the same level of AEP, the layouts optimized for profits with reserve lead to higher profits on JERM than the ones obtained for AEP maximization. The explanation for those significant economic losses is that the objective function with AEP aims at maximizing the power output of wind farm regardless of electricity prices. It usually avoids wake losses for the directions of dominant wind. However, if low or even negative prices are associated with those directions, then profits will not increase. Moreover, besides profits, it is not beneficial for the grid that wind farms produce a lot of electricity when prices are quite low. Indeed, for power systems with a high penetration of renewable energies, especially wind, low or even negative prices may correspond to periods of overproduction, i.e., generation exceeds consumption. In that case, wind turbines might have to be curtailed to reduce wind energy production and restore balance in the system. This spillage of renewable energy is of course not desirable and it is much more relevant to optimize wind farm layouts so that they produce more

energy during times of scarcity (usually associated with higher prices).

5.5.5. Generalization to Unseen Future Data

In Sections 5.5.1 to 5.5.4, historical data from 2023 were used during the SGD optimizations, as well as for the computation of expected yearly profits for the optimized layouts. In this section, revenues and supplied energy will be assessed with historical data from 2024, i.e., data unseen during the optimization process. Indeed, it is valuable to have optimized layouts that also yield improved profits for future years.

First, wind data and electricity prices from January to July 2024 are analysed. The wind rose of 2024, plotted in Fig. 5.10(d), shows patterns comparable with 2023: dominant wind directions are mostly South-Westerly. More wind blowing from the North-East was visible in Fig. 5.1(d), which is not the case here. It can be seen in Fig. 5.10(a) that day-ahead prices, similar to 2023, have lower values for the direction of dominant winds, although this is less noticeable than in 2023. Moreover, day-ahead prices in 2024 have overall lower mean values than in 2023. Reserve capacity prices do not vary much with wind direction, while activation prices show more variability but no significant drop for the directions of dominant wind. The overall mean values are in the same order of magnitude than for the previous year, and we observe again a sharp increase in reserve activation prices between 20 and 25 m/s. However, this peak is less pronounced, with a mean peak value under 200€/MWh while it reached almost 250€/MWh in 2023. This could be explained by less sudden and high wind events (e.g., storms), a smoother farm cut-out, or a better anticipation by the TSO. Normalized activation volumes exhibit lower values for directions of dominant wind. Therefore, while wind, prices and activated reserve volume of 2024 share some similarities with data from 2023, they also exhibit noticeable differences. They are thus relevant to test the validity of the optimized layouts on unseen data. The case presented here uses R_{max}=50 MW when the wind farm is operated with reserve.

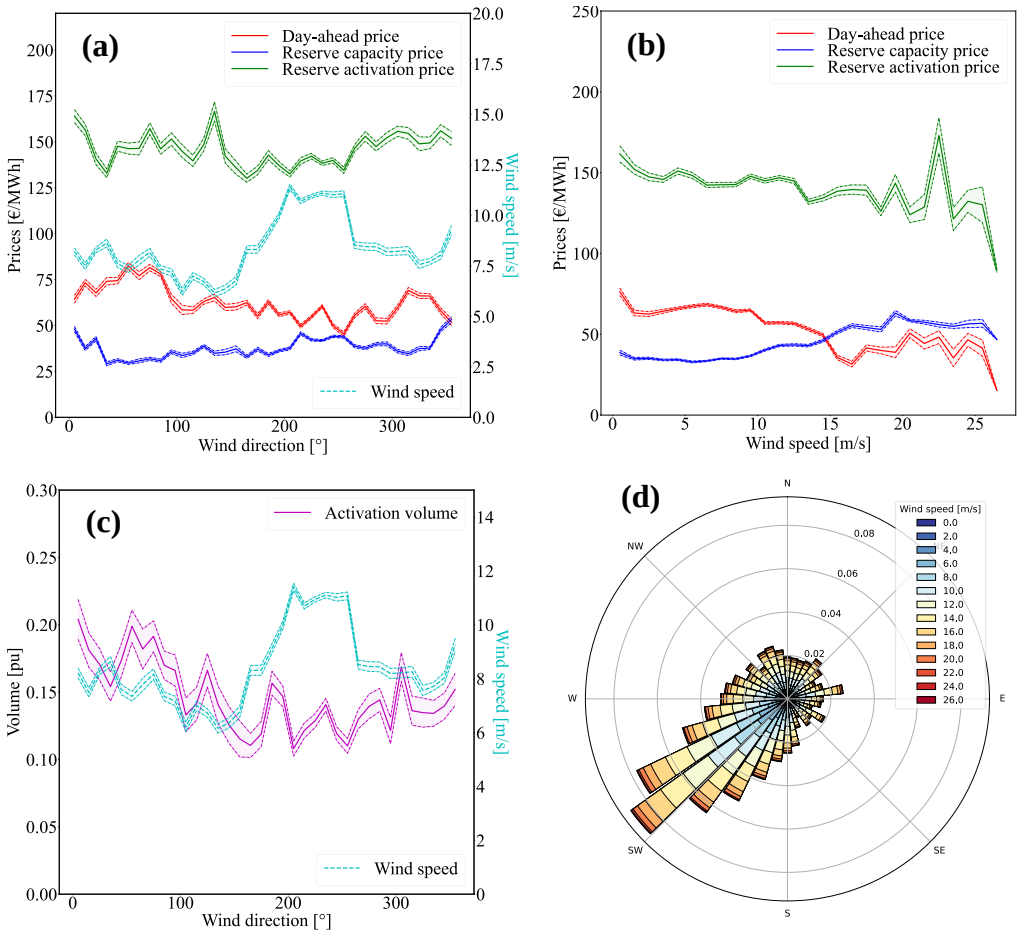

Figure 5.10.: Mean electricity prices with regard to (a) wind direction and (b) wind speed in 2024. (c) Mean normalized activated volumes of reserve with regard to wind direction. (d) Wind rose at the location of Belgian offshore wind farms for 2024, from ERA5 data (latitude: 51.5°N, longitude: 2.75°E)

For the base layout, it can be observed in Table 5.5 that results show the same trends already noticed for 2023: profits on DAEM only are increased when energy bids are made to maximize profits and not power production. Participating to reserve leads to yearly profits improved by 20.97%, while it was only 7.82% for 2023. A reason for this better improvement is the overall lower values of day-ahead prices in 2024, thus giving more opportunities to make profits on reserve markets. Indeed, allowing participation to reserve markets increases profits significantly when the day-ahead market is less profitable.

Table 5.5.: Expected yearly profits and supplied energy in 2024 for the base and best layout optimized on JERM with 2023 data, both operated for maximizing production on DAEM (a;d), maximizing profits on DAEM only (b;e), and maximizing profits on JERM (c;f, with maximum reserve bids R_{max}=50 MW). Results reported as $\mu \pm \frac{\sigma}{\sqrt{S}}$, where μ and σ relate to forecast uncertainty.

	Base	Layout optimized on JERM
Expected yearly profits [M€]		
(a) On DAEM only (prod. max.)	18.8986 ± 0.0054	19.4822 ± 0.0050 (▲3.09% w.r.t. base)
(b) On DAEM only (profits max.)	21.3492 ± 0.0043	21.9111 ± 0.0040 (▲2.63% w.r.t. base)
(c) On JERM (with reserve)	25.8267 ± 0.0045	26.4243 ± 0.0042 (▲2.31% w.r.t. base)
Expected energy supplied [GWh]		
(d) On DAEM only (prod. max.)	445.74 ± 0.03	455.23 ± 0.03(▲2.13% w.r.t. base)
(e) On DAEM only (profits max.)	394.98 ± 0.03	404.21 ± 0.03 (▲2.34% w.r.t. base)
(f) On JERM (with reserve)	347.56 ± 0.03	356.52 ± 0.03 (▲2.58% w.r.t. base)
AEP_{theory} [GWh]	506.93	516.24 (▲1.84% w.r.t. base)

The best layout optimized on JERM is the same than the one presented in Tab. 5.4, i.e. optimized with 2023 data. When operated using 2024 data, the optimized layout leads to higher total profits and supplied energy, in the same order of magnitude than for 2023. These results show that the optimized layout obtained with data from 2023 is still relevant for 2024, even though both year showed dissimilarities in wind distribution and prices.

If we compare again our methodology with the AEP maximization formulation, we observe the same patterns than for 2023. Indeed, when plotting expected yearly profits on JERM in function of AEP, for layouts optimized for profits on JERM and for AEP, we still see that the grey triangles representing layouts for AEP maximization are below the black circles. However, it can be observed that a few black circles are below triangles. This implies that those layouts optimized for profit maximization with reserve are less optimal regarding wind data and electricity prices from 2024.

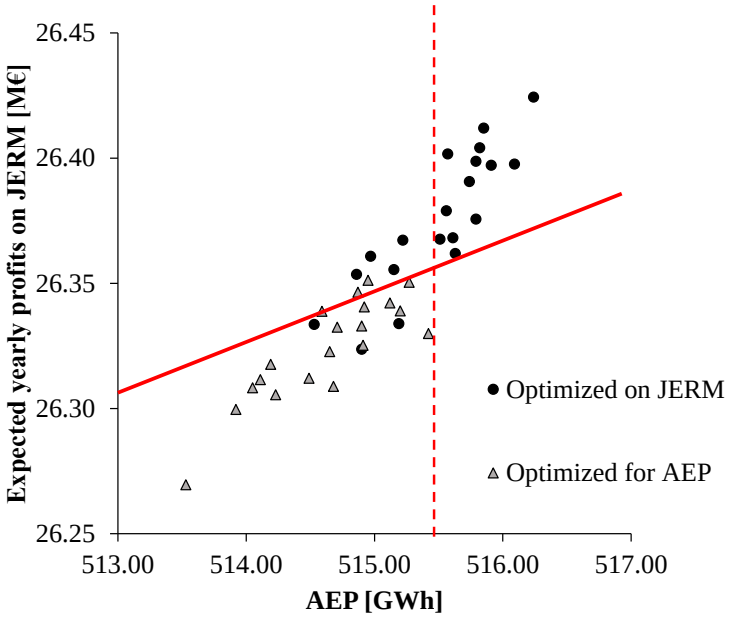

Figure 5.11.: Expected yearly profits on JERM in 2024 plotted versus AEP. Each point corresponds to one layout optimized using 2023 data, with the black circles representing layouts optimized with reserve, and the grey triangles are for layouts optimized for AEP maximization.

5.6. Conclusion

In this chapter, the ML surrogate developed in Chapter 3 was integrated within a wind farm layout optimization problem accounting for reserve provision by offshore turbines. Indeed, in the forthcoming years, offshore wind farms are expected to have a significant role for restoring frequency balance through the provision of reserve. Future wind farms should therefore be designed for that purpose. This chapter develops a new methodology for WFLO to account for future offshore wind farms participating to secondary upward reserve markets. The objective function aims at maximizing revenues from both day-ahead and reserve markets. It uses stochastic gradient descent for the optimization and probabilistic forecasts of wind power and electricity prices. An inner optimization problem provides the total power contracted on the JERM and the allocation of power to reserve procurement purposes.

When applied on a real-life Belgian test case, results show that yearly profits are expected to increase in a significant way when accounting for participation

to reserve markets, while exhibiting a lower supplied energy. This profit augmentation is amplified when the maximum value for reserve bids is increased. Moreover, layouts optimized for profit maximization with reserve markets lead to better yearly profits than when considering day-ahead market only in the objective function. Profits are also higher for the developed methodology than for layouts optimized for AEP maximization, widely used in the literature, even though the AEP is similar. Finally, the optimized layouts also yield better profits when computed using unseen data. Besides higher revenues, it is critical that wind farms are designed to produce more energy when prices are higher, usually corresponding to periods of electricity shortage. Maximizing production when prices are low or even negative, generally associated with a surplus of generation, leads to spillage of renewable energy.

Chapter Publication

- **T-H. Nguyen**, J. Quick, P-E. Réthoré, J-F. Toubeau, E. De Jaeger and F. Vallée, "Offshore Wind Farm Layout Optimization Accounting for Participation to Secondary Reserve Markets", submitted to *Wind Energy Science*

CHAPTER 6.

Conclusions and Perspectives

Global warming is not the only negative impact that human activities have on our planet. The energy transition must aim not only at preventing climate change, but also at returning us below the 9 planetary boundaries that describe limits beyond which the environment may not be able to self-regulate anymore. Equally important is that the energy transition must be fair, allowing everyone to thrive in an environment respectful of the Earth. In other words, we need to find the safe space between the 9 planetary boundaries and a social foundation of well-being that no one should fall below (this is the main concept of the Doughnut). Encompassed within the basics needs of life is notably access to energy.

Renewable energy sources are expected to play a significant role against climate change, as they emit very low greenhouse gases during their operational lifetime. However, solar panels and wind turbines require a lot of raw materials, obtained through mining, and a considerable surface area, potentially jeopardizing biodiversity and land use (through deforestation) and affecting other planetary boundaries. Therefore, the operation of those energy sources must be optimized to produce electricity in the most efficient way and avoid spillage of electricity. Moreover, renewable energy sources are inherently intermittent, fluctuating, and highly unpredictable, thus posing many challenges to ensure a reliably supply of electricity. A detailed planning and usage throughout the year will be necessary to guarantee access to electricity for everyone, at all times, and at an affordable price.

Considering those challenges, this work did not have the ambition to tackle all those aspects, but aimed at discussing the impact of the massive installation of renewable energy sources, targeting one type in particular: offshore wind energy. This work is thus focused on three complementary research questions with the purpose of improving the integration of future offshore wind farms

in power systems by assessing their impact on the reliability of supply and their ability to provide balancing services. The first objective was to develop a fast and accurate model for offshore wind farms, able to capture complex aerodynamic phenomena while keeping a reasonable computation time. This led to a topology-aware offshore wind farm surrogate, able to generalize to any layout configuration. Then, the research focus was put on adequacy studies aiming at assessing the reliability of electricity supply in future power systems with a high share of offshore wind generation. The developed surrogate was leveraged to assess the impact of an improved modelling of offshore wind power on reliability indices. Thirdly, we focused on the foreseen participation of offshore wind farms to reserve markets, aiming at restoring balance within the system in case of sudden perturbations. We explored how the layout of future wind farms can be optimized to account for their participation to ancillary frequency services.

In this final chapter, the developments and findings presented throughout the dissertation are summarized. Then, perspectives for future research are formulated.

6.1. Concluding Remarks

Considering the massive growth of offshore wind generation in electrical grids (in Europe, but also in China and perhaps in the United States), the techno-economic analysis of modern power systems can no longer be envisioned without an accurate modelling of this fluctuating generation within power system computations. Because of complex aerodynamic phenomena arising within offshore wind farms, modelling their power output is an intricate process. While high-fidelity wind farm simulations allow to capture aerodynamic effects between interacting turbines and their impact on electricity production, they are generally computationally demanding and time consuming. Therefore, they cannot be used as such in iterative power system computations.

In this work, a new methodology is developed to improve the modelling of offshore wind power within time demanding computations. In **Chapter 3**, a Machine Learning-based wind farm surrogate is created, allowing to account for aerodynamic losses arising in large offshore wind farms without compromising tractability. The model, based on MLP neural networks, is trained on a large database built upon wind farm simulations, thus removing the need for historical data (rarely publicly available, for confidentiality and strategic reasons, and not existent for future wind farms yet to be built). The ML surrogate is fed by new geometric and physics-informed input features such that it is generic and

topology-aware, i.e., it can be applied to any offshore wind farm configuration. This topology-aware aspect ensures that the training process is carried out only once. Moreover, this model allows to account for disabled turbines (failures or maintenance) and the subsequent wake redistribution.

Comparisons with very high-fidelity simulations of a real-life offshore wind farm demonstrate the validity of the developed methodology. Moreover, the topology-aware ML surrogate is shown to be more than 25 times faster than the wind farm simulations carried out to build the training database. The proposed methodology is easy to implement and to reproduce, as it only uses publicly available data (wind farm layout, turbine power curve, wind database) and simulation outputs.

Within problems involving iterative computations, wake effects occurring in offshore wind farms are often taken into account in a very simplified way or even completely disregarded, even though they greatly influence the power output. Assessing the adequacy of modern power systems usually involves such iterative computations. Therefore, in **Chapter 4**, the developed ML surrogate is directly integrated within adequacy studies using sequential Monte-Carlo simulations. The fast inference time and topology-aware abilities allow an improved modelling of offshore wind farms without hindering the tractability of the computation process. In that way, it leads to a better assessment of the security of supply and an accurate computation of reliability indices for modern power systems.

Results of a test case, based on a simplified model of the Belgian power system in 2030, demonstrate the relevance of an improved modelling of offshore wind generation as it significantly affects adequacy outcomes. Indeed, with a power curve approach (generally used in adequacy studies) that ignores wake losses, we observe a noteworthy underestimation of LOLE and LOEE values. This error increases with both the installed capacity and power density within the farms, potentially exceeding 18%. This can critically affect adequacy assessments, particularly in a context of increased wind energy integration. Indeed, underestimating reliability indices may conceal adequacy issues, thereby preventing to make the right investments and take the appropriate necessary planning actions to ensure a sufficient reliability of the system.

The generalization abilities allow to account for various possibilities related to future wind farms topology. Indeed, their layout (turbine position, power density, turbine technology) is still unknown, as the tendering process should begin in late 2024. Therefore, it is important to consider multiple scenarios for the future offshore zone in Belgium in order to account for the current

uncertainty on the energy that will be provided by the different wind farms. Thanks to the topology-aware abilities of the ML surrogate, the same model can be used to consider many possible farm configurations, thereby preventing the need to train one model per configuration, as it would be the case with traditional farm-specific surrogates. Outcomes show that increasing power density improves reliability indices, but exhibit diminishing marginal returns after a certain point, due to the amplification of wake losses caused by the additional turbines. The installed capacity should thus result from a well-studied compromise between increasing the yearly offshore production while limiting power losses from wake effects. Moreover, the choice of turbine models also impacts adequacy results, as larger rotor diameters (for the same total farm capacity) decreases LOLE and LOEE values, but at the expense of higher turbine costs.

Current offshore wind farms are usually operated to maximize the annual energy production, and they have been designed with that purpose. However, in the forthcoming years, offshore wind farms are expected to have a significant role for restoring frequency balance through the provision of reserve. Future wind farms should therefore be designed for that purpose. In **Chapter 5**, the ML surrogate was integrated within a wind farm layout optimization problem accounting for reserve provision by offshore turbines. This chapter develops a new methodology for WFLO to account for future offshore wind farms participating to secondary upward reserve markets. The objective function aims at maximizing revenues from both day-ahead and reserve markets. It uses stochastic gradient descent for the optimization and probabilistic forecasts of wind power and electricity prices. An inner optimization problem provides the total power contracted on the JERM and the allocation of power to reserve procurement purposes.

The developed topology-aware ML surrogate is especially appropriate for a wind farm layout optimization problem. Indeed, for a fixed number of turbines with given characteristics, the optimal siting will aim at placing turbines to minimize power losses due to wakes, considering the wind regime (i.e., dominant wind directions) at the farm location. Accurately modelling wake losses is thus crucial in that context as it will directly influence the optimized solution. Moreover, at each optimization step, turbines are moved within the farm boundaries until convergence is reached for the optimal positioning. Therefore, a different layout is seen at each iteration, justifying the need for a topology-aware model, applicable to any wind farm configuration.

When applied on a real-life Belgian test case, results show that yearly profits are expected to increase in a significant way when accounting for participation

to reserve markets, while exhibiting a lower supplied energy. Moreover, layouts optimized for profit maximization with reserve markets lead to better yearly profits than when considering day-ahead market only in the objective function. Profits are also higher for the developed methodology than for layouts optimized for AEP maximization, widely used in the literature. Finally, the optimized layouts also yield better profits when computed using unseen data. Besides higher revenues, it is critical that wind farms are designed to produce more energy when prices are higher, usually corresponding to periods of electricity shortage. Maximizing production when prices are low or even negative, generally associated with a surplus of generation, leads to spillage of renewable energy.

6.2. Perspectives for Future Research

On a Topology-aware Offshore Wind Farm Surrogate

- **Perspective 1 - on enriching the training database**
  In this work, an engineering tool was used to run wind farm simulations. Although the tool was validated with very high-fidelity simulations, it is clear that more advanced models would have a higher accuracy. Currently, the high computational time of such advanced methods prohibit their use to build a database with a significant amount of samples. However, if future models are able to reduce the computational time, and a relevant database can be generated, then the methodology presented in this paper could still be used, but with this new database. Besides, the lack of publicly available operational data for offshore wind farms has gradually incentivised research academics to publish simulations data, especially when the latter are carried out using intensive computation methods such as LES or RANS [195]–[198]. Because of the computational burden and the recentness of the initiative, the number of cases is still very limited and would not constitute a comprehensive database sufficient to train our model. However, in the meantime, a multi-fidelity database could be built with the lower-fidelity simulations obtained with wake models, combined with few cases of high-fidelity simulations. For example, in multi-fidelity composite neural networks [199], a first training is carried out using the low-fidelity data, then corrected in a next stage by coupling with high-fidelity neural networks in order to discover and exploit correlations between low-fidelity and high-fidelity data. Another possibility would be to leverage a gaussian process regression framework to combine information from low and high-fidelity simulations [200].

- **Perspective 2 - on capturing wind dynamics**
  Computing hourly averaged wind power can be carried out with two ways: by directly using hourly averaged wind data (which was the case in this work), or by converting wind time series to power time series and average the latter (quasi-steady or even dynamic approach). Because the wake takes time to propagate within a wind farm (especially for large farms), those two methods could lead to different power assessments. The recent advancements regarding dynamic wake models [201]–[204] would allow to capture wind power variation and replace steady-state simulations by dynamic ones. Those dynamic wake models are faster than CFD simulations and first results show a relatively good accuracy compared to high-fidelity CFD simulations [205]. In particular FloriDyn is a dynamic version of Floris, the open-source code used in Chapter 3 to build the training database of wind farm simulations, but it is still under development. Building a database of dynamic wind farm simulations would allow to train a ML surrogate able to capture wind (and thus power) variations within an hour. For example, wind inputs would consist in not only the average value of wind speed and wind direction, but also other statistics such as standard deviation (or higher statistical moments) that capture wind changes.

- **Perspective 3 - on the consideration of turbine control**
  Throughout this work, it was assumed that wind turbines are actively controlled for maximum power point tracking and that the nacelle is always perfectly facing the main wind direction. Indeed, it is the common practice in commercial wind farms as operators aim at maximizing annual energy production. However, methods for decreasing wake losses are actively studied, the main ones being wake steering and axial induction control. Even though these techniques could be associated with an increase on loads and fatigue on the turbine blades, the wind industry has recognized the potential of an improved wind farm control. If such wind farm controls are to be implemented in the future, new simulations where wind turbines are controlled with yaw steering, induction control, or other methods, should be run. Additional features would have to be fed to the ML surrogate to describe the control strategy used in the farm. This could prove especially challenging if different strategies are applied to individual wind turbines, leading to a heterogeneous control distribution within the farm and a complex distribution of wakes.

On Adequacy Studies with a High Share of Offshore Generation

- **Perspective 1 - on wake effects between neighbouring wind farms**
  While intra-farm wake effects have been considered in the adequacy studies thanks to the ML surrogate, wake effects between neighbouring wind farms have been ignored. However, inter-farm effects are particularly relevant if wind farms are installed close to each other and if the dominant wind direction blows throughout several adjacent farms. Even for more distant wind farms, the influence of an upwind farm is sometimes not negligible, depending on wind conditions and farm characteristics. For example, in Belgium, the potential impact of the new offshore zone on the already built turbines has been studied [206], although it will be situated at a distance of approximately 8 km (for the closest point) to 42 km (for the furthest point) from the first offshore cluster. It was shown that AEP loss due to the new zone could reach 0.8%, but more importantly that in worst-case wind conditions, power losses can be as high as 20%. For future electricity systems reliant on offshore wind, such a momentary drop in wind power due to farm interactions can potentially cause unexpected grid instability. Therefore, inter-farm wake effects should be encompassed in future work on adequacy studies with a high share of offshore wind generation. Wind farm wake is a very complex flow, and its computation differ from the prediction of individual wind turbine wakes. Although the turbine wake models used in Chapter 3 are not directly adapted to compute farm wake, other tools have recently been developed with the purpose of estimating the influence of an entire wind farm on the incoming wind [207]–[209]. Therefore, the power assessment for a given wind farm would be carried out in two steps: firstly, estimate the influence of upstream wind farms (if present) on the incoming wind, then feed this computed waked wind to our ML surrogate.

- **Perspective 2 - on intra-hour wind power variability**
  The adequacy studies carried out in this work have a temporal resolution of 1 hour, which was highly suitable when power systems were dominated by conventional generation. However, for modern power systems with a high share of renewables, this hourly granularity may no longer be appropriate. For offshore wind farms, ramping events correspond to sudden changes in wind power. The main cause for those events is wind speed fluctuations. This is especially significant if those variations occur around the steep part of the power curve, where the wind farm power can ramp significantly in 5 minutes [210]. Another root cause for ramping events can be changes in wind direction, as the wake from upstream wind

farms and the wakes inside the wind farm are modified. With several offshore wind farms close to each other, the wind speeds and directions are highly correlated, and therefore the total offshore wind power ramping can become critical. For example, in Belgium, in the evening on the 10^{th} of August, a reduction in wind speed from approximately 13 m/s to 8 m/s led to a power decrease from full to less than half in less than one hour [210]. For adequacy studies, it could mean that the integral over one hour is such that mean generation covers the load, but some smaller periods may be inadequate, with no sufficient generation. To capture this aspect, wind data with a higher temporal resolution is needed: since offshore wind modelling generally has an hourly granularity, measurements might be required to generate wind time series with timesteps of e.g. 15 minutes. The hourly resolution could be kept for conventional generation, and the impact of sudden wind generation variations on reliability indices should be assessed.

On Wind Farm Layout Optimization Accounting for Reserve Participation

- **Perspective 1 - on forecast errors**
  For the optimal bidding strategy on JERM, probabilistic forecasts of wind power, electricity prices and reserve activation volume were used to account for forecasting error. Those forecast errors are sampled from a normal distribution related to each variable, meaning that those forecasts are independant. However, this is a huge assumption that may not be realistic. Indeed, one can expect that a large error on wind forecast (e.g., overestimating wind power) will lead to a large error in day-ahead and imbalance prices (underestimation), especially in weather-dominated power systems. A better modelling of forecast errors could take into account cross-correlation between wind, price and activated reserve forecasts. Although this would not change the WFLO formulation, it would impact day-ahead and reserve bidding, and subsequent profits.

- **Perspective 2 - on the impact of reserve provision for turbine loading**
  The components of a wind turbine are constantly impacted by both static and dynamic loads. It has been shown that supplying upward frequency services (i.e., keeping a power reserve so that increases in power are possible) could have a beneficial effect on static loading [211], as it tends to decrease extreme loads in faster winds. Moreover, as it was shown in the test case of Chapter 5, wind farms participating in the reserve market supply less energy, which would reduce static loads as well as

operation and maintenance costs of the wind farm components, thereby increasing the farm lifetime. However, regarding dynamic and fatigue loading, additional mechanical constraints are also sustained by turbines when providing ancillary services. Indeed, when actively participating to frequency reserve markets, the power reference setpoint of the wind farm could be frequently modified, thus creating load fluctuations on turbines. Therefore, mechanical fatigue of wind turbine components could be increased due to dynamic load variations. Computing the resulting impact on blade loads (static and dynamic) would be relevant to assess the costs versus benefits of providing reserve services. Moreover, it could be influencing the layout optimization as well.

- **Perspective 3 - on an objective function aiming at benefiting society**
  In our formulation of the layout optimization for wind farms providing reserve, the objective function is to maximize profits for the farm owners. However, coming back to the Doughnut described in the introduction of this manuscript, what we really want to optimize is the value of energy, and not profits as such. Maximizing offshore wind farm utilities means providing reserve only if necessary, and maximizing electricity production in times of high demand or scarcity, but not when the grid is already saturated with overproduction. Indeed, in that case, wind turbines might have to be curtailed to reduce wind energy generation and this spillage of renewable energy is of course not desirable. If wind farms are not properly designed and operated to maximize utility and societal welfare, it could lead to the installation of more turbines than necessary, thus impacting land use, exploitation of resources, biodiversity, ... In this work, we assume that electricity prices are a good representation of the value of energy (higher prices in periods of scarcity, and low or even negative prices in case of overproduction in the system), which is why we aimed at maximizing profits. However, we know that it might not always be the case, as it was demonstrated during the recent 2022 energy crisis. Although gas price spikes could partially explain the overly high electricity prices, uncertainty and fear of shortages also contributed. Moreover, in the current liberalized system, electricity is traded on markets as a commodity and is thus subjected to market schemes, malfunctions, and sometimes wrong assumptions (such as the presumption of unlimited resources). Therefore, it could be interesting to develop another objective function for the layout optimization problem, using a proxy for the value of energy instead of profits. Finding such a proxy is a rather complex task but a great challenge to take a step forward towards a fair energy transition within the limits of our planet.

Bibliography

[1] IPCC Core Writing Team, H. Lee and J. Romero (eds.), "Climate change 2023: Synthesis report," Intergovernmental Panel on Climate Change (IPCC), Tech. Rep., 2023.

[2] K. Richardson, W. Steffen, W. Lucht, *et al.*, "Earth beyond six of nine planetary boundaries," *Science advances*, vol. 9, no. 37, 2023.

[3] M. Jacobson, *No Miracles Needed: How Today's Technology Can Save Our Climate and Clean Our Air*. Cambridge University Press, 2023.

[4] United Nations, "The United Nations world water development report 2024: Water for prosperity and peace.," UNESCO, Tech. Rep., 2024.

[5] "Climate change and health," World Health Organization, Tech. Rep., 2023.

[6] "How climate change impacts marine life," European Environment Agency, Tech. Rep., 2023.

[7] G. Cissé, "Food-borne and water-borne diseases under climate change in low-and middle-income countries: Further efforts needed for reducing environmental health exposure risks," *Acta tropica*, vol. 194, pp. 181–188, 2019.

[8] B. P. White, S. Breakey, M. J. Brown, *et al.*, "Mental health impacts of climate change among vulnerable populations globally: An integrative review," *Annals of global health*, vol. 89, no. 1, 2023.

[9] K. Raworth, *Doughnut economics: Seven ways to think like a 21st-century economist*. Chelsea Green Publishing, 2017.

[10] Elia, *Elia open data portal*, last access: November 2024. [Online]. Available: `https://opendata.elia.be/pages/home/`.

[11] B. Li, S. Basu, S. J. Watson, and H. W. Russchenberg, "Mesoscale modeling of a "dunkelflaute" event," *Wind Energy*, vol. 24, no. 1, pp. 5–23, 2021.

[12] S. Plamondon, "Inequality in abundance," *Frontiers in Research Metrics and Analytics*, vol. 7, 2022.

[13] "World energy outlook 2023," Internatinonal Energy Agency (IEA), Tech. Rep., 2023.

[14] "Global wind report," Global Wind Energy Council, Tech. Rep., 2024.

[15] "Global offshore wind report," Global Wind Energy Council, Tech. Rep., 2024.

[16] "Delivering on the EU offshore renewable energy ambitions," European Commission, Tech. Rep., 2023.

[17] European Commission: Directorate-General for Climate Action, "Going climate-neutral by 2050," European Commission, Tech. Rep., 2019.

[18] J. Millward-Hopkins, J. K. Steinberger, N. D. Rao, and Y. Oswald, "Providing decent living with minimum energy: A global scenario," *Global Environmental Change*, vol. 65, p. 102 168, 2020.

[19] *Belgian Offshore Platform*, last access: August 2024. [Online]. Available: `https://www.belgianoffshoreplatform.be/en/`.

[20] S. Degraer, R. Brabant, B. Rumes, and L. Vigin, *Environmental Impacts of Offshore Wind Farms in the Belgian Part of the North Sea: Empirical Evidence Inspiring Priority Monitoring, Research and Management*. Dec. 2020, ISBN: 978-9-0732-4252-4.

[21] T. V. der Straten, "Public consultation on the offshore wind tender for the princess elisabeth zone," FPS Economy, Tech. Rep., 2022.

[22] T. Letcher, *Wind Energy Engineering: A Handbook for Onshore and Offshore Wind Turbines*. Elsevier, 2023.

[23] F. Vallée, "Etude de la fiabilité, au sens de l'adéquation, des réseaux électriques en présence de production décentralisée de type éolien.," Ph.D. dissertation, Faculté Polytechnique de Mons, 2007.

[24] R. Billinton and R. N. Allen, *Reliability Evaluation of Power Systems*, Second. Reading, MA: Plenum Press, 1996.

[25] "Adequacy and flexibility study for belgium 2024-2034," Elia, Tech. Rep., 2023.

[26] N. Kayedpour, J. D. M. D. Kooning, A. E. Samani, F. Kayedpour, L. Vandevelde, and G. Crevecoeur, "An optimal wind farm operation strategy for the provision of frequency containment reserve incorporating active wake control," *IEEE Transactions on Sustainable Energy*, vol. 15, no. 1, pp. 276–289, 2024.

[27] N. Kayedpour, A. E. Samani, J. D. M. De Kooning, L. Vandevelde, and G. Crevecoeur, "Model predictive control with a cascaded hammerstein neural network of a wind turbine providing frequency containment reserve," *IEEE Transactions on Energy Conversion*, vol. 37, no. 1, pp. 198–209, 2022.

[28] P. Gipe and E. Möllerström, "An overview of the history of wind turbine development: Part I — the early wind turbines until the 1960s," *Wind Engineering*, vol. 46, no. 6, pp. 1973–2004, 2022.

[29] T. J. Price, "James Blyth — Britain's first modern wind power pioneer," *Wind engineering*, vol. 29, no. 3, pp. 191–200, 2005.

[30] "Statistical review of world energy, 73rd edition," Energy Institute, Tech. Rep., 2024.

[31] "Belgian energy data overview," SPF Economy, Tech. Rep., 2024.

[32] K. Johansen, "Blowing in the wind: A brief history of wind energy and wind power technologies in denmark," *Energy Policy*, vol. 152, p. 112 139, 2021.

[33] F. Trigaux, P. Chatelain, and G. Winckelmans, "Investigation of blade flexibility effects over the loads and wake of a 15 MW wind turbine using a flexible actuator line method," *Wind Energy Science Discussions*, vol. 2024, pp. 1–33, 2024.

[34] A. Betz, "The maximum of the theoretically possible exploitation of wind by means of a wind motor," *Wind Engineering*, vol. 37, no. 4, pp. 441–446, 2013.

[35] J. F. Manwell, J. G. McGowan, and A. L. Rogers, *Wind Energy Explained: Theory, Design and Application*. John Wiley & Sons, 2010.

[36] "General Specification V112–3.0 MW 50/60 Hz," Vestas, Tech. Rep., 2010.

[37] X. Zhang, J. Jia, L. Zheng, W. Yi, and Z. Zhang, "Maximum power point tracking algorithms for wind power generation system: Review, comparison and analysis," *Energy Science & Engineering*, vol. 11, no. 1, pp. 430–444, 2023.

[38] S. C. Pryor, R. J. Barthelmie, and T. J. Shepherd, "Wind power production from very large offshore wind farms," *Joule*, vol. 5, no. 10, pp. 2663–2686, 2021.

[39] S. Wang, P. Cook, A. Stein, J. Lloyd, and C. Smith, "Updated mining footprints and raw material needs for clean energy," The Breakthrough Institute, Tech. Rep., 2024.

[40] I. Komusanac, G. Brindley, D. Fraile, and L. Ramirez, "Wind energy in europe - 2021 statistics and the outlook for 2022-2026," WindEurope, Tech. Rep., 2022.

[41] I. Kamwa, "Offshore wind energy transmission - challenges and innovations in collecting and transmitting electricity from sea to cities," *IEEE Power & Energy Magazine*, vol. 22, no. 5, pp. 4–16, 2024.

[42] IRENA, "Renewable power generation costs in 2023," International Renewable Energy Agency, Tech. Rep., 2023.

[43] R. Nicholls-Lee, "A low motion floating platform for offshore wind resource assessment using lidars," in *International Conference on Offshore Mechanics and Arctic Engineering*, American Society of Mechanical Engineers, 2013.

[44] M. J. Kühn, *Dynamics and design optimisation of offshore wind energy conversion systems*. DUWIND, Delft University Wind Energy Research Institute Delft, The Netherlands, 2001.

[45] *Record-breaking Vestas offshore turbine gets type certification*, last access: October 2024. [Online]. Available: `https://www.windpowermonthly.com/article/1849658/record-breaking-vestas-offshore-turbine-gets-type-certification`.

[46] R. Barthelmie, B. Grisogono, and S. Pryor, "Observations and simulations of diurnal cycles of near-surface wind speeds over land and sea," *Journal of Geophysical Research: Atmospheres*, vol. 101, no. D16, pp. 21 327–21 337, 1996.

[47] M. J. Churchfield, S. Lee, J. Michalakes, and P. J. Moriarty, "A numerical study of the effects of atmospheric and wake turbulence on wind turbine dynamics," *Journal of turbulence*, no. 13, 2012.

[48] T. Uchida, "Effects of inflow shear on wake characteristics of wind-turbines over flat terrain," *Energies*, vol. 13, no. 14, p. 3745, 2020.

[49] R. J. Barthelmie, K. Hansen, S. T. Frandsen, *et al.*, "Modelling and measuring flow and wind turbine wakes in large wind farms offshore," *Wind Energy: An International Journal for Progress and Applications in Wind Power Conversion Technology*, vol. 12, no. 5, pp. 431–444, 2009.

[50] F. Porté-Agel, Y.-T. Wu, and C.-H. Chen, "A numerical study of the effects of wind direction on turbine wakes and power losses in a large wind farm," *Energies*, vol. 6, no. 10, pp. 5297–5313, 2013.

[51] S. Xie and C. Archer, "Self-similarity and turbulence characteristics of wind turbine wakes via large-eddy simulation," *Wind Energy*, vol. 18, no. 10, pp. 1815–1838, 2015.

[52] J. Cleijne, J. Coelingh, and A. Van Wijk, *Description of the North Sea wind climate for offshore wind energy applications*. TNO Institute of Environmental and Energy Technology, 1991.

[53] R. J. Barthelmie, S. T. Frandsen, M. Nielsen, S. Pryor, P.-E. Rethore, and H. E. Jørgensen, "Modelling and measurements of power losses and turbulence intensity in wind turbine wakes at Middelgrunden offshore wind farm," *Wind Energy: An International Journal for Progress and Applications in Wind Power Conversion Technology*, vol. 10, no. 6, pp. 517–528, 2007.

[54] FPS Health, Food Chain Safety and Environment, "Something is moving at sea - the marine spatial plan for 2020-2026," Belgian Federal Public Service (FPS), Tech. Rep., 2020.

[55] A. McCoy, W. Musial, R. Hammond, *et al.*, "Offshore wind market report: 2024 edition," National Renewable Energy Laboratory (NREL), Golden, CO (United States), Tech. Rep., 2024.

[56] M. Đukan, A. Gumber, F. Egli, and B. Steffen, "The role of policies in reducing the cost of capital for offshore wind," *Iscience*, vol. 26, no. 6, 2023.

[57] COWI, "Foreign experiences for awarding offshore wind: New concepts for awarding offshore wind licences - part 1," Danish Energy Agency, Tech. Rep., 2022.

[58] SPF Economie, PME, Classes moyennes et Energie, "Arrêté royal établissant la procédure de mise en concurrence, les conditions et la procédure d'octroi des concessions domaniales et les conditions générales pour l'utilisation des parcelles pour la construction et l'exploitation d'une installation pour la production d'électricité à partir de sources d'énergie renouvelables dans les espaces marins sous la juridiction de la Belgique," Service Public Fédéral Belge, Tech. Rep., 2024.

[59] N. Chestney, "Wind power production from very large offshore wind farms," *Reuters*, 2023.

[60] L. Hirth and S. Müller, "System-friendly wind power: How advanced wind turbine design can increase the economic value of electricity generated through wind power," *Energy Economics*, vol. 56, pp. 51–63, 2016.

[61] F. Rasmussen, F. Zahle, A. B. Abrahamsen, A. Natarajan, and H. A. Madsen, "Pushing the physics of the large turbines of the future," in *DTU International Energy Report 2021: Perspectives on Wind Energy*, DTU Wind Energy, 2021, pp. 76–87.

[62] H. A. Madsen, F. Zahle, F. Meng, T. Barlas, F. Rasmussen, and R. Rudolf, "Initial performance and load analysis of the lowwind turbine in comparison with a conventional turbine," in *Journal of Physics: Conference Series*, IOP Publishing, vol. 1618, 2020.

[63] D. Moulas, M. Shafiee, and A. Mehmanparast, "Damage analysis of ship collisions with offshore wind turbine foundations," *Ocean Engineering*, vol. 143, pp. 149–162, 2017.

[64] C. Jung and D. Schindler, "The properties of the global offshore wind turbine fleet," *Renewable and Sustainable Energy Reviews*, vol. 186, p. 113 667, 2023.

[65] "Offshore wind in europe: Key trends and statistics 2018," WindEurope, Tech. Rep., 2019.

[66] C. Ng and L. Ran, *Offshore Wind Farms: Technologies, Design and Operation*. Woodhead Publishing, 2016.

[67] J. J. Thomas, N. F. Baker, P. Malisani, *et al.*, "A comparison of eight optimization methods applied to a wind farm layout optimization problem," *Wind Energy Science*, vol. 8, no. 5, pp. 865–891, 2023.

[68] M. Sickler, B. Ummels, M. Zaaijer, R. Schmehl, and K. Dykes, "Offshore wind farm optimisation: A comparison of performance between regular and irregular wind turbine layouts," *Wind Energy Science*, vol. 8, no. 7, pp. 1225–1233, 2023.

[69] M. S. De Alencar, T. Göçmen, and N. Cutululis, "GNN-based surrogate modeling for collection systems costs," in *Journal of Physics: Conference Series*, IOP Publishing, vol. 2767, 2024.

[70] G. Quinonez-Varela, G. W. Ault, O. Anaya-Lara, and J. R. McDonald, "Electrical collector system options for large offshore wind farms," *IET Renewable power generation*, vol. 1, no. 2, pp. 107–114, 2007.

[71] J. Fu and S. Shah, "Offshore transmission - key to unlocking wind energy from oceans," *IEEE Power & Energy Magazine*, vol. 22, no. 5, pp. 17–19, 2024.

[72] D. Kurthakoti, "Offshore wind - design, development, construction, operation," *IEEE Power & Energy Magazine*, vol. 22, no. 5, pp. 120–124, 2024.

[73] "High voltage off the belgian coast," Elia, Tech. Rep., 2019.

[74] "Federal development plan of the belgian transmission system (2024-2034)," Elia, Tech. Rep., 2023.

[75] J. Chang, B. C. Ummels, W. G. van Sark, H. P. den Rooijen, and W. L. Kling, "Economic evaluation of offshore wind power in the liberalized Dutch power market," *Wind Energy*, vol. 12, no. 5, pp. 507–523, 2009.

[76] T. Soares, T. V. Jensen, N. Mazzi, P. Pinson, and H. Morais, "Optimal offering and allocation policies for wind power in energy and reserve markets," *Wind Energy*, vol. 20, no. 11, pp. 1851–1870, 2017.

[77] H. Dong, J. Xie, and X. Zhao, "Wind farm control technologies: From classical control to reinforcement learning," *Progress in Energy*, 2022.

[78] D. R. Houck, "Review of wake management techniques for wind turbines," *Wind Energy*, vol. 25, no. 2, pp. 195–220, 2022.

[79] R. He, H. Yang, and L. Lu, "Optimal yaw strategy and fatigue analysis of wind turbines under the combined effects of wake and yaw control," *Applied Energy*, vol. 337, 2023.

[80] S. Kanev and T. van Engelen, "Wind turbine extreme gust control," *Wind Energy: An International Journal for Progress and Applications in Wind Power Conversion Technology*, vol. 13, no. 1, pp. 18–35, 2010.

[81] E. Topham and D. McMillan, "Sustainable decommissioning of an offshore wind farm," *Renewable energy*, vol. 102, pp. 470–480, 2017.

[82] J. P. Pfeifenberger, A. Orths, W. Wang, and J. DeLosa, "Planning for the winds of change," *IEEE Power & Energy Magazine*, vol. 22, no. 5, pp. 20–30, 2024.

[83] A. C. Müller and S. Guido, *Introduction to Machine Learning with Python: A Guide for Data Scientists*. O'Reilly Media, Inc., 2016.

[84] F. Pelletier, C. Masson, and A. Tahan, "Wind turbine power curve modelling using artificial neural network," *Renewable Energy*, vol. 89, pp. 207–214, 2016.

[85] M. Schlechtingen, I. F. Santos, and S. Achiche, "Using data-mining approaches for wind turbine power curve monitoring: A comparative study," *IEEE Transactions on Sustainable Energy*, vol. 4, no. 3, pp. 671–679, 2013.

[86] H. Zhou, Y. Qiu, Y. Feng, and J. Liu, "Power prediction of wind turbine in the wake using hybrid physical process and machine learning models," *Renewable Energy*, vol. 198, pp. 568–586, 2022.

[87] T.-H. Nguyen, J.-F. Toubeau, E. D. Jaeger, and F. Vallee, "Fast and reliable modelling of offshore wind generation for adequacy studies," *IEEE Transactions on Industry Applications*, pp. 1–10, 2023.

[88] Z. Ti, X. W. Deng, and M. Zhang, "Artificial neural networks based wake model for power prediction of wind farm," *Renewable Energy*, vol. 172, pp. 618–631, 2021.

[89] N. Zehtabiyan-Rezaie, A. Iosifidis, and M. Abkar, "Physics-guided machine learning for wind-farm power prediction: Toward interpretability and generalizability," *PRX Energy*, vol. 2, no. 1, 2023.

[90] J. Park and J. Park, "Physics-induced graph neural network: An application to wind-farm power estimation," *Energy*, vol. 187, 2019.

[91] Y.-T. Wu, T.-L. Liao, C.-K. Chen, C.-Y. Lin, and P.-W. Chen, "Power output efficiency in large wind farms with different hub heights and configurations," *Renewable Energy*, vol. 132, pp. 941–949, 2019.

[92] S.-P. Breton, J. Sumner, J. N. Sørensen, K. S. Hansen, S. Sarmast, and S. Ivanell, "A survey of modelling methods for high-fidelity wind farm simulations using large eddy simulation," *Philosophical Transactions of the Royal Society A: Mathematical, Physical and Engineering Sciences*, vol. 375, no. 2091, 2017.

[93] M. Moens, "Large eddy simulation of wind farm flows : Improved actuator disk model and investigations of wake phenomena," Ph.D. dissertation, UCL - Ecole Polytechnique de Louvain, 2018.

[94] M. Churchfield, S. Lee, P. Moriarty, *et al.*, "A large-eddy simulation of wind-plant aerodynamics," in *50th AIAA aerospace sciences meeting including the new horizons forum and aerospace exposition*, 2012, p. 537.

[95] B. Chaouat, "The state of the art of hybrid RANS/LES modeling for the simulation of turbulent flows," *Flow, turbulence and combustion*, vol. 99, pp. 279–327, 2017.

[96] F. G. Schmitt, "About boussinesq's turbulent viscosity hypothesis: Historical remarks and a direct evaluation of its validity," *Comptes Rendus Mécanique*, vol. 335, no. 9-10, pp. 617–627, 2007.

[97] P. Spalart and S. Allmaras, "A one-equation turbulence model for aerodynamic flows," in *30th Aerospace Sciences Meeting and Exhibit*, 1992, p. 439.

[98] D. C. Wilcox, "Reassessment of the scale-determining equation for advanced turbulence models," *AIAA journal*, vol. 26, no. 11, pp. 1299–1310, 1988.

[99] W. P. Jones and B. E. Launder, "The prediction of laminarization with a two-equation model of turbulence," *International journal of heat and mass transfer*, vol. 15, no. 2, pp. 301–314, 1972.

[100] F. R. Menter, "Two-equation eddy-viscosity turbulence models for engineering applications," *AIAA journal*, vol. 32, no. 8, pp. 1598–1605, 1994.

[101] J. Hart, "Comparison of turbulence modeling approaches to the simulation of a dimpled sphere," *Procedia engineering*, vol. 147, pp. 68–73, 2016.

[102] N. Troldborg, F. Zahle, N. N. Sørensen, and P.-E. Réthoré, "Comparison of wind turbine wake properties in non-uniform inflow predicted by different rotor models," in *Journal of Physics: Conference Series*, IOP Publishing, vol. 555, 2014.

[103] M. P. van der Laan, N. N. Sørensen, P.-E. Réthoré, *et al.*, "The k-ϵ-fp model applied to wind farms," *Wind Energy*, vol. 18, no. 12, pp. 2065–2084, 2015.

[104] *RAVE: Research at Ahlpa Ventus*, last access: August 2024. [Online]. Available: `https://rave-offshore.de/en/data.html`.

[105] N. Stergiannis, C. Lacor, J. Beeck, and R. Donnelly, "CFD modelling approaches against single wind turbine wake measurements using RANS," in *Journal of Physics: Conference Series*, IOP Publishing, vol. 753, 2016.

[106] M. E. Hoem, "Wind Turbine Simulations with OpenFOAM," M.S. thesis, Norwegian University of Science and Technology, 2018.

[107] P. Richards and R. Hoxey, "Appropriate boundary conditions for computational wind engineering models using the k-epsilon turbulence model," *Journal of wind engineering and industrial aerodynamics*, vol. 46, pp. 145–153, 1993.

[108] L. Caretto, A. Gosman, S. Patankar, and D. Spalding, "Two calculation procedures for steady, three-dimensional flows with recirculation," in *Proceedings of the Third International Conference on Numerical Methods in Fluid Mechanics: Vol. II Problems of Fluid Mechanics*, Springer, 1973, pp. 60–68.

[109] *ESI OpenCFD Release OpenFOAM v2106*, last access: August 2024. [Online]. Available: `https://www.openfoam.com/news/main-news/openfoam-v2106`.

[110] N. Sedaghatizadeh, M. Arjomandi, R. Kelso, B. Cazzolato, and M. H. Ghayesh, "Modelling of wind turbine wake using large eddy simulation," *Renewable Energy*, vol. 115, pp. 1166–1176, 2018.

[111] N. O. Jensen, *A note on wind generator interaction*. Citeseer, 1983, vol. 2411.

[112] S. Frandsen, R. Barthelmie, S. Pryor, *et al.*, "Analytical modelling of wind speed deficit in large offshore wind farms," *Wind Energy: An International Journal for Progress and Applications in Wind Power Conversion Technology*, vol. 9, no. 1-2, pp. 39–53, 2006.

[113] M. Bastankhah and F. Porté-Agel, "A new analytical model for wind-turbine wakes," *Renewable energy*, vol. 70, pp. 116–123, 2014.

[114] M. Bastankhah and F. Porté-Agel, "Experimental and theoretical study of wind turbine wakes in yawed conditions," *Journal of Fluid Mechanics*, vol. 806, pp. 506–541, 2016.

[115] A. Niayifar and F. Porté-Agel, "Analytical modeling of wind farms: A new approach for power prediction," *Energies*, vol. 9, no. 9, p. 741, 2016.

[116] C. J. Bay, P. Fleming, B. Doekemeijer, J. King, M. Churchfield, and R. Mudafort, "Addressing deep array effects and impacts to wake steering with the cumulative-curl wake model," *Wind Energy Science*, vol. 8, no. 3, pp. 401–419, 2023.

[117] M. Bastankhah, B. L. Welch, L. A. Martínez-Tossas, J. King, and P. Fleming, "Analytical solution for the cumulative wake of wind turbines in wind farms," *Journal of Fluid Mechanics*, vol. 911, A53, 2021.

[118] F. Blondel and M. Cathelain, "An alternative form of the super-gaussian wind turbine wake model," *Wind Energy Science*, vol. 5, no. 3, pp. 1225–1236, 2020.

[119] G. Nai-Zhi, Z. Ming-Ming, and L. Bo, "A data-driven analytical model for wind turbine wakes using machine learning method," *Energy Conversion and Management*, vol. 252, p. 115 130, 2022.

[120] L. P. Chamorro and F. Porté-Agel, "A wind-tunnel investigation of wind-turbine wakes: Boundary-layer turbulence effects," *Boundary-layer meteorology*, vol. 132, pp. 129–149, 2009.

[121] W. Zhang, C. D. Markfort, and F. Porté-Agel, "Wind-turbine wakes in a convective boundary layer: A wind-tunnel study," *Boundary-layer meteorology*, vol. 146, pp. 161–179, 2013.

[122] Y.-T. Wu and F. Porté-Agel, "Atmospheric turbulence effects on wind-turbine wakes: An LES study," *energies*, vol. 5, no. 12, pp. 5340–5362, 2012.

[123] M. Gaumond, P.-E. Réthoré, S. Ott, A. Pena, A. Bechmann, and K. S. Hansen, "Evaluation of the wind direction uncertainty and its impact on wake modeling at the horns rev offshore wind farm," *Wind Energy*, vol. 17, no. 8, pp. 1169–1178, 2014.

[124] B. M. Doekemeijer, E. Simley, and P. Fleming, "Comparison of the gaussian wind farm model with historical data of three offshore wind farms," *Energies*, vol. 15, no. 6, p. 1964, 2022.

[125] A. Crespo, J. Herna, *et al.*, "Turbulence characteristics in wind-turbine wakes," *Journal of Wind Engineering and Industrial Aerodynamics*, vol. 61, no. 1, pp. 71–85, 1996.

[126] P. B. Lissaman, "Energy effectiveness of arbitrary arrays of wind turbines," *Journal of energy*, vol. 3, no. 6, pp. 323–328, 1979.

[127] I. Katic, J. Højstrup, and N. O. Jensen, "A simple model for cluster efficiency," in *European Wind Energy Association Conference and Exhibition*, A. Raguzzi, 1987, pp. 407–410.

[128] K. Gunn, C. Stock-Williams, M. Burke, *et al.*, "Limitations to the validity of single wake superposition in wind farm yield assessment," in *Journal of Physics: Conference Series*, IOP Publishing, vol. 749, 2016.

[129] NREL, *FLORIS. Version 4.4.1*, last access: November 2024. [Online]. Available: `https://github.com/NREL/floris`.

[130] N. Hamilton, C. J. Bay, P. Fleming, J. King, and L. A. Martínez-Tossas, "Comparison of modular analytical wake models to the lillgrund wind plant," *Journal of Renewable and Sustainable Energy*, vol. 12, no. 5, 2020.

[131] B. M. Doekemeijer, D. van der Hoek, and J.-W. van Wingerden, "Closed-loop model-based wind farm control using FLORIS under time-varying inflow conditions," *Renewable Energy*, vol. 156, pp. 719–730, 2020.

[132] *Offshore wind farms in belgium*, last access: November 2024. [Online]. Available: `https://odnature.naturalsciences.be/mumm/en/windfarms/`.

[133] H. Hersbach *et al.*, *ERA5 hourly data on single levels from 1959 to present*, Copernicus Climate Change Service (C3S) Climate Data Store (CDS), last access: June, 2024, 2018. [Online]. Available: `10.24381/cds.adbb2d47`.

[134] J.-F. Toubeau, T. Morstyn, J. Bottieau, *et al.*, "Capturing spatio-temporal dependencies in the probabilistic forecasting of distribution locational marginal prices," *IEEE Transactions on Smart Grid*, vol. 12, no. 3, pp. 2663–2674, 2020.

[135] N. S. Ghaisas and C. L. Archer, "Geometry-based models for studying the effects of wind farm layout," *Journal of Atmospheric and Oceanic Technology*, vol. 33, no. 3, pp. 481–501, 2016.

[136] G. E. Karniadakis, I. G. Kevrekidis, L. Lu, P. Perdikaris, S. Wang, and L. Yang, "Physics-informed machine learning," *Nature Reviews Physics*, vol. 3, no. 6, pp. 422–440, 2021.

[137] B. Huang and J. Wang, "Applications of physics-informed neural networks in power systems: A review," *IEEE Transactions on Power Systems*, vol. 38, no. 1, pp. 572–588, 2022.

[138] D. Vahidi and F. Porté-Agel, "A physics-based model for wind turbine wake expansion in the atmospheric boundary layer," *Journal of Fluid Mechanics*, vol. 943, A49, 2022.

[139] J.-F. Toubeau, "Stochastic optimization of virtual power plants participating in electricity markets: From forecasting to decision-making," Ph.D. dissertation, Faculté Polytechnique de Mons (University of Mons), 2018.

[140] L. Breiman, J. Friedman, C. J. Stone, and R. Olshen, *Classification and Regression Trees*. CRC Press, 1984.

[141] L. Breiman, "Random forests," *Machine learning*, vol. 45, pp. 5–32, 2001.

[142] J. H. Friedman, "Stochastic gradient boosting," *Computational statistics & data analysis*, vol. 38, no. 4, pp. 367–378, 2002.

[143] W. S. McCulloch and W. Pitts, "A logical calculus of the ideas immanent in nervous activity," *The bulletin of mathematical biophysics*, vol. 5, pp. 115–133, 1943.

[144] D. Bertoin, J. Bolte, S. Gerchinovitz, and E. Pauwels, "Numerical influence of ReLU'(0) on backpropagation," *Advances in Neural Information Processing Systems*, vol. 34, pp. 468–479, 2021.

[145] N. Zehtabiyan-Rezaie, A. Iosifidis, and M. Abkar, "Data-driven fluid mechanics of wind farms: A review," *Journal of Renewable and Sustainable Energy*, vol. 14, no. 3, 2022.

[146] S. Sulaeman, M. Benidris, J. Mitra, and C. Singh, "A wind farm reliability model considering both wind variability and turbine forced outages," *IEEE Transactions on Sustainable Energy*, vol. 8, no. 2, pp. 629–637, 2017.

[147] D. Villanueva, A. Feijóo, and J. L. Pazos, "Simulation of correlated wind speed data for economic dispatch evaluation," *IEEE Transactions on Sustainable Energy*, vol. 3, no. 1, pp. 142–149, 2011.

[148] R. Billinton, Y. Gao, and R. Karki, "Composite system adequacy assessment incorporating large-scale wind energy conversion systems considering wind speed correlation," *IEEE Transactions on Power Systems*, vol. 24, no. 3, pp. 1375–1382, 2009.

[149] J. Zhu and Y. Zhang, "A frequency and duration method for adequacy assessment of generation systems with wind farms," *IEEE Transactions on Power Systems*, vol. 34, no. 2, pp. 1151–1160, 2018.

[150] A. Almutairi, M. H. Ahmed, and M. Salama, "Use of MCMC to incorporate a wind power model for the evaluation of generating capacity adequacy," *Electric Power Systems Research*, vol. 133, pp. 63–70, 2016.

[151] H. Yang, K. Xie, H.-M. Tai, and Y. Chai, "Wind farm layout optimization and its application to power system reliability analysis," *IEEE Transactions on Power Systems*, vol. 31, no. 3, pp. 2135–2143, 2016.

[152] H. Kim, C. Singh, and A. Sprintson, "Simulation and estimation of reliability in a wind farm considering the wake effect," *IEEE Transactions on Sustainable Energy*, vol. 3, no. 2, pp. 274–282, 2012.

[153] R. Billinton and L. Wenyuan, *Reliability Assessment of Electric Power Systems Using Monte Carlo Methods*. New York: Plenum Press, 1994.

[154] R. Billinton, R. Karki, Y. Gao, D. Huang, P. Hu, and W. Wangdee, "Adequacy assessment considerations in wind integrated power systems," *IEEE Transactions on Power Systems*, vol. 27, no. 4, pp. 2297–2305, 2012.

[155] F. Vallee, J. Lobry, and O. Deblecker, "System reliability assessment method for wind power integration," *IEEE Transactions on Power Systems*, vol. 23, no. 3, pp. 1288–1297, 2008.

[156] B. W. Tuinema, J. R. Torres, A. I. Stefanov, F. M. Gonzalez-Longatt, and M. van der Meijden, *Probabilistic Reliability Analysis of Power Systems*. Springer, 2020.

[157] V. Miranda, L. de Magalhaes Carvalho, M. A. Da Rosa, A. M. L. Da Silva, and C. Singh, "Improving power system reliability calculation efficiency with EPSO variants," *IEEE Transactions on Power Systems*, vol. 24, no. 4, pp. 1772–1779, 2009.

[158] M. Alavi-Sereshki and C. Singh, "A generalized continuous distribution approach for generating capacity reliability evaluation and its applications," *IEEE Transactions on Power Systems*, vol. 6, no. 1, pp. 16–22, 1991.

[159] A. A. Kadhem, N. I. A. Wahab, I. Aris, J. Jasni, and A. N. Abdalla, "Computational techniques for assessing the reliability and sustainability of electrical power systems: A review," *Renewable and Sustainable Energy Reviews*, vol. 80, pp. 1175–1186, 2017.

[160] L. Söder, E. Tómasson, A. Estanqueiro, *et al.*, "Review of wind generation within adequacy calculations and capacity markets for different power systems," *Renewable and Sustainable Energy Reviews*, vol. 119, 2020.

[161] R. Billinton, S. Kumar, N. Chowdhury, *et al.*, "A reliability test system for educational purposes-basic data," *IEEE Transactions on Power Systems*, vol. 4, no. 3, pp. 1238–1244, 1989.

[162] C. Grigg, P. Wong, P. Albrecht, *et al.*, "The IEEE reliability test system-1996. A report prepared by the reliability test system task force of the application of probability methods subcommittee," *IEEE Transactions on power systems*, vol. 14, no. 3, pp. 1010–1020, 1999.

[163] A. Hernandez, "Impact of hydrogen on power system adequacy assessment studies - application on the future coupled electrcicty-hydrogen belgian system in 2030," Ph.D. dissertation, University of Louvain (UCL), 2024.

[164] E. Erdem and J. Shi, "ARMA based approaches for forecasting the tuple of wind speed and direction," *Applied Energy*, vol. 88, no. 4, pp. 1405–1414, 2011.

[165] R. Billinton, H. Chen, and R. Ghajar, "Time-series models for reliability evaluation of power systems including wind energy," *Microelectronics Reliability*, vol. 36, no. 9, pp. 1253–1261, 1996.

[166] F. Anderson, R. Dawid, D. G. Cava, and D. McMillan, "Operational metrics for an offshore wind farm & their relation to turbine access restrictions and position in the array," in *Journal of Physics: Conference Series*, IOP Publishing, vol. 2018, 2021.

[167] S. Pfenninger and I. Staffell, "Long-term patterns of european PV output using 30 years of validated hourly reanalysis and satellite data," *Energy*, vol. 114, pp. 1251–1265, 2016.

[168] I. Staffell and S. Pfenninger, "Using bias-corrected reanalysis to simulate current and future wind power output," *Energy*, vol. 114, pp. 1224–1239, 2016.

[169] *Renewables.ninja*, last access: November 2024. [Online]. Available: `https://www.renewables.ninja/`.

[170] 3E, "LCOE offshore wind in the Princess zone: Analysis of various density scenarios," FOD Economie, Tech. Rep., 2021.

[171] W. Munters, B. Adiloglu, S. Buckingham, and J. van Beeck, "Wake impact of constructing a new offshore wind farm zone on an existing downwind cluster: A case study of the belgian princess elisabeth zone using floris," in *Journal of Physics: Conference Series*, IOP Publishing, vol. 2265, 2022.

[172] E. Perroy, D. Lucas, and V. Debusschere, "Provision of frequency containment reserve through large industrial end-users pooling," *IEEE Transactions on Smart Grid*, vol. 11, no. 1, pp. 26–36, 2020.

[173] P. Sumetha-Aksorn, K. Dykes, and O. C. Yilmaz, "Assessing the economical impact of innovations for offshore wind farms through a holistic modelling approach," in *Journal of Physics: Conference Series*, IOP Publishing, vol. 2265, 2022.

[174] Windvision, Enercon, Eneco, and Elia, "Delivery of downward aFRR by wind farms," Elia, Tech. Rep., 2015.

[175] J. Liang, S. Grijalva, and R. G. Harley, "Increased wind revenue and system security by trading wind power in energy and regulation reserve markets," *IEEE Transactions on Sustainable Energy*, vol. 2, no. 3, pp. 340–347, 2011.

[176] M. Cañas-Carretón and M. Carrión, "Generation capacity expansion considering reserve provision by wind power units," *IEEE Transactions on Power Systems*, vol. 35, no. 6, pp. 4564–4573, 2020.

[177] J. Quick, P.-E. Rethore, M. Mølgaard Pedersen, R. V. Rodrigues, and M. Friis-Møller, "Stochastic gradient descent for wind farm optimization," *Wind Energy Science*, vol. 8, no. 8, pp. 1235–1250, 2023.

[178] R. V. Rodrigues, M. M. Pedersen, J. P. Schøler, J. Quick, and P. Réthoré, "Speeding up large wind farms layout optimization using gradients, parallelization, and a heuristic algorithm for the initial layout," *Wind Energy Science*, vol. 2023, pp. 1–30, 2023.

[179] J. Park and K. H. Law, "Layout optimization for maximizing wind farm power production using sequential convex programming," *Applied Energy*, vol. 151, pp. 320–334, 2015.

[180] P. Hou, W. Hu, M. Soltani, and Z. Chen, "Optimized placement of wind turbines in large-scale offshore wind farm using particle swarm optimization algorithm," *IEEE Transactions on Sustainable Energy*, vol. 6, no. 4, pp. 1272–1282, 2015.

[181] J. Feng and W. Z. Shen, "Solving the wind farm layout optimization problem using random search algorithm," *Renewable Energy*, vol. 78, pp. 182–192, 2015.

[182] H. Long, P. Li, and W. Gu, "A data-driven evolutionary algorithm for wind farm layout optimization," *Energy*, vol. 208, p. 118 310, 2020.

[183] A. P. Stanley, O. Roberts, J. King, and C. J. Bay, "Objective and algorithm considerations when optimizing the number and placement of turbines in a wind power plant," *Wind Energy Science*, vol. 2021, pp. 1–38, 2021.

[184] J. S. González, A. G. G. Rodriguez, J. C. Mora, J. R. Santos, and M. B. Payan, "Optimization of wind farm turbines layout using an evolutive algorithm," *Renewable Energy*, vol. 35, no. 8, pp. 1671–1681, 2010.

[185] J. S. Gonzalez, M. B. Payan, and J. M. Riquelme-Santos, "Optimization of wind farm turbine layout including decision making under risk," *IEEE Systems Journal*, vol. 6, no. 1, pp. 94–102, 2012.

[186] ENTSO-E, *ENTSO-E Transparency Platform*, last access: November 2024. [Online]. Available: `https://transparency.entsoe.eu/`.

[187] ECMWF, "Intercomparison of operational wave forecasting systems against in-situ observations: data from BoM, DMI, DWD, ECCC, ECMWF, JMA, LOPS, METEOAM, METFR, METNO, NCEP, PRTOS, SHNSM, UKMO," WMO Lead Centre for Wave Forecast Verification LC-WFV and European Centre for Medium-Range Weather Forecasts ECMWF, Tech. Rep., 2024.

[188] M. A. Chitsazan, M. S. Fadali, and A. M. Trzynadlowski, "Wind speed and wind direction forecasting using echo state network with nonlinear functions," *Renewable Energy*, vol. 131, pp. 879–889, 2019.

[189] J. Lago, G. Marcjasz, B. De Schutter, and R. Weron, "Forecasting day-ahead electricity prices: A review of state-of-the-art algorithms, best practices and an open-access benchmark," *Applied Energy*, vol. 293, p. 116 983, 2021.

[190] J.-F. Toubeau, C. Ponsart, C. Stevens, Z. De Grève, and F. Vallée, "Sizing of underwater gravity storage with solid weights participating in electricity markets," *International Transactions on Electrical Energy Systems*, vol. 30, no. 10, 2020.

[191] T. Brijs, K. De Vos, C. De Jonghe, and R. Belmans, "Statistical analysis of negative prices in european balancing markets," *Renewable Energy*, vol. 80, pp. 53–60, 2015.

[192] Elia, "Terms and Conditions for balancing service providers for automatic Frequency Restoration Reserve (aFRR)," Elia, Tech. Rep., 2022.

[193] P. Wang, H. Zareipour, and W. D. Rosehart, "Descriptive models for reserve and regulation prices in competitive electricity markets," *IEEE Transactions on Smart Grid*, vol. 5, no. 1, pp. 471–479, 2013.

[194] R. Riva, J. Y. Liew, M. Friis-Møller, *et al.*, "Welcome to TOPFARM," 2024. [Online]. Available: `https://topfarm.pages.windenergy.dtu.dk/TopFarm2/index.html`.

[195] L. Lanzilao and J. Meyers, *A reference database of wind-farm large-eddy simulations for parametrizing effects of blockage and gravity waves*, version V2, 2023. DOI: `10.48804/L45LTT`. [Online]. Available: `https://doi.org/10.48804/L45LTT`.

[196] S. J. Andersen and N. Troldborg, "Description of TotalControl Reference Wind Farm Simulations," Dec. 2020. DOI: `10.11583/DTU.13160606.v2`. [Online]. Available: `https://data.dtu.dk/articles/dataset/Description_of_TotalControl_Reference_Wind_Farm_Simulations/13160606`.

[197] M. Lejeune, P. Chatelain, and M. Moens, *OnWaRDS: reference LES data - small 8 turbines wind farm*, version V1, 2022. DOI: `10.14428/DVN/AUVUI6`. [Online]. Available: `https://doi.org/10.14428/DVN/AUVUI6`.

[198] A. Kirby, T. Nishino, and T. D. Dunstan, "Two-scale interaction of wake and blockage effects in large wind farms," *Journal of Fluid Mechanics*, vol. 953, A39, 2022.

[199] X. Meng and G. E. Karniadakis, "A composite neural network that learns from multi-fidelity data: Application to function approximation and inverse pde problems," *Journal of Computational Physics*, vol. 401, 2020.

[200] A. Kirby, F.-X. Briol, T. D. Dunstan, and T. Nishino, "Data-driven modelling of turbine wake interactions and flow resistance in large wind farms," *Wind Energy*, vol. 26, no. 9, pp. 968–984, 2023.

[201] P. M. Gebraad, P. A. Fleming, and J.-W. van Wingerden, "Wind turbine wake estimation and control using FLORIDyn, a control-oriented dynamic wind plant model," in *2015 American Control Conference (ACC)*, IEEE, 2015, pp. 1702–1708.

[202] M. Becker, B. Ritter, B. Doekemeijer, *et al.*, "The revised FLORIDyn model: Implementation of heterogeneous flow and the Gaussian wake," *Wind Energy Science Discussions*, vol. 2022, pp. 1–25, 2022.

[203] B. Foloppe, W. Munters, S. Buckingham, L. Vandevelde, and J. van Beeck, "Development of a dynamic wake model accounting for wake advection delays and mesoscale wind transients," in *Journal of Physics: Conference Series*, IOP Publishing, vol. 2265, 2022.

[204] M. Lejeune, M. Moens, and P. Chatelain, "Extension and validation of an operational dynamic wake model to yawed configurations," in *Journal of Physics: Conference Series*, IOP Publishing, vol. 2265, 2022.

[205] M. Lejeune, M. Moens, and P. Chatelain, "A meandering-capturing wake model coupled to rotor-based flow-sensing for operational wind farm flow prediction," *Frontiers in Energy Research*, vol. 10, 2022.

[206] W. Munters, B. Adiloglu, S. Buckingham, and J. van Beeck, "Wake impact of constructing a new offshore wind farm zone on an existing downwind cluster: A case study of the belgian princess elisabeth zone using floris," in *Journal of Physics: Conference Series*, IOP Publishing, vol. 2265, 2022.

[207] W. C. Skamarock, J. Klemp, J. Dudhia, *et al.*, "A description of the advanced research WRF model version 4," *National Center for Atmospheric Research*, 2019.

[208] J. Schmidt, L. Vollmer, M. Dörenkämper, and B. Stoevesandt, "Foxes: Farm optimization and extended yield evaluation software," *Journal of Open Source Software*, vol. 8, no. 86, p. 5464, 2023.

[209] K. Devesse, L. Lanzilao, D. Allaerts, S. Jamaer, and J. Meyers, *WAYVE: Wind-fArm gravitY-waVe and blockagE code V2*, KU Leuven RDR, 2023. [Online]. Available: `https://doi.org/10.48804/XMNVVY`.

[210] P. Sørensen, M. Koivisto, and J. P. Murcia, "Elia - MOG II System Integration – Public version," DTU Wind Energy, for Elia, Tech. Rep., 2020.

[211] P. A. Fleming, J. Aho, A. Buckspan, *et al.*, "Effects of power reserve control on wind turbine structural loading," *Wind Energy*, vol. 19, no. 3, pp. 453–469, 2016.

APPENDIX A.

List of Publications

Under Review

Peer-reviewed Journal papers

- **T-H. Nguyen**, J. Quick, P-E. Réthoré, J-F. Toubeau, E. De Jaeger and F. Vallée, "Offshore Wind Farm Layout Optimization Accounting for Participation to Secondary Reserve Markets", submitted to *Wind Energy Science*

- **T-H. Nguyen**, J-F. Toubeau, E. De Jaeger, and F. Vallée, "Topology-aware Surrogate for Future Offshore Wind Farms Using Machine Learning", submitted to *Applied Energy*

Published

Peer-reviewed Journal papers

- **T-H. Nguyen**, J-F. Toubeau, E. De Jaeger and F. Vallée, "Fast and Reliable Modeling of Offshore Wind Generation for Adequacy Studies," in IEEE Transactions on Industry Applications, vol. 59, no. 6, pp. 7116-7125, 2023, doi: 10.1109/TIA.2023.3307076.

- **T-H. Nguyen**, J-F. Toubeau, E. De Jaeger and F. Vallée, "Adequacy Assessment Using Data-driven Models to Account for Aerodynamic Losses in Offshore Wind Generation", in Electric Power Systems Research, vol. 211, 2022, doi: 10.1016/j.epsr.2022.108599

Peer-reviewed Conference papers

- **T-H. Nguyen**, G. Paternostre, J-F. Toubeau, E. De Jaeger, and F. Vallée, "Adequacy Computations for Power Systems with a High Share of Offshore Wind Generation: Application to Belgium", in 2023 EAWE PhD seminar, Hannover, Germany, 2023
- **T-H. Nguyen**, N. Thils, J-F. Toubeau, E. De Jaeger, and F. Vallée, "Offshore Wind Farm Power Prediction for Security of Supply Assessment Using a Unique Machine Learning Proxy", in 2022 EAWE PhD seminar, Bruges, Belgium, 2022
- **T-H. Nguyen**, J-F. Toubeau, E. De Jaeger and F. Vallée, "Adequacy Assessment Using Data-driven Models to Account for Aerodynamic Losses in Offshore Wind Generation", in 2022 IEEE Power Systems Computation Conference (PSCC), Porto, Portugal, 2022
- **T-H. Nguyen**, J-F. Toubeau, E. De Jaeger and F. Vallée, "Machine Learning Proxies Integrating Wake Effects in Offshore Wind Generation for Adequacy Studies," in 2021 IEEE International Conference on Environment and Electrical Engineering and 2021 IEEE Industrial and Commercial Power Systems Europe (EEEIC / I&CPS Europe), Bari, Italy, 2021, doi: 10.1109/EEEIC/ICPSEurope51590.2021.9584611.